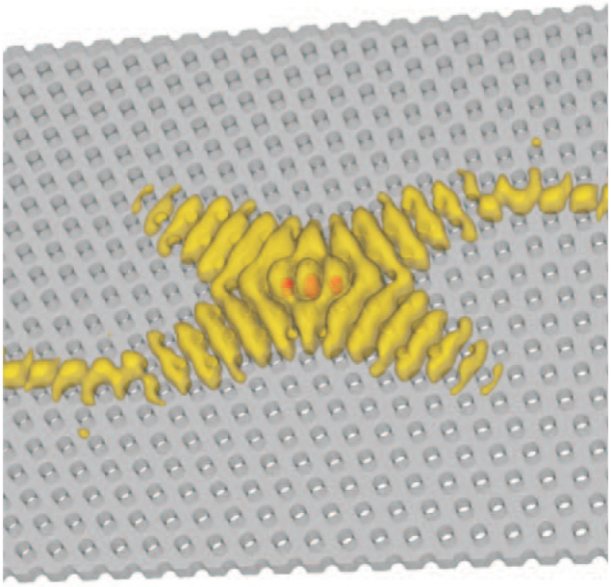

All-Optical Switching in Photonic Crystal Cavities

Mikkel Heuck

PhD Thesis

March 2013

DTU Fotonik
Department of Photonics Engineering

All-Optical Switching in Photonic Crystal Cavities

A dissertation
submitted to the Department of Photonics Engineering
at the Technical University of Denmark
in partial fulfillment of the requirements
for the degree of
philosophiæ doctor

Mikkel Heuck
March 31st, 2013

Preface

This thesis is submitted in candidacy for the PhD degree from the Technical University of Denmark. The project has been carried out in the Theory and Signal Processing group at DTU Fotonik - Department of Photonics Engineering from 2010 to 2013, under the supervision of Philip Trøst Kristensen and Professor Jesper Mørk. In the fall of 2011, I visited Thales Research and Technology in Palaiseau, France. The main purpose of the visit was to gain experience with experimental techniques to study the structures under consideration in this thesis.

Acknowledgements

First and foremost, I would like to thank my supervisors, Philip Trøst Kristensen and Jesper Mørk. Philip for our countless discussions that always deepened my physical and mathematical understanding and pushed the project forward. Jesper for sharing his enormous physical insight and enabling me to always leave a supervisor meeting in an optimistic and enthusiastic spirit. I would also like to extend a special thanks to Alfredo de Rossi and Sylvain Combrié for welcoming and guiding me in their lab at Thales. Also, for the continuing fruitful discussions with Alfredo about experimental techniques and modeling. A special thanks is also owed to Yuriy Elesin from DTU Mechanical Engineering, for letting me use his FDTD code. From DTU - Mathematics, I would like to thank Mads Peter Sørensen and Anton Evgrafov, for guidance related to optimal control theory and Kristian Kristiansen for help with mathematical issues in general. I would like to thank Christophe Peucheret and Jing Xu from DTU Fotonik for fruitful discussions related to optical communication systems. A thanks is also extended to the entire Theory and Signal Processing group, especially Yi Yu for discussions about design and fabrication of devices.

Finally, I would like to thank all the people, who have made my time at DTU Fotonik very enjoyable, in particular Christian Agger, Lars Rishøj, Martin Pedersen, Henrik Steffensen, and Johan Raunkjær Ott.

Mikkel Heuck
Kongens Lyngby, 31. Marts, 2013.

Abstract

All-Optical switching in photonic crystal waveguide-cavity structures is studied predominantly theoretically and numerically, but also from an experimental point of view.

We have calculated the first order perturbations to the resonance frequency and decay rate of cavity modes, using a mathematical framework that correctly takes into account the leaky nature of these modes. This represents the foundation for including nonlinearities into the temporal coupled mode theory, which is widely used to model the cavity-waveguide dynamics.

In the experimental part of the thesis, we have considered both homodyne and heterodyne measurements of the cavity dynamics, as well as a comparison with the model developed from the perturbation theory mentioned above. The model was seen to provide a qualitative agreement with the experiments indicating that the relevant physical mechanisms are accounted for by the model.

A considerable effort has been put into designing advanced structures with increased flexibility and the ability to avoid some of the difficulties in terms of experimental investigations mentioned above. This has resulted in e.g. the four port device, where the signal and pump are spatially separated. This device was fabricated and characterized by colleagues within the group, and it was shown to perform very well in terms of cross-talk between the signal and pump.

Theoretical investigations as well as practical design proposals have resulted from a study of waveguide-cavity structures exhibiting Fano resonances. These devices were predicted to be superior to structures with the more well-known Lorentzian line shape in terms of energy consumption and switching contrast.

Finally, the mathematical framework of optimal control theory was employed as a general setting, in which the optical properties of the input fields may be tailored to optimize various objectives, such as the cavity energy. A particular example showed how to adjust the amplitude and phase of the pump field to maximize the cavity energy in a given time interval. The results also revealed how to extract the cavity energy faster than the photon lifetime by utilizing interference effects.

Mikkel Heuck
March 31st 2013

Resumé

Optisk switching i strukturer af koblede bølgeledere og kaviteter fremstillet i membraner af fotoniske krystaller er blevet undersøgt primært teoretisk og numerisk, men også ud fra et eksperimentelt synspunkt.

Vi har beregnet første-ordens perturbationer til resonansfrekvensen og koblingsraten af kavitetsmodes ved hjælp af en matematisk teori, som på korrekt vis tager højde for energitabet fra disse modes. Dette repræsenterer den underlæggende måde, hvorpå ikke-lineariteter introduceres i "temporal coupled mode theory", som i vid udstrækning bruges til at modellere dynamikken i strukturer af koblede bølgeledere og kaviteter.

I den eksperimentelle del af afhandlingen betragter vi både homodyne og heterodyne målemetoder til at studere kavitetsdynamikken. Derudover foretager vi en sammenligning af eksperimentelle resultater med numeriske beregninger baseret på den ovennævnte perturbationsanalyse. Vi ser en kvalitativ overensstemmelse mellem måleresultater og simuleringer, hvilket indikerer, at modellen indeholder de relevante fysiske mekanismer.

Der er blevet lagt en betragtelig indsats i at designe avancerede strukturer med forøget fleksibilitet samt mulighed for at undgå nogle af de eksperimentelle begrænsninger, som vi fandt ved brug af to-port-strukturer. Blandt disse designs er fire-port-strukturen, hvor pumpefeltet og signalet kan adskilles rumligt. Denne struktur er blevet fabrikeret og karakteriseret af en kollega fra gruppen, og resultatet viste en meget lille krydskobling mellem signalet og pumpen.

Et studie af strukturer, der udviser såkaldte Fano-resonanser, har resulteret i konkrete designforslag samt teoretiske overvejelser af deres egenskaber. Det er vist, at Fano-resonanser er overlegne med hensyn til energiforbrug i forhold til mere velkendte strukturer med Lorentz-resonancer.

Til sidst har vi benyttet den matematiske disciplin "optimal control theory" som en general ramme, hvori de optiske egenskaber af input-felterne kan optimeres med henblik på forskellige målsætninger. Som et eksempel har vi beregnet den optimale tidsafhængighed af både amplitude og fase af pumpefeltet, således at kavitetsenergien kan ændres mellem to fastsatte værdier i et fastsat tidsrum med mindst mulig indkoblet energi. Denne analyse viste også, at energien i kaviteten kan blive trukket ud hutigere end foton-levetiden ved hjælp af interferenseffekter.

List of Publications

The work carried out during this PhD project has resulted in the following publications:

Scientific Journals

- M. Heuck, P. T. Kristensen, and J. Mørk, "*Energy-Bandwidth Trade-off in All-Optical Photonic Crystal Microcavity Switches*", Optics Express, **19**, pp. 18410-18422, 2011.
- Y. Yu, M. Heuck, S. Ek, N. Kuznetsova, K. Yvind, and J. Mørk, "*Experimental Demonstration of a Four-Port Photonic Crystal Cross-Waveguide Structure*", Applied Physics Letters, **101**, 25, (2012).
- P. T. Kristensen, M. Heuck, and J. Mørk, "*Optimal Switching using Coherent Control*", Applied Physics Letters, **102**, 4, (2013).

Conference Proceedings

- M. Heuck, P. T. Kristensen, and J. Mørk, "*Patterning Effects in Ultrafast All-Optical Photonic Crystal Nanocavity Switches*", European Conference on Lasers and Electro-Optics and the European Quantum Electronics Conference, Munich, 2011.
- P. T. Kristensen, M. Heuck, and J. Mørk, "*Coherent all-optical switching in a bistable waveguide-cavity-waveguide system*", European Conference on Lasers and Electro-Optics and the European Quantum Electronics Conference, Munich, 2011.
- M. Heuck, P. T. Kristensen, and J. Mørk, "*A Non-Hermitian Approach to Non-Linear Switching Dynamics in Coupled Cavity-Waveguide Systems*", Conference on Lasers and Electro-Optics, San Jose, USA, 2012.
- S. Combrié, M. Heuck, S. Xavier, G. Lehoucq, S. Malaguti, G. Ballanca, S. Trillo, P. T. Kristensen, J. Mørk, and A. de Rossi,"*Demonstration of Optically Controlled re-Routing in a Photonic Crystal Three-Port Switch*",

Integrated Photonics Research, Silicon and Nanophotonics (IPR), Colorado Springs, USA, 2012.

- Y. Yu, S. Ek, M. Heuck, K. Yvind, and J. Mørk,"*InGaAsP Photonic Crystal Nanocavities with a Fano Line Shape Resonant at 1.55 μm*", Integrated Photonics Research, Silicon and Nanophotonics (IPR), Colorado Springs, USA, 2012.

Submitted Papers

- M. Heuck, P. T. Kristensen, Y. Elesin, and J. Mørk, "*Improved Switching using Fano Resonances in Photonic Crystal Structures*".

Papers in Preparation

- M. Heuck, S. Combrié, G. Lehoucq, S. Malaguti, G. Bellanca, S. Trillo, P. T. Kristensen, J. Mørk, P. Reithmaier, and A. de Rossi, "*Switching and Carrier Dynamics in an InP Photonic Crystal Nanocavity*".

Contents

1

Introduction

1.1 Motivation

The demand for bandwidth capacity in modern communication networks is exponentially increasing at a fast rate [1, 2]. This is primarily due to the amount of video content being shared over the Internet [2, 3]. Along with the increased Internet traffic comes an increase in energy consumption that will eventually limit this traffic, unless more energy-efficient technologies are developed. A source of increasing importance in the energy consumption of communication networks and high performance computing systems is dissipation in the electrical wiring. Resistive loss in metal wires increase with oscillation frequency, and this puts limitations on the achievable bandwidth [1]. Optical interconnects, where the information is carried by an optical signal, are thus becoming an interesting alternative at shorter and shorter distances, even down to the chip level. Achieving this, however, requires the development of extremely energy efficient and fast components, such as lasers, modulators, switches, and detectors. Whether optical logic will be part of this technology is an ongoing debate [4–7], which motivates research within this field to assist in finding the right answer. There are many considerations to take into account such as material system, scalability, and mass production cost. However, from a physicist's standpoint, understanding the ultimate limitations dictated by the underlying physics of these devices has the highest priority. In this thesis, we will explore the physics and performance of all-optical gates made from III-IV (InP) semiconductor photonic crystal (PC) membrane structures. Before moving on to the more technical details, the rest of this chapter is devoted to an introduction of the constituents of these gates and a discussion of possible applications.

1.2 Applications

In order to understand the functionality of a switch and the performance requirements we must impose, it is important to consider the context in which it is intended. There are many schemes to encode information onto an optical carrier utilizing its amplitude, phase, or carrier frequency [8]. The corresponding modulation formats are denoted amplitude modulation, phase shift keying, and frequency modulation, respectively. The information is encoded in bits representing some detectable change in the signal by either of the mentioned modulation formats. Generally, the time axis is divided into intervals, which contain a piece of information. The number of bits contained in each interval depends on the complexity of the modulation format. Here, we shall only consider binary symbols, where the amplitude, phase, or frequency may have two different values.

The information capacity of optical carriers may be increased by using multiplexing schemes such as wavelength division multiplexing (WDM). Because electromagnetic waves do not interact (when propagating in linear media), one may transmit several signals using either modulation format on the same transmission line, if the center frequencies of the signals are different. By spectral filtering of the combined signal at the detector, all the information may be extracted. This is the basic principle of WDM.

Considering all the usable modulation formats, it does not seem plausible that we can create a switching device, which will work on all of them. Therefore, as a starting point, it seems natural to focus on a switch intended for the simplest type of modulation. In this thesis, we will only consider switches

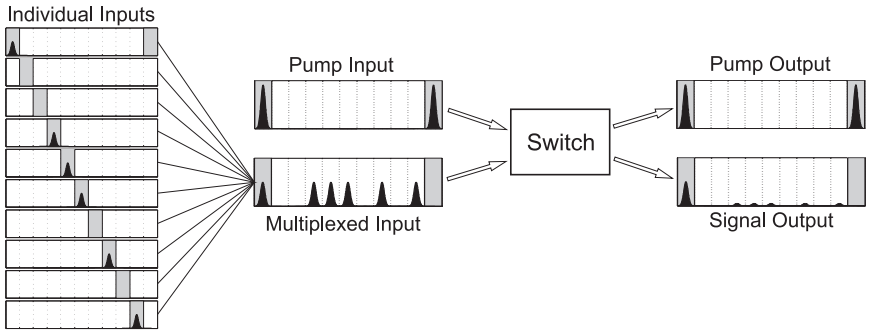

Figure 1.1: Schematic illustration of an OTDM system. Ten individual signals are interleaved into a single signal at a ten times higher information density. An optical switch is used to de-multiplex the dense signal to enable detection with electronic devices of limited frequency response.

intended for amplitude modulated signals. A multiplexing scheme, which operates with amplitude modulated signals is OTDM. The binary information

is represented by the presence or absence of an optical pulse. In OTDM the time intervals mentioned above are subdivided, which is possible if the widths of the pulses are much smaller than the original time interval. The overall information density (also denoted signal bandwidth) is increased by interleaving several individual signals into one interval. Fig. 1.1 illustrates the procedure, where ten individual signals are delayed with respect to each other and combined into a single signal with a ten times larger bandwidth. If the speed of the photo detector is too low to detect the pulses in individual time slots, a de-multiplexing scheme must be devised to read the information in each pulse. This is facilitated by using an all-optical switch as illustrated in Fig. 1.1. The switch works as a logical AND gate [9], where a signal output only appears if both a signal and a pump pulse are present at the input of a given time slot. The pump is a periodic signal with the same repetition rate as the original individual inputs and the pump pulse selects the time slot to be read out from the signal. On the output side, only the information in the targeted time slot is available because the switch is in its "off" state, when no pump pulse arrives simultaneously with the signal. The output signal may then be detected by a photo detector with an operation speed corresponding to the bandwidth of the individual inputs and the de-multiplexing is accomplished. A more detailed investigation of using an optical switch for de-multiplexing an OTDM signal will be considered in Chapter 7.

1.3 Photonic Crystals

Since the pioneering work by Yablonovitch [10] and John [11] in the late 1980's, PCs has been a very active field of research. To understand the physics of these structures, an analogy with electrons in periodic lattices is often employed. The potential arising from the atom cores sitting in a periodic lattice in crystals gives rise to interesting energy-dispersion properties of the electrons, like band gaps in semiconductor materials [12]. The meaning of a band gap is a range of energies, where electrons cannot propagate through the material. The typical wavelength of light is much larger than that of electrons, and thus, electromagnetic waves in a semiconductor crystal only experience an averaged potential. By actively structuring a material in a periodic manner with a lattice constant a on the order of the wavelength of the waves, a similar effect may be observed for light. The periodicity can be in one (Bragg stack), two (micro pillars), or three (inverse opals) dimensions [13]. Like the band gaps seen in unstructured semiconductors, the PC structures may exhibit photonic band gaps, where no light can propagate in certain frequency intervals. This allows one to confine light to well defined regions of space and by introducing point or line defects, cavities and waveguides may be formed. Because of their compatibility with planar processing, PC membranes [14] are a widely used platform for utilizing these special characteristics. In order to achieve light confinement in the perpendicular direction (denoted the z-direction), the membrane must be sur-

rounded by a material with a lower refractive index. Throughout this thesis, we consider membranes fabricated in InP that are under-etched so they are completely surrounded by air. The periodic lattice is created by etching holes into the membrane. Fig. 1.2(a) shows a top view of a membrane with a triangular lattice of air-holes.

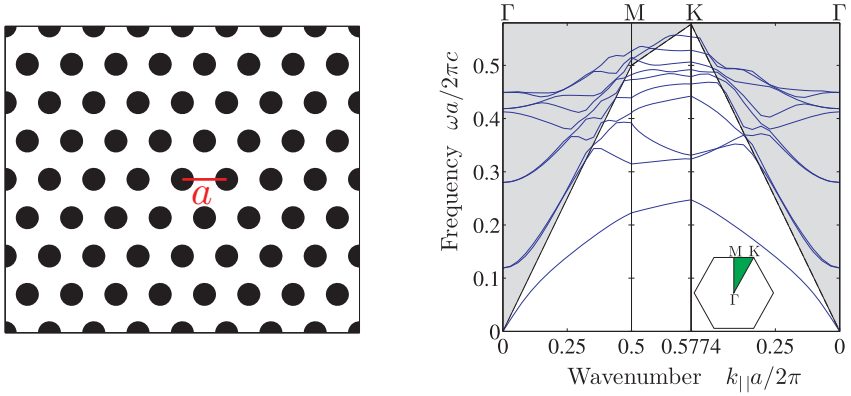

(a) (b)

Figure 1.2: (a) Top view of a photonic crystal with a triangular lattice. The distance between holes is called the lattice constant and is represented by a. (b) Band diagram of a PC membrane with a thickness of $d=0.8a$ and hole radii $r_0=0.26a$. The frequency of the modes (solid blue) is plotted as a function of the in-plane k-vector around the edge of the irreducible Brillouin zone of a triangular lattice shown in the inset. The gray area shows regions of evanescent modes, which cannot propagate inside the crystal.

In Fig. 1.2(b), we show the corresponding band diagram calculated using a plane wave expansion method [15]. The modes (solid blue) are even with respect to reflections in the mirror plane $z=0$, and are usually referred to as TE-like [13]. The abscissa shows the length of the in-plane wave vector $k_{||}$ around the edge of the irreducible Brillouin zone [13], see inset. The lattice constant a is defined as the distance between holes and c is the speed of light in vacuum. The modes that are confined to the membrane lie below the light line defined by $\omega=k_{||}c/n_{\mathrm{R}}$ (white area in Fig. 1.2(b)), where n_{R} is the real part of the refractive index of the semiconductor material. It is observed that a band gap for the confined modes exists for normalized frequencies in the range [0.247; 0.315]. The size and location of this gap depends on the refractive index of the material, the hole size, and the membrane thickness. Above the light line (gray area in Fig. 1.2(b)) the modes are evanescent and decay exponentially with propagation distance inside the crystal.

As mentioned above, one may create waveguides and traps for light having frequencies within the band gap by shifting, removing, or changing the shape

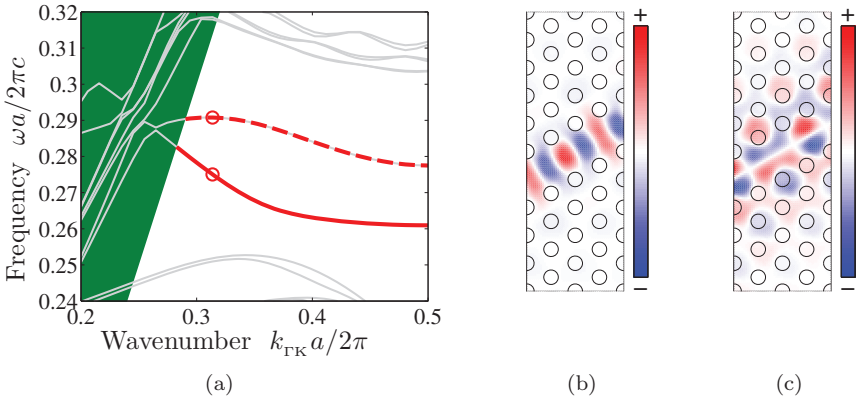

Figure 1.3: (a) Band diagram of a PC membrane $W1$ line-defect waveguide with a thickness of $d = 0.8a$ and hole radii $r_0 = 0.26a$. Two guided modes appear in the band gap of the infinite structure, which have even (solid red) or odd (dashed red) symmetry with respect to reflections in the mirror-plane constituted by the central axis of the waveguide. (b) Magnetic field H_z of the even mode at the point indicated by a circle on the solid red line in (a). (c) Magnetic field H_z of the odd mode at the point indicated by a circle on the dashed red line in (a).

or radii of the holes in the membrane. All these degrees of freedom offer a lot of potential for controlling the behavior of light and creating integrated optical circuits. By removing one line of holes along the Γ-K direction (see inset in Fig. 1.2(b)), one may create a so-called $W1$ line-defect waveguide. The abbreviation $W1$ signifies that the width of the waveguide corresponds to the removal of one row of holes. In Fig. 1.3(a), the band diagram of such a waveguide is shown. The irreducible Brillouin zone of the line-defect crystal is slightly different from that of the infinite structure in Fig. 1.2(b) [16], and all information about the dispersion is contained in the interval $k_{\Gamma M} \in [0; 0.5]$. The solid and dashed red curves correspond to modes, which are well confined to the waveguide and they are either even (solid) or odd (dashed) with respect to reflections in the mirror-plane of the waveguide (axis at the center of the line-defect). The magnetic field distributions of the modes are shown in Figs. 1.3(b) and 1.3(c). The even mode is observed to be confined more tightly than the odd mode at the chosen point on the dispersion curve indicated by circles in Fig. 1.3(a).

The last building block of the switching structures is a cavity, which is created by introducing a localized defect into the PC. Fig. 1.4 shows an example of a so-called H0 cavity [17], which is formed by shifting two neighboring holes away from each other. The resulting defect in the PC lattice gives rise to a lo-

calized mode, which is confined to a very small volume, as observed in Fig. 1.4. The field enhancement inside this small region increases the strength of nonlinear effects, which is needed for the switching application. This issue is addressed in the next section, where the principle of the switching operation is described in more detail.

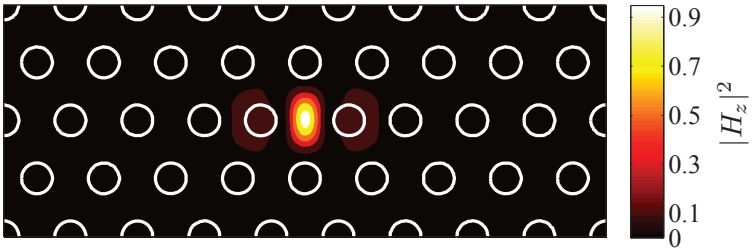

Figure 1.4: Top view of an H0 cavity structure with the mode profile $|H_z|$ superimposed. The cavity is formed by shifting two neighboring holes apart horizontally, which creates a defect in the PC lattice, where the field may be trapped. The mode distribution is normalized to a peak value of 1.

1.4 Principle of Switching

A generic sketch of the type of structure we consider throughout this thesis is shown in Fig. 1.5(a). It consists of a cavity, which may trap the electromagnetic field resulting in a significant field enhancement. The cavity supports a discrete set of eigenmodes that oscillate at the eigenfrequencies ω_n. The energy in these modes decays by different mechanisms, such as material absorption, scattering into radiation modes, and coupling to the adjacent waveguides (denoted Port 1 and 2 in Fig. 1.5(a)). The decay due to waveguide coupling is described by parameters d_{mn}, which denote coupling from the mth port to the nth resonance. All the decay mechanisms, which are not related to waveguide coupling are accounted for by the γ_{loss} parameter in Fig. 1.5(a). Direct scattering between the ports is also possible and this process is illustrated by the dashed line and the t_1 parameter. The fields in the cavity and waveguides are described by $A(t)$ and $S_{m\pm}(t)$, where + (-) denotes an input (output) field. The physical interpretation of these parameters is treated in Section 2.2.

To understand how we can perform signal processing with this type of structure, it is convenient to think of the cavity as an optical filter. Let us consider the case of a single resonance coupled to two ports and no direct scattering path between the ports ($|t_1| = 0$ in Fig. 1.5(a)). The only pathway for the light between the ports is through the cavity, and since only frequencies close to the resonance can couple into the cavity, it acts as a bandpass filter (BPF). This is illustrated in Fig. 1.5(b), where the transmission spectrum of the filter

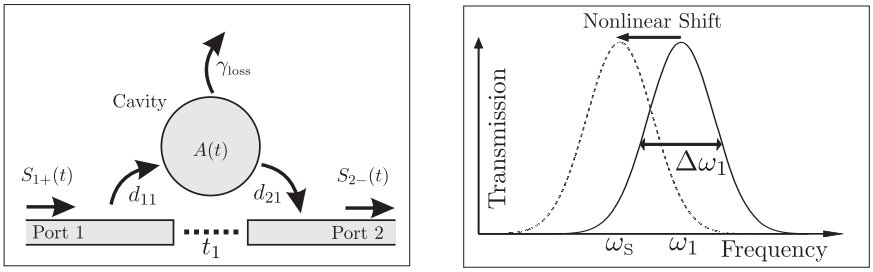

Figure 1.5: (a) Generic illustration of the cavity-waveguide structures considered in this thesis. The fields propagating through the waveguides may couple into the cavity or scatter directly to the other waveguides. (b) Example of the transmission spectrum of light propagating from Port 1 to Port 2 through the cavity. The resonance frequency and linewidth of the cavity are ω_1 and $\Delta\omega_1$, and ω_S represents the center frequency of the signal. The presence of a pump field will change the refractive index through a nonlinear interaction, which shifts the resonance and thereby the transmission spectrum as illustrated.

is shown (solid black) and ω_1 is the resonance frequency. If the transmission properties of the filter can be modified by some external influence, the structure may act as a switch. Since we only consider all-optical switching, the external influence is an electromagnetic field, which we shall denote control or pump. In Fig. 1.5(b), the dashed curve illustrates an example of the resonance frequency being shifted due to the presence of the pump. If a signal with a center frequency ω_S is coupled into port 1, it is seen that the transmission of the signal changes from a small to a large value with the presence of the pump. The pump may thus open or close the switch for the signal, depending on the detuning of the signal from the cavity resonance. The change of the filter transmission properties relies on a nonlinear interaction with the pump, and thus, it usually requires large intensities to achieve a significant switching contrast (defined as the ratio between the signal energy passing through the filter in the open and closed state).

The advantage of using a cavity structure is that the field energy may be confined to very small volumes, which drastically increases the intensity and thereby the nonlinear interaction. Simultaneously, the photon lifetime in the cavity can be large, which increases the interaction time and thereby also reduces the requirements on the pump energy. The photon lifetime is usually expressed via the cavity quality factor Q, defined as the ratio between the stored optical energy and the dissipated power during one oscillation at the cavity resonance frequency $Q = \omega_n U_n / P_n$ [13]. A high Q therefore corresponds to a long photon lifetime and a larger interaction. The Q is also often related to the cavity linewidth $\Delta\omega_n$, defined as the full width at half maximum (FWHM)

of the transmission spectrum seen in Fig. 1.5(b), $Q = \omega_n/\Delta\omega_n$. The photon lifetime may be defined as $\tau_{\mathrm{ph}} = 1/\Delta\omega_n$. Using PC membrane structures has been shown to facilitate cavities with extremely large Q/V ratios [18, 19]. A strict definition of the cavity mode volume is somewhat subtle [20], but the important point is that the field enhancement increases with increased confinement signified by a small mode volume. The small size of the cavity structure is also important for optical integration, where footprint is a key consideration.

All-optical switching has been demonstrated using many different structures and materials such as silicon waveguides [21] and micro rings [22], PC cavities [23, 24] and Mach-Zehnder interferometers [25], semiconductor optical amplifiers (SOAs) [26–28], and parametric processes in fibers [29, 30]. We may distinguish between switches operating by use of a resonance, like silicon micro rings or PC cavities, and switches based on cross phase- or cross gain modulation, like Mach-Zehnder interferometers or SOAs. As explained above, the resonance based switches have advantages in terms of energy consumption and footprint. Their most significant drawbacks are related to the fact that large switching contrasts are only achievable in a very limited wavelength range close to the cavity resonance. This range is denoted the operation bandwidth. It causes an undesirable sensitivity to temperature fluctuations, which may shift the cavity resonance considerably relative to the operation bandwidth. It also poses limitations on the flexibility of the device for use in e.g. WDM systems. If the cavity linewidth $\Delta\omega_n$ is small compared to the bandwidth of the incoming signal, the transmission in the open state drops and decreases the signal to noise ratio of the outgoing signal. Thus, there is a trade-off between the switching energy and signal bandwidth, which we shall discuss in more detail in Chapter 7.

The other class of switches do not suffer from as severe operation bandwidth limitations, however, they cannot be made as small as the cavity structures. This is due to the absence of a strong field enhancement, which must be compensated by a longer interaction length and thereby larger size. For these types of structures, PC designs are also able to improve the performance by slow light waveguides [31], where the effective interaction length is increased by the slow down factor. This happens at the expense of a decrease in operation bandwidth and increased scattering loss due to fabrication imperfections, so a compromise can be made utilizing semi-slow light waveguides [32, 33].

Devices based on optical fibers are robust, stable, and easily compatible with existing fiber components. However, they usually require large pump energies and bulky components, which makes them unsuited for integration at the micro meter scale.

Since both classes of switches have their strengths and weaknesses, it must be decided from system application and requirement considerations, which one is most suited. In this thesis, we exclusively investigate cavity based PC structures.

The material nonlinearities that facilitate switching may originate from a range of physical mechanisms. In semiconductor crystals the Kerr effect and carrier induced nonlinearities are used to affect the refractive index as well as the gain of the material. Carriers are generated by linear- or higher order absorption, depending on the wavelength of the pump relative to the electronic band gap of the semiconductor. Changes in the real and imaginary part of the refractive index are always related due to causality, which is expressed in the Kramers-Kronig relations [34]. There are several effects, such as band filling, band gap shrinkage, and free carrier absorption [35], which are responsible for changes in the complex refractive index due to the generation of free carriers.

Carrier induced nonlinearities are governed by time scales, such as the non-radiative recombination rate, which may be on the order of hundreds of picoseconds. The Kerr nonlinearity, on the other hand, has a response time in the femtosecond range, making it possible for the switch to reset much faster. However, it takes a much stronger pump field to produce the same index change using the Kerr effect as with carrier induced effects.

Lower dimensional semiconductor structures such as quantum wells or quantum dots have special nonlinear properties due to their significantly different density of electronic states. This allows for saturation effects down to the single photon level for quantum dots [36]. The relaxation dynamics of these structures may also exhibit different behavior than devices based on bulk material.

Again, the choice of nonlinear mechanism depends on the application and system requirements under consideration. In this thesis, we only focus on the Kerr effect and free carrier effects of bulk InP.

1.5 Overview of the Thesis

The first chapter of the thesis introduces the mathematical model, which is employed to describe the physics of waveguide-cavity structures. This model is well-known from the literature, and the treatment in Chapter 2 only provides a brief overview.

The simple model considered in the first chapter assumes that nonlinear effects can be introduced as perturbations of the resonance frequency and decay rate of the cavity modes. In Chapter 3 we discuss how to calculate these perturbations using a rigorous theory suitable for open systems that leak energy into their surroundings. The theory is based on the previous work contained in Refs. [37–39].

A considerable part of the work in the thesis is concerned with the design of PC membrane structures, and Chapter 4 contains a general discussion of this topic. An example of a two port structure is given, which has been studied previously in the literature [23, 24]. A similar device is used in the experiments described in Chapter 5. All the measurements presented in the thesis were done

in collaboration with Alfredo de Rossi and Sylvain Combrié and were carried out during a visit at Thales Research and Technology in France.

Chapter 6 contains a description of a more advanced structure with separate ports for the signal and pump fields. The reasoning for considering such a structure is, in part, to avoid the difficulties in measuring the cavity dynamics, which are described in Chapter 5. The separation of the pump and signal is believed to better represent the way a switch would be implemented in an integrated optical circuit, and it offers important flexibility in controlling the optical environment for the signal and pump independently.

Chronologically, the work in Chapter 7 predates that of the first chapters, but conceptually it follows Chapter 6. It contains an analysis of the cavity dynamics of a four port structure with a Kerr nonlinearity. In particular, it is devoted to a consideration of the trade-off between energy consumption and bandwidth in high speed OTDM systems, where patterning effects are important to take into account. The bandwidth limitation of the device originates solely from the photon lifetime of the cavity when only the Kerr effect is considered.

The understanding of the cavity dynamics obtained from the analysis in Chapter 7 has helped to form the basis of the proposed methods of reducing the switching energy, which are presented in the last two chapters of the thesis. The first method is concerned with the optical properties of the cavity and how the transmission spectrum may be modified to exhibit a stronger dependence on frequency. The idea of using Fano resonances for this purpose originates from Ref. [40], and Chapter 8 provides a simple design concept for producing such resonances in both two and four port structures. An extensive analysis of the advantages compared to the more well-known Lorentzian line shape is also contained in this chapter.

Finally, in Chapter 9, it is considered how controlling the optical properties of the input fields may yield a reduction in switching energy. A general mathematical method is employed, which provides the means for calculating the optimum amplitude and phase of the input in order to optimize a prescribed quantity, such as the optical energy inside the cavity. An example is given, which shows that the cavity energy may be changed arbitrarily fast.

The very last chapter contains a summary of the most important conclusions and a discussion of interesting directions, in which the work may be continued.

2

Model Formalism

2.1 Introduction

In this chapter the mathematical framework of the model used to describe the switching structures is laid out. In the first section, we start from Maxwell's equations and consider a modal expansion of the field, which leads to the temporal coupled mode theory (TCMT). The last section contains a general formulation of this model, which simplifies the description of the system from a partial differential equation (PDE) to a set of ordinary differential equations (ODEs).

2.2 Temporal Coupled Mode Theory

Let us begin by introducing some notation for the electromagnetic fields. Maxwell's equations are given by [41]

$$\nabla \times \vec{\mathcal{E}}(\mathbf{r},t) = -\frac{\partial \vec{\mathcal{B}}(\mathbf{r},t)}{\partial t} \tag{2.2.1a}$$

$$\nabla \times \vec{\mathcal{H}}(\mathbf{r},t) = \frac{\partial \vec{\mathcal{D}}(\mathbf{r},t)}{\partial t} + \vec{\mathcal{J}}(\mathbf{r},t) \tag{2.2.1b}$$

$$\nabla \cdot \vec{\mathcal{B}}(\mathbf{r},t) = 0 \tag{2.2.1c}$$

$$\nabla \cdot \vec{\mathcal{D}}(\mathbf{r},t) = \rho(\mathbf{r},t), \tag{2.2.1d}$$

where $\vec{\mathcal{E}}$ and $\vec{\mathcal{B}}$ are the electric and magnetic fields, $\vec{\mathcal{D}}$ and $\vec{\mathcal{H}}$ are the electric displacement and magnetic induction fields, and $\vec{\mathcal{J}}$ and ρ are the free current and charge density. Spatial position and time are denoted by $\mathbf{r}$ and t, respectively.

The fields are related by the relations

$$\vec{\mathcal{D}} = \epsilon_0 \vec{\mathcal{E}} + \vec{\mathcal{P}} \tag{2.2.2a}$$

$$\vec{\mathcal{H}} = \frac{1}{\mu_0}\vec{\mathcal{B}} - \vec{\mathcal{M}}, \tag{2.2.2b}$$

where $\vec{\mathcal{P}}$ and $\vec{\mathcal{M}}$ are the polarization and magnetization.

In the TCMT the electric field in the waveguides and cavity are expanded on the eigenmodes of the subsystems. For the cavity, the fields take the form

$$\vec{\mathcal{E}}(\mathbf{r},t) = \sum_{n\in\mathbb{N}} \frac{1}{2}\mathbf{E}_n(\mathbf{r})e^{-i\tilde{\omega}_n t} + \frac{1}{2}\mathbf{E}_n^*(\mathbf{r})e^{i\tilde{\omega}_n t} \tag{2.2.3}$$

$$\vec{\mathcal{H}}(\mathbf{r},t) = \sum_{n\in\mathbb{N}} \frac{1}{2}\mathbf{H}_n(\mathbf{r})e^{-i\tilde{\omega}_n t} + \frac{1}{2}\mathbf{H}_n^*(\mathbf{r})e^{i\tilde{\omega}_n t}. \tag{2.2.4}$$

If it is assumed that the magnetization is zero, we may combine Eqs. (2.2.1a) and (2.2.1b) as well as the relations into the wave equation

$$\nabla\times\nabla\times\vec{\mathcal{E}}(\mathbf{r},t) = -\mu_0\epsilon_0\frac{\partial^2\vec{\mathcal{E}}(\mathbf{r},t)}{\partial t^2} - \mu_0\frac{\partial^2\vec{\mathcal{P}}(\mathbf{r},t)}{\partial t^2} - \mu_0\frac{\partial\vec{\mathcal{J}}(\mathbf{r},t)}{\partial t}. \tag{2.2.5}$$

As a first order approximation, the polarization and current may be assumed to be proportional to the electric field

$$\vec{\mathcal{P}}(\mathbf{r},t) \approx \vec{\mathcal{P}}^{(1)}(\mathbf{r},t) = \epsilon_0\chi^{(1)}(\mathbf{r})\vec{\mathcal{E}}(\mathbf{r},t), \qquad \vec{\mathcal{J}}(\mathbf{r},t) = \sigma(\mathbf{r})\vec{\mathcal{E}}(\mathbf{r},t),$$

where $\chi^{(1)}$ is the first order susceptibility and σ is the conductivity and the material response is assumed to be frequency independent and local. Using these relations and inserting Eq. (2.2.3) into Eq. (2.2.5), an equation for each frequency component is obtained

$$\nabla\times\nabla\times\mathbf{E}_n(\mathbf{r}) - \frac{\tilde{\omega}_n^2}{c^2}\left(\epsilon_{\mathrm{R}}(\mathbf{r}) + i\frac{\sigma(\mathbf{r})}{\epsilon_0\tilde{\omega}_n}\right)\mathbf{E}_n(\mathbf{r}) = 0, \tag{2.2.6}$$

where $\epsilon_{\mathrm{R}} = 1 + \chi^{(1)}$, and we may define $\epsilon_{\mathrm{I}} = \sigma/(\epsilon_0\omega)$. Eq. (2.2.6) combined with appropriate boundary conditions constitute a generalized eigenvalue problem from which $\tilde{\omega}_n$ and $\mathbf{E}_n$ may be determined for a specific structure described by the dielectric function $\epsilon_{\mathrm{r}} \equiv \epsilon_{\mathrm{R}} + i\epsilon_{\mathrm{I}}$. If the cavity is being considered, the appropriate boundary condition is the Silver-Mï¿½ller radiation condition [42]

$$\lim_{|\mathbf{r}|\to\infty}\left[\hat{\mathbf{r}}\times\nabla\times\mathbf{E}_n(\mathbf{r}) + i\frac{\tilde{\omega}_n\sqrt{\epsilon_{\mathrm{B}}}}{c}\mathbf{E}_n(\mathbf{r})\right] = \mathbf{0}. \tag{2.2.7}$$

Eq. (2.2.7) assumes an isotropic background material with dielectric constant ϵ_{B} at very large distances. This boundary condition takes into account the lossy nature of the cavity even in the absence of absorption $\epsilon_{\mathrm{I}} = 0$ and generally

yields complex eigenvalues $\tilde{\omega}_n = \omega_n - i\gamma_m$. The electric field may be normalized as $\mathbf{E}_n = A_0\tilde{\mathbf{f}}_n(\mathbf{r})$, where $\tilde{\mathbf{f}}_n$ is also a solution of Eq. (2.2.6). Let us consider a case where the current term in Eq. (2.2.5) describes a source with a center frequency close to one of the cavity modes and a spectrum, which is narrow compared with the smallest distance to a neighboring eigenfrequency. If it is located far away from the region of space comprised by the cavity, we may assume that the coefficient A_0 is time dependent and write the real electric field as

$$\vec{\mathcal{E}}(\mathbf{r},t) = \sum_{n\in\mathbb{N}} \frac{1}{2}A_n(t)\tilde{\mathbf{f}}_n(\mathbf{r}) + \frac{1}{2}A_n^*(t)\tilde{\mathbf{f}}_n^*(\mathbf{r}). \tag{2.2.8}$$

The spatial distribution of the mode $\tilde{\mathbf{f}}_n$ is assumed still to be a solution to Eq. (2.2.6) and only the amplitudes A_n change due to the driving field. The simplification that the TCMT provides is to reduce the problem of solving a PDE to solving only an ODE for the amplitudes A_n. In other words, from having solved Eqs. (2.2.6) and (2.2.7) only once for the modes $\tilde{\mathbf{f}}_n$ using e.g. finite difference time domain (FDTD) simulations, the response to any time dependent driving field is contained in the solution of the ODE for $A_n(t)$. In the absence of a source term, the equation is

$$\frac{dA_n(t)}{dt} = -i\tilde{\omega}_n A_n(t).$$

The solution $A_n(t) = A_0\exp(-i\tilde{\omega}_n t)$ renders Eqs. (2.2.3) and (2.2.8) identical, which must be the case. With an external driving field, the equation becomes

$$\frac{dA_n(t)}{dt} = -i\tilde{\omega}_n A_n(t) + \sqrt{\gamma}S(t).$$

The driving field $S(t)$ is added phenomenologically, and γ is a number describing the efficiency at which energy is transferred between the cavity and the source.

Let us consider the normalization of the modes. It is a common convention in the literature to normalize the field, so that the energy in each mode is given by $|A_n|^2$ [13]. To see the consequence of this, we consider the time averaged electromagnetic energy in the cavity [43]

$$\langle U\rangle = \frac{1}{4}\mathrm{Re}\left\{\int_{V_{\mathrm{cav}}} \epsilon_0\epsilon_{\mathrm{r}}(\mathbf{r})|\vec{\mathcal{E}}|^2 + \mu_0|\vec{\mathcal{H}}|^2 dV\right\} = \frac{1}{4}\sum_{n\in\mathbb{N}}|A_n|^2\mathrm{Re}\left\{\int_{V_{\mathrm{cav}}} \epsilon_0\epsilon_{\mathrm{r}}(\mathbf{r})|\tilde{\mathbf{f}}_n|^2 + \frac{\mu_0}{|\tilde{\omega}_n|^2}|\nabla\times\tilde{\mathbf{f}}_n|^2 dV\right\}. \tag{2.2.9}$$

It is seen that if $\langle U\rangle = \sum_{n\in\mathbb{N}} U_n$ and $U_n = |A_n|^2$, then the modes must be normalized as

$$\frac{1}{4}\mathrm{Re}\left\{\int_{V_{\mathrm{cav}}} \epsilon_0\epsilon_{\mathrm{r}}(\mathbf{r})|\tilde{\mathbf{f}}_n|^2 + \frac{\mu_0}{|\tilde{\omega}_n|^2}|\nabla\times\tilde{\mathbf{f}}_n|^2 dV\right\} = 1. \tag{2.2.10}$$

The region of space comprised by the cavity is also defined by Eq. (2.2.10) and we denote its volume V_{cav}. We note that this volume does not correspond to the mode volume of the cavity [20]. It is simply the region of space, where the optical energy appearing in the TCMT equations is calculated. A more detailed discussion of this volume is contained in Section 3.3.1.

2.2.1 TCMT Equations

We shall use a formulation of the coupled mode theory equations based on Ref. [44]. It treats a general case of m ports coupled to n resonances, where the TCMT equations are given by

$$\frac{d\mathbf{A}}{dt} = (-i\mathbf{\Omega} - \mathbf{\Gamma})\mathbf{A} + \mathbf{K}^T|S_+\rangle \tag{2.2.11}$$

$$|S_-\rangle = \mathbf{C}|S_+\rangle + \mathbf{D}\mathbf{A}. \tag{2.2.12}$$

The matrix $\mathbf{\Omega}$ is an $n \times n$ diagonal matrix with elements describing the individual resonances. The diagonal elements of the $n \times n$ matrix $\mathbf{\Gamma}$ account for the energy decay of the modes, whereas the off-diagonal elements relate to coupling between different resonances. The $m \times n$ matrices $\mathbf{K}$, and $\mathbf{D}$ describe coupling between the ports and waveguides, while the $m \times m$ scattering matrix $\mathbf{C}$ accounts for direct coupling between the ports. It is assumed to be symmetric and unitary, which is the case in a lossless and reciprocal system. In Ref. [44] the following identities are proven

$$\mathbf{D}^\dagger\mathbf{D} = 2\mathbf{\Gamma} \tag{2.2.13}$$

$$\mathbf{K} = \mathbf{D} \tag{2.2.14}$$

$$\mathbf{C}\mathbf{D}^* = -\mathbf{D}, \tag{2.2.15}$$

where † (*) means hermitian (complex) conjugate. If the entire system of resonances and ports is considered, energy will be conserved and $\mathbf{\Omega}$ and $\mathbf{\Gamma}$ are Hermitian matrices. The presence of material loss or loss to radiation modes can be introduced phenomenologically by splitting $\mathbf{\Gamma}$ into two parts $\mathbf{\Gamma} = \mathbf{\Gamma}_{\mathrm{port}} + \mathbf{\Gamma}_{\mathrm{loss}}$, where Eq. (2.2.13) applies only to $\mathbf{\Gamma}_{\mathrm{port}}$ [44]. The elements of the matrix $\mathbf{D}$ are complex numbers $d_{mn} = |d_{mn}| \exp(i\theta_{mn})$.

Let us consider an example of a single resonance coupled to two ports. The matrices of the equation system are

$$\mathbf{\Omega} = \omega_1, \quad \mathbf{\Gamma}_{\mathrm{port}} = \gamma_1, \quad \mathbf{D} = \begin{bmatrix} d_1 \\ d_2 \end{bmatrix}, \quad \mathbf{C} = \begin{bmatrix} r_1 & t_1 \\ t_1 & r_1 \end{bmatrix}. \tag{2.2.16}$$

If we assume an odd mirror symmetry of the cavity mode with respect to a vertical plane dividing the cavity in Fig. 1.5(a) in two equally sized parts, the coupling coefficients are related by $d_1 = -d_2$. From Eq. (2.2.13) it follows that

$|d_1| = \sqrt{\gamma_1}$, and Eq. (2.2.15) results in the relation

$$(r_1 - t_1)d_1^* = -d_1 \;\Rightarrow\; (r_1 - t_1)|d_1|e^{-i\theta_1} = -|d_1|e^{i\theta_1} \;\Rightarrow\; r_1 - t_1 = -e^{i2\theta_1}.$$

Because $\mathbf{C}$ is unitary, the identities $|r_1|^2 + |t_1|^2 = 1$ and $r_1 t_1^* + t_1 r_1^* = 0$ hold, which also leads to $|r_1 + t_1| = 1$ and $|r_1 - t_1| = 1$. By combining these expressions, we can relate the real and imaginary parts of r_1 and t_1

$$r_1 - t_1 = -e^{i2\theta_1} \quad \Rightarrow \quad r_1 = t_1 - e^{i2\theta_1} \quad \Rightarrow \quad |2t_1 - e^{i2\theta_1}| = 1. \tag{2.2.17}$$

Let us introduce the variable $t_1' = t_1 e^{-i2\theta_1} = |t_1|e^{i\phi_{t_1'}}$. By substitution we get

$$|2t_1' - 1| = 1 \quad \Rightarrow \quad 4|t_1'|^2 + 1 - 4\mathrm{Re}\{t_1'\} = 1 \quad \Rightarrow \quad |t_1'| = \cos(\phi_{t_1'}) \quad \Rightarrow$$
$$t_1' = |t_1'|\left(\cos[\phi_{t_1'}] + i\sin[\phi_{t_1'}]\right) = |t_1'|\left(\cos[\mathrm{acos}(|t_1'|)] + i\sin[\mathrm{acos}(|t_1'|)]\right).$$

If the cavity mode is even ($d_1 = d_2$), we find in a similar manner

$$t_1' = |t_1'|\left(-\cos[\mathrm{acos}(|t_1'|)] + i\sin[\mathrm{acos}(|t_1'|)]\right).$$

By using identities from trigonometry, a general expression may be written as

$$t_1' = -|t_1'|\left(\pm|t_1'| - i\sqrt{1 - |t_1'|^2}\right), \tag{2.2.18}$$

where the upper sign in $\pm$ corresponds to an even cavity mode, and the lower to an odd mode. The reflectivity is given by $r_1' = \mp t_1' - 1$ using the same sign convention for even and odd modes. To find the transmission spectrum of the system, we solve Eqs. (2.2.11) and (2.2.12) either by Fourier transformation or simply by assuming that A and $|S_\pm\rangle$ are plane waves of angular frequency ω. If S_{2+} is zero, we have

$$-i\omega A' = (-i\omega_1 - \gamma_1 - \gamma_{\mathrm{loss}})A' + \sqrt{\gamma_1}e^{i\theta_1}S_{1+}'$$
$$S_{2-}' = t_1 S_{1+}' \pm \sqrt{\gamma_1}e^{i\theta_1}A'.$$

Let us multiply the first equation by $\exp(-i\theta_1)$ and the second by $\exp(-i2\theta_1)$. By defining the new fields $A = A'\exp(-i\theta_1)$ and $S_{n\pm} = S_{n\pm}'\exp(-i2\theta_1)$ as well as the detuning $\delta_1 = \omega_1 - \omega$ and total decay rate $\gamma_{\mathrm{C}} = \gamma_1 + \gamma_{\mathrm{loss}}$, we have

$$0 = (-i\delta_1 - \gamma_{\mathrm{C}})A + \sqrt{\gamma_1}S_{1+}$$
$$S_{2-} = t_1' S_{1+} \pm \sqrt{\gamma_1}A.$$

The continuous wave (CW) transmission is then given by

$$T_{\mathrm{CW}}(\delta_1) = \frac{|S_{2-}|^2}{|S_{1+}|^2} = \left|t_1' \pm \frac{\gamma_1}{i\delta_1 + \gamma_{\mathrm{C}}}\right|^2 =$$
$$\left|-|t_1|^2 \pm i|t_1|\sqrt{1 - |t_1|^2} + \frac{\gamma_1}{i\delta_1 + \gamma_{\mathrm{C}}}\right|^2. \tag{2.2.19}$$

Again, the upper (lower) sign corresponds to an even (odd) mode. If $t'=0$ the transmission is symmetric around $\delta_1 = 0$ and has one extremum corresponding to a maximum. For $t'=1$ the same holds, only the extremum is a minimum. The transmission is asymmetric for $|t_1| \in \,]0;1[$ and has both a maximum and a minimum. Let us define the slowly varying fields $a(t)$ and $s(t)$ by the relations

$$A(t) = a(t)e^{-i\omega_{\mathrm{L}}t} \quad \text{and} \quad S(t) = s(t)e^{-i\omega_{\mathrm{L}}t}. \tag{2.2.20}$$

The dynamical equations for these fields are given by

$$\frac{da(t)}{dt} = (-i\delta_{\mathrm{L}} - \gamma_{\mathrm{C}})a(t) + \sqrt{\gamma_1}s_{1+}(t) \tag{2.2.21}$$

$$s_{1-}(t) = r_1' s_{1+}(t) \mp \sqrt{\gamma_1}a(t) \tag{2.2.22}$$

$$s_{2-}(t) = t_1' s_{1+}(t) \pm \sqrt{\gamma_1}a(t), \tag{2.2.23}$$

where $\delta_{\mathrm{L}} = \omega_1 - \omega_{\mathrm{L}}$. These equations will be used repeatedly throughout the thesis.

3

Perturbation Theory

3.1 Introduction

The temporal coupled mode theory (TCMT) equations of the last chapter are linear, and cannot account for the optical switching mechanism, which requires a nonlinear interaction to transfer the influence of the pump onto the signal. It is commonly assumed that nonlinear effects causing changes in the complex refractive index of the material can be included in the TCMT as perturbations of the real and imaginary part of the complex eigenfrequency [45]. This chapter contains a treatment of the perturbation theory, which is needed to relate changes in the dielectric function to changes in the eigenvalue of Eq. (2.2.6). In the literature, this problem is often assumed to constitute a Hermitian eigenvalue problem with real eigenvalues [46,47]. However, the cavity must exchange energy with the waveguides, and there will always be some finite leakage of the energy out of the membrane into radiation modes. This means that the problem is inherently non-Hermitian and the eigenvalues are complex. The proper perturbation theory for such systems is described in Refs. [37–39]. We perform the necessary calculations below and in Appendix A. The basic difference between the result obtained here, and that obtained from assuming a Hermitian eigenvalue problem, is the non-zero surface terms of the integration in e.g. Eq. (A.1.4).

The chapter is divided into three sections, where the first treats a general perturbation of the dielectric function, and the following provide examples for the Kerr effect and free carrier induced effects.

3.2 General Case

Let us consider the wave equation again, and include a small perturbation of the dielectric function $\Delta\epsilon_{\mathrm{r}}$

$$\nabla \times \nabla \times \mathbf{E} - \frac{\tilde{\omega}^2}{c^2} \left[\epsilon_r + \zeta \Delta\epsilon_{\mathrm{r}}(\mathbf{E})\right] \mathbf{E} = \mathbf{0},$$

where we have dropped the subscripts compared to Eq. (2.2.6) and introduced the perturbation parameter ζ, which is used to expand the eigenfrequencies and modes

$$\mathbf{E} = \sum_{j=0} \zeta^j \mathbf{E}^{(j)} \quad , \quad \tilde{\omega} = \sum_{j=0} \zeta^j \tilde{\omega}^{(j)}. \tag{3.2.1}$$

In the absence of the perturbation, the equation is seen to be

$$\nabla \times \nabla \times \mathbf{E}^{(0)} - \frac{(\tilde{\omega}^{(0)})^2}{c^2} \epsilon_r \mathbf{E}^{(0)} = \mathbf{0}. \tag{3.2.2}$$

Let us collect terms up to first order in ζ

$$\nabla \times \nabla \times (\mathbf{E}^{(0)} + \zeta \mathbf{E}^{(1)}) - \frac{\left(\tilde{\omega}^{(0)} + \zeta \tilde{\omega}^{(1)}\right)^2}{c^2} \epsilon_r \left(\mathbf{E}^{(0)} + \zeta \mathbf{E}^{(1)}\right) \zeta \Delta\epsilon_{\mathrm{r}}(\mathbf{E}^{(0)} + \zeta \mathbf{E}^{(1)}) = \mathbf{0}$$

For $\zeta = 0$, we see that Eq. (3.2.2) is recovered. Collecting all terms proportional to ζ, we have

$$\nabla \times \nabla \times \mathbf{E}^{(1)} - \frac{2\tilde{\omega}^{(0)}\tilde{\omega}^{(1)}}{c^2} \epsilon_r \mathbf{E}^{(0)} - \frac{(\tilde{\omega}^{(0)})^2}{c^2} \epsilon_r \mathbf{E}^{(1)} - \frac{(\tilde{\omega}^{(0)})^2}{c^2} \Delta\epsilon_{\mathrm{r}}(\mathbf{E}^{(0)}) \mathbf{E}^{(0)} = \mathbf{0}. \tag{3.2.3}$$

In Appendix A.1 it is shown that the first order correction to the eigenfrequency, for a field obeying the boundary condition in Eq. (2.2.7), is given by

$$\tilde{\omega}^{(1)} = -\frac{1}{2} \tilde{\omega}^{(0)} \frac{\int_V \Delta\epsilon_{\mathrm{r}} \mathbf{E}^{(0)} \cdot \mathbf{E}^{(0)} dV}{\int_V \epsilon_{\mathrm{r}} \mathbf{E}^{(0)} \cdot \mathbf{E}^{(0)} dV + i \frac{c\sqrt{\epsilon_{\mathrm{B}}}}{2\tilde{\omega}^{(0)}} \int_{\partial V} \left(\mathbf{E}^{(0)} \cdot \mathbf{E}^{(0)}\right) \hat{\mathbf{r}} \cdot d\mathbf{A}}.$$

3.3 Kerr Effect

In this section we calculate the first order correction to the eigenfrequency in cases, where the polarization includes terms of higher order in the electric field. The semiconductor materials we consider have no second order response due to inversion symmetry [34], so the polarization includes only the first and third order susceptibility

$$\vec{\mathcal{P}}(\mathbf{r}, t) \approx \epsilon_0 \chi^{(1)}(\mathbf{r}) \vec{\mathcal{E}}(\mathbf{r}, t) + \vec{\mathcal{P}}^{(3)}(\mathbf{r}, t).$$

The third order polarization is expanded like $\vec{\mathcal{E}}$ and $\vec{\mathcal{H}}$ in Eqs. (2.2.3) and (2.2.4)

$$\vec{\mathcal{P}}^{(3)}(\mathbf{r},t) = \sum_{n\in\mathbb{N}} \frac{1}{2}\mathbf{P}_n^{(3)}(\mathbf{r},\tilde{\omega}_n)e^{-i\tilde{\omega}_n t} + \frac{1}{2}\mathbf{P}_n^{(3)}(\mathbf{r},-\tilde{\omega}_n)e^{i\tilde{\omega}_n t}. \tag{3.3.1}$$

By including this extra term in Eq. (2.2.5), the right hand side (RHS) consists of the nonlinear polarization

$$\nabla\times\nabla\times\mathbf{E}_n(\mathbf{r}) - \frac{\tilde{\omega}_n^2\epsilon_{\mathrm{r}}(\mathbf{r})}{c^2}\mathbf{E}_n(\mathbf{r}) = \frac{\tilde{\omega}_n^2}{c^2}\mathbf{P}_n^{(3)}(\mathbf{r}). \tag{3.3.2}$$

The details of the perturbation calculation are carried out in Appendix A.2 and the first order change in the eigenfrequency is given by Eq. (A.2.4). Using Eq. (2.2.8), the result in Eq. (A.2.4) may be written in terms of the mode function $\tilde{\mathbf{f}}_n$

$$\tilde{\omega}^{(1)}(t) = -\frac{3}{8}\tilde{\omega}^{(0)}|A(t)|^2\frac{\int_V \chi^{(3)}(\mathbf{r})|\tilde{\mathbf{f}}_n(\mathbf{r})|^2\tilde{\mathbf{f}}_n(\mathbf{r})\cdot\tilde{\mathbf{f}}_n(\mathbf{r})dV}{\langle\langle\tilde{\mathbf{f}}_n|\tilde{\mathbf{f}}_n\rangle\rangle},$$

where

$$\langle\langle\tilde{\mathbf{f}}_n|\tilde{\mathbf{f}}_n\rangle\rangle = \int_V \epsilon_{\mathrm{r}}(\mathbf{r})\tilde{\mathbf{f}}_n\cdot\tilde{\mathbf{f}}_n dV + i\frac{c\sqrt{\epsilon_{\mathrm{B}}}}{2\tilde{\omega}^{(0)}}\int_{\partial V}\left(\tilde{\mathbf{f}}_n\cdot\tilde{\mathbf{f}}_n\right)\hat{\mathbf{r}}\cdot d\mathbf{A}.$$

In general, the third order susceptibility may be considered to be complex $\chi^{(3)} = \chi_{\mathrm{R}}^{(3)} + i\chi_{\mathrm{I}}^{(3)}$ with a real part that is related to the Kerr effect and an imaginary part, which is related to two photon absorption (TPA). We may define an effective (generally complex) volume

$$\frac{1}{V_\chi} = \frac{3}{8}\frac{\epsilon_0\int_V f_\epsilon(\mathbf{r})|\tilde{\mathbf{f}}_n(\mathbf{r})|^2\tilde{\mathbf{f}}_n(\mathbf{r})\cdot\tilde{\mathbf{f}}_n(\mathbf{r})dV}{\langle\langle\tilde{\mathbf{f}}_n|\tilde{\mathbf{f}}_n\rangle\rangle}, \tag{3.3.3}$$

where the function $f_\epsilon(\mathbf{r})$ equals 1 inside the nonlinear material and 0 in the background material, such that $\chi^{(3)}(\mathbf{r}) = \chi^{(3)}f_\epsilon(\mathbf{r})$. By introducing this notation, the effective volume V_χ is only dependent on the structural parameters. The real and imaginary contributions to the perturbation may be written as

$$\tilde{\omega}^{(1)}(t) = \left(-K_{\mathrm{Kerr}} - iK_{\mathrm{TP}}\right)|A(t)|^2,$$

where

$$K_{\mathrm{Kerr}} = \mathrm{Re}\left\{\frac{\tilde{\omega}^{(0)}\chi^{(3)}}{\epsilon_0 V_\chi}\right\} \quad \text{and} \quad K_{\mathrm{TP}} = \mathrm{Im}\left\{\frac{\tilde{\omega}^{(0)}\chi^{(3)}}{\epsilon_0 V_\chi}\right\}. \tag{3.3.4}$$

By including these perturbative corrections to the eigenfrequency in Eq. (2.2.21), we have

$$\frac{da(t)}{dt} = -i\left[\delta_{\mathrm{L}} - K_{\mathrm{Kerr}}|a(t)|^2\right]a(t) - \left[\gamma_{\mathrm{C}} + K_{\mathrm{TP}}|a(t)|^2\right]a(t) + \sqrt{\gamma_1}s_{1+}(t). \tag{3.3.5}$$

The physical interpretation of the coefficients is clear from Eq. (3.3.5). The change in resonance frequency due to the change of the real part of the refractive index caused by the Kerr effect is contained in K_{Kerr}. When the real part of the index changes, there will also be an accompanying change of the scattering properties of the cavity. This changes the decay rate by an amount that is related to K_{TP}. If $\chi_{\text{I}}^{(3)}$ is non-zero, the parameter K_{TP} also describes two photon absorption (TPA), and K_{Kerr} will contain a contribution from the change in the real part of the resonance frequency caused by a perturbation of the imaginary part of the dielectric function.

3.3.1 Comparison with FDTD Simulations

To test the validity of the perturbation theory results, one may either compare with experimental data or numerical results from a more accurate method. Where possible, the latter is preferable because there are no measurement uncertainties, which will make the comparison less conclusive. In the case of the Kerr effect, there is a finite difference time domain (FDTD) tool freely available [48], which includes this nonlinearity. In FDTD simulations, Maxwell's equations are solved including the third order susceptibility by discretizing the differential operators in space and time. Therefore, all perturbation orders are naturally included in the solution. The linear parameters (resonance frequency and coupling rates) may be determined from a separate FDTD simulation and used in Eq. (3.3.5). The procedures used to extract these parameters as well as the mode functions $\tilde{\mathbf{f}}_n$ are treated in Appendix B.

For simplicity, we shall consider a system with a single cavity resonance and two ports with an input signal entering the cavity from port 1 and an output signal exiting through port 2. In this case, we denote the input (output) field

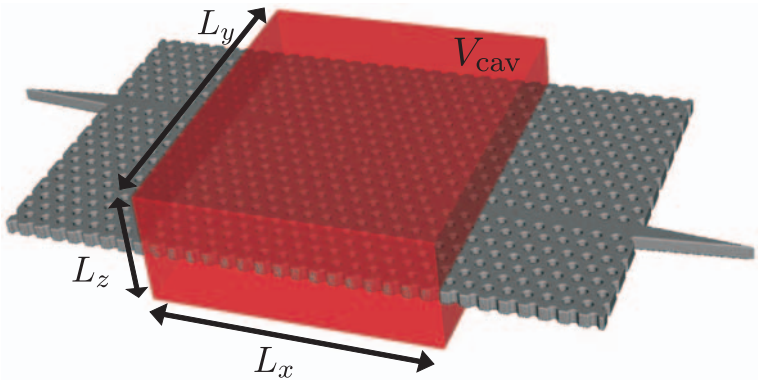

Figure 3.1: The red box shows the cavity volume V_{cav} surrounding the PC membrane. The mode adapters at the end-facets of the waveguides are used in fabricated devices to decrease the coupling loss into the waveguide [49].

by $s_{\text{S}}^{\text{i}} = s_{1+}$ ($s_{\text{S}}^{\text{o}} = s_{2-}$). We generally use the subscripts S, P, and C to denote

the signal, pump, and cavity, respectively. The structure has two mirror-planes at $x=0$ and $z=0$. In the FDTD simulation, a volume V_{cav} must be chosen, and the field energy inside as well as the power flux through its surfaces must be calculated as a function of time. These quantities are to be compared with $|a_{\text{S}}(t)|^2$, $P_{\text{S}}^{\text{i}}=|s_{\text{S}}^{\text{i}}(t)|^2$, and $P_{\text{S}}^{\text{o}}=|s_{\text{S}}^{\text{o}}(t)|^2$ from the TCMT. The incoming and outgoing power must be measured on the boundary of the volume so that Poynting's theorem [41] is satisfied. In Fig. 3.1 the choice of cavity volume is illustrated. The PC structure considered is an H0 cavity [17], which will be investigated in more detail in Chapter 4. The shape of the volume is, in principle, arbitrary, but in the FDTD simulations, it is convenient to work with rectangular shapes. The size of the volume $V_{\text{cav}}=L_xL_yL_z$ is, however, not arbitrary. To understand this, we consider some implications of the TCMT equations.

As discussed in Appendix B.2, the cavity mode may be excited by a transient source. After the source has died out, we have from Eqs. (2.2.21) and (2.2.23) as well as Poynting's theorem [41]

$$\frac{d|a_{\text{S}}(t)|^2}{dt}=-2\gamma_{\text{C}}|a_{\text{S}}(t)|^2=-\sum P_{\text{out}}(t)=-2P_x(t)-2P_z(t) \tag{3.3.6}$$

$$|s_{2-}(t)|^2=|s_{1-}(t)|^2=P_x(t)=\gamma_1|a_{\text{S}}(t)|^2. \tag{3.3.7}$$

In Eqs. (3.3.6) and (3.3.7) it is assumed that the volume is chosen to be symmetrically placed around the cavity in the x and z directions due to the structural symmetry, and L_y is assumed large enough for the power flux through the xz-surfaces of the volume to be negligible. The Cartesian subscripts indicate the direction of the normal vector of the surfaces, where the power passes through. In Fig. 3.2 a top view of the structure from Fig. 3.1 is shown with the electric field distribution overlaid, and it is observed that $P_y\approx 0$ is a good approximation. Rearranging Eqs. (3.3.6) and (3.3.7), we have

$$\frac{P_z}{|a_{\text{S}}|^2}=\gamma_{\text{C}}-\gamma_1 \quad \text{and} \quad \frac{P_x}{|a_{\text{S}}|^2}=\gamma_1. \tag{3.3.8}$$

Since the coupling rates γ_{C} and γ_1 must be independent of the choice of volume, Eq. (3.3.8) puts restrictions on the size of the xy-surfaces relative to the yz-surfaces. Hence, there must exist a curve in the xz-plane defining the corners of the box constituting V_{cav}, such that Eq. (3.3.8) is fulfilled for any L_x and L_z corresponding to the curve. In general, the shape of the curve depends on the radiation pattern of the cavity, but we shall approximate it with a straight line. In Figs. 3.3 and 3.4 we show side views of the structure along with the x and z component of the Poynting vector, $\mathcal{S}=\mathbf{E}\times\mathbf{H}$, integrated over the y-direction. It is seen how the power carried by the waveguides is confined to the membrane in Fig. 3.3, and the power radiated out of the cavity in the z-direction is observed to be strongest close to the cavity from Fig. 3.4. The dashed lines indicate the curves that best satisfy Eq. (3.3.8). We note, that the ratios in the equation were evaluated in the range $x\in[10a;\ 15a]$, and the slope

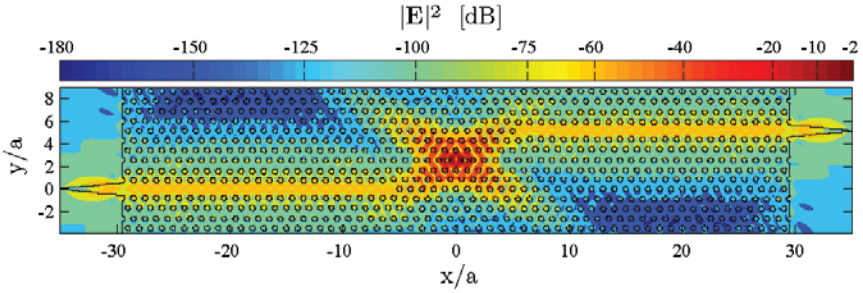

Figure 3.2: Top view of a structure comprised by a H0 cavity coupled to two waveguides. The eigenmode found by the procedure described in Appendix B.1 is overlaid on the structure and it has been normalized to have a maximum of 1.

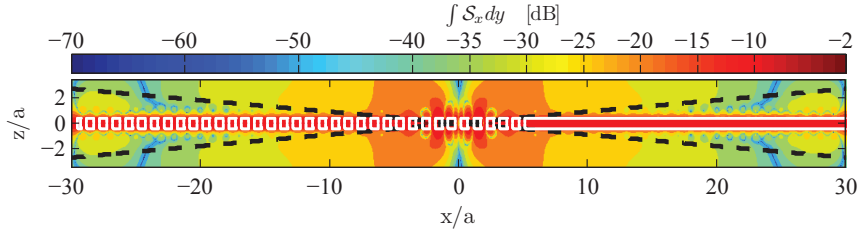

Figure 3.3: Integral of the x-component of the Poynting vector over y as a function of x and z. A normalization is used, so the maximum equals 1. The dashed lines indicate the cone separating light coupling to radiation modes from that being guided by the waveguides. A cross section of the membrane in Fig. 3.2 at $y=6\sqrt{3}a/2$ is shown in white.

of the dashed lines were found from these ratios. By calculating the ratios at smaller distances to the cavity center, the values show considerable fluctuation, so one should probably be careful with extrapolating the dashed lines all the way to the cavity center. It is noted that since the total decay rate γ_C may be determined from monitoring the decay of either P_z or P_x as a function of time as discussed in Appendix B.2, and the ratio P_z/P_x is known, the coupling to the waveguides may be calculated from Eq. (3.3.8) as

$$\gamma_1 = \frac{\gamma_C}{1 + P_z/P_x}. \tag{3.3.9}$$

To determine the exact location of the corners of the volume on the dashed lines in Figs. 3.3 and 3.4, we may consider a continuous wave (CW) excitation of the system. In the linear regime, the following relations hold from Eqs.

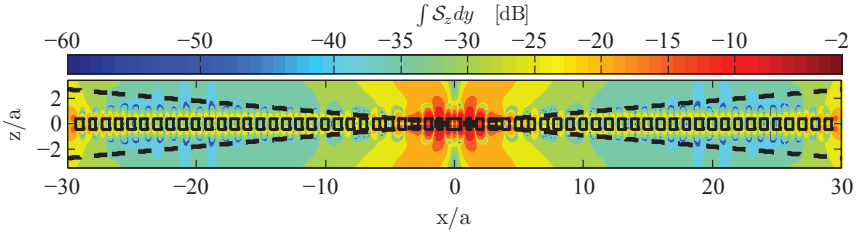

Figure 3.4: Integral of the z-component of the Poynting vector over y as a function of x and z. A normalization is used, so the maximum equals 1. The dashed lines indicate the cone separating light coupling to radiation modes from that being guided by the waveguides. A cross section of the membrane in Fig. 3.2 at $y=0$ is shown in black.

(2.2.21)-(2.2.23) as well as Poynitng's theorem

$$|s_{1-}|^2 = \left| \frac{i\delta_{\mathrm{L}} - \gamma_{\mathrm{C}}}{\sqrt{\gamma_1}} r' \mp \sqrt{\gamma_1} \right|^2 |a|^2 \tag{3.3.10a}$$

$$|s_{2-}|^2 = \left| \frac{i\delta_{\mathrm{L}} - \gamma_{\mathrm{C}}}{\sqrt{\gamma_1}} t' \pm \sqrt{\gamma_1} \right|^2 |a|^2 \tag{3.3.10b}$$

$$|s_{1+}|^2 = |s_{1-}|^2 + |s_{2-}|^2 + 2P_z. \tag{3.3.10c}$$

In steady state, the power passing through the yz-surfaces of the volume is independent of the size of the surface. This is because the CW field is guided in a lossless waveguide. The cavity energy $|a|^2$, however, does depend on the size of the volume. Thus, a specific choice of V_{cav} is required to satisfy Eq. (3.3.10).

Since we are concerned with a comparison between FDTD and TCMT results in the nonlinear regime, we shall determine the cavity volume by considering a steady state excitation including the nonlinearity. From Eqs. (3.3.3) and (2.2.10) it is evident that the size of V_χ, and thus, the size of K_{Kerr} and K_{TP}, depend on the size of V_{cav}. This may not cause any immediate problems, as the product $K_{\mathrm{Kerr}}|a|^2$ could be independent of V_{cav}, since the cavity energy also depends on the volume. Let us investigate the relationship between the input and output power with a CW incident field $|s_{1+}|^2 = P_{\mathrm{in}}$. From Eqs. (2.2.19), (2.2.23), and (3.3.5) it is seen to be given by

$$P_{\mathrm{out}} = \frac{\gamma_1^2}{\left(\delta_{\mathrm{L}} - K_{\mathrm{Kerr}} \frac{P_{\mathrm{out}}}{\gamma_1}\right)^2 + \left(\gamma_{\mathrm{C}} + K_{\mathrm{TP}} \frac{P_{\mathrm{out}}}{\gamma_1}\right)^2} P_{\mathrm{in}}, \tag{3.3.11}$$

where we have considered the case $t_1' = 0$ for simplicity and $P_{\mathrm{out}} = |s_{2-}|^2$. Assuming the power in the waveguide is small enough to neglect nonlinear absorption, the power passing through the yz-surfaces of the cavity volume

in Fig. 3.1 is independent of L_x as in the linear regime. This means that there must be a unique choice of V_χ, such that Eq. (3.3.11) agrees with the input and output power found from an FDTD simulation. In Fig. 3.5(a) the cavity energy calculated from Eq. (2.2.9) is plotted as a function of L_x with L_z given by the dashed lines in Figs. 3.3 and 3.4. In Fig. 3.5(b) we plot the output power as a function of input power found from FDTD (black markers) as well as the solution of Eq. (3.3.11) using a value of $\langle U \rangle$, which provides the best agreement with the FDTD results. The coefficients K_{Kerr} and K_{TP} are calculated from Eq. (3.3.4) using the normalization of the eigenmodes $\tilde{\mathbf{f}}_n$ in Eq. (2.2.10) corresponding to the same volumes used to calculate the energy in Fig. 3.5(a). The optimum choice of cavity volume is indicated by the red circle in Fig. 3.5(a). The agreement in Fig. 3.5(b) is good, which provides

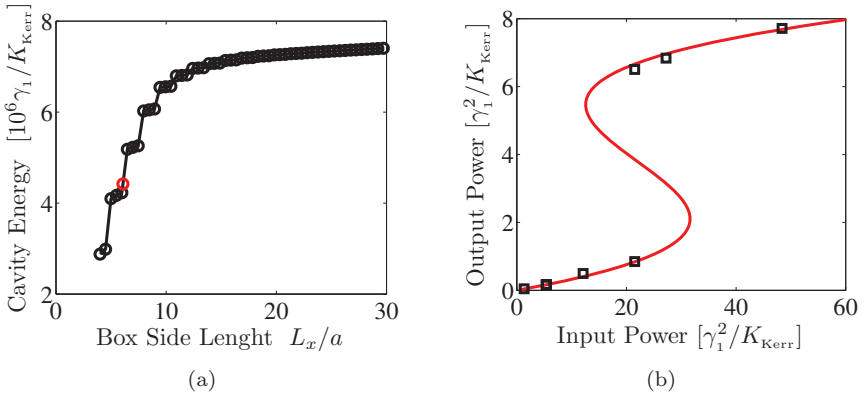

Figure 3.5: P_{out} as a function of P_{in} in steady state for the structure shown in Fig. 3.1. The blue markers are from FDTD simulations, while the red curves are solutions to Eq. (3.3.11). (b) 3D example with a detuning of $\delta_{\text{L}} = 2.1 \times \sqrt{3}\gamma_{\text{C}}$.

confidence in the ability of the TCMT to account for the nonlinear dynamics caused by the Kerr effect. However, the optimum choice of cavity volume corresponds to a rather small value of L_x, and from the discussion of the dashed lines in Figs. 3.3 and 3.4, it is noted that Eq. (3.3.8) may not yield the same power to energy ratios as for larger values of L_x. In this discussion it should be kept in mind that two different FDTD implementations were used to calculate the parameters in Eq. (3.3.11) (PHAZOR) and the curve in Fig. 3.5(b) (MEEP), see Appendix B. For this reason, it is expected that slight differences may occur.

We note that the procedure to obtain the coefficients K_{Kerr} and K_{TP} is completely unambiguous. Unfortunately, an FDTD simulation with a CW excitation in the linear regime is not available at the time of writing the thesis, but we note that such simulations would provide an additional an independent

way of determining the cavity volume. A unique volume should exist, such that both Eqs. (3.3.10) and (3.3.11) are satisfied simultaneously. One objection to the method outlined here, where a combination of steady state and transient excitation of the cavity mode is used, is that the appropriate boundary conditions for Eq. (2.2.6) are different in the two cases. In steady state, Eq. (2.2.7) does not represent the proper boundary condition. However, the changes of the mode close to the cavity region, where V_{cav} is found, are expected to be negligible, so this issue should not have a significant influence on the method described above.

The input-output relation characterized by the curve in Fig. 3.5(b) exhibits a bistable behavior, in which two stable and one unstable output exist for a certain range of input power. Let us find the condition for the appearance of the bistability. For simplicity, we neglect the imaginary part of the perturbation K_{TP}, which is much smaller than the real part for the structure under consideration. If we consider P_{in} to be a function of P_{out}, then Eq. (3.3.11) describes a third order polynomial $y = ax^3 + bx^2 + cx$, where

$$a = \frac{K_{\text{Kerr}}^2}{\gamma_1^4}, \quad b = -2\frac{K_{\text{Kerr}}\delta_{\text{L}}}{\gamma_1^3}, \quad c = \frac{\delta_{\text{L}}^2 + \gamma_{\text{C}}^2}{\gamma_1^2}.$$

In order for a bistability to occur, there must be a real solution to the equation $dy/dx = 0$, which yields the condition

$$\delta_{\text{L}} > \sqrt{3}\gamma_{\text{C}}. \tag{3.3.12}$$

The bistability curve will be encountered again in Chapter 7, where we consider the dynamics of pulses in a waveguide-cavity system with a Kerr nonlinearity.

3.4 Carrier Effects

As discussed in Section 1.4, carrier based nonlinearities are advantageous if switching energy is a key performance parameter. In this section we shall discuss how to include such nonlinearities into the TCMT model. In general, the refractive index of a semiconductor material changes when valence electrons are excited into the conduction band [35]. Due to causality expressed through the Kramers-Kronig relations [41], a change in the real part of the refractive index is always accompanied by a change in the imaginary part and vice versa.

3.4.1 Linear Absorption

First, let us consider the case of linear absorption. The solution of the wave equation in an isotropic medium is a plane wave

$$\vec{\mathcal{E}}(\mathbf{r}, t) = \vec{\mathcal{E}}_0 e^{i\mathbf{k}\cdot\mathbf{r} - i\omega t} + c.c., \tag{3.4.1}$$

where *c.c.* means complex conjugate. Substituting Eq. (3.4.1) into Eq. (2.2.6), we get

$$\mathbf{k}\cdot\mathbf{E}_0 = 0 \quad \text{and} \quad \mathbf{k}\cdot\mathbf{k} = \frac{\omega^2}{c^2}\epsilon_{\mathrm{r}}.$$

The free space wave vector $\mathbf{k}_0$ and complex refractive index $\tilde{n} = n_{\mathrm{R}} + in_{\mathrm{I}}$ are usually defined by the relation $\mathbf{k} = \mathbf{k}_0\tilde{n}$, such that $k_0^2 = \omega^2/c^2$ and $\tilde{n}^2 = \epsilon_{\mathrm{r}}$. Then, the refractive index and dielectric function are related by

$$\begin{array}{rclcrcl} \epsilon_{\mathrm{R}} & = & n_{\mathrm{R}}^2 - n_{\mathrm{I}}^2 & & \epsilon_{\mathrm{I}} & = & 2n_{\mathrm{R}}n_{\mathrm{I}} \\ n_{\mathrm{R}}^2 & = & \frac{\epsilon_{\mathrm{R}}}{2} + \frac{1}{2}\sqrt{\epsilon_{\mathrm{R}}^2 + \epsilon_{\mathrm{I}}^2} & & n_{\mathrm{I}} & = & \frac{\epsilon_{\mathrm{I}}}{2n_{\mathrm{R}}} \end{array}.$$

If we consider a plane wave propagating in the x-direction ($\mathbf{k} = k\hat{\mathbf{x}}$) in an isotropic medium, it follows that the intensity decays as

$$\frac{d|\mathbf{E}(x)|^2}{dx} = -2k_0 n_{\mathrm{I}}|\mathbf{E}(x)|^2.$$

The proportionality constant is denoted the absorption coefficient and is seen to be related to the imaginary part of the complex dielectric function and the conductivity by

$$\alpha_{\mathrm{LA}} = \frac{2\omega n_{\mathrm{I}}}{c} = \frac{\omega\epsilon_{\mathrm{I}}}{n_{\mathrm{R}}c} = \frac{\sigma}{n_{\mathrm{R}}c\epsilon_0}.$$

For our purpose, we need to relate the absorption coefficient to a rate, which is appropriate for the TCMT equations. Using the approximation

$$\frac{d}{dx} \approx \frac{n_{\mathrm{R}}}{c}\frac{d}{dt},$$

we get the absorption rate

$$\gamma_{\mathrm{LA}} = \frac{1}{2}\alpha_{\mathrm{LA}}\frac{c}{n_{\mathrm{R}}}.$$

The factor of $1/2$ in the expression is present because γ_{LA} is defined as the decay rate of the field instead of the intensity.

3.4.2 Two Photon Absorption

Higher order absorption effects are described by an expansion

$$\frac{dI(x)}{dx} = -\alpha_{\mathrm{LA}}I(x) - \alpha_{\mathrm{TPA}}I^2(x),$$

where $I \propto |\mathbf{E}|^2$ is the intensity of the plane wave in Eq. (3.4.1). We shall relate α_{TPA} to the imaginary part of $\chi^{(3)}$, because then the analysis in Section 3.3 provides the corresponding perturbative changes of the eigenfrequency. For

small x or a slowly varying field intensity, an approximate solution to the above equation is

$$I(x) \approx I(0) \exp\left[-(\alpha_{\mathrm{LA}} + \alpha_{\mathrm{TPA}} I)x\right].$$

If nonlinear absorption is modeled by including a first order intensity term in the refractive index, we get

$$\tilde{n} = n_{\mathrm{R}} + i n_{\mathrm{I}} + n_{\mathrm{R}}^{(3)} I + i n_{\mathrm{I}}^{(3)} I,$$

where the real part of the third order refractive index is the commonly used nonlinear refractive index $n_{\mathrm{R}}^{(3)} = n_2$ [34]. It follows as in the case of linear absorption that

$$\alpha_{\mathrm{TPA}} = \frac{2\omega n_{\mathrm{I}}^{(3)}}{c}.$$

From Ref. [34] the following relation holds

$$\tilde{n}^{(3)} = \frac{3}{4} \frac{1}{\epsilon_0 \epsilon_{\mathrm{R}} c} \tilde{\chi}^{(3)} \quad \Leftrightarrow \quad \tilde{\chi}^{(3)} = \frac{4}{3} c \epsilon_0 \epsilon_{\mathrm{R}} \tilde{n}^{(3)}. \tag{3.4.2}$$

Rearranging Eq. (3.4.2) it follows that

$$\alpha_{\mathrm{TPA}} = \frac{2\omega}{c} \frac{3}{4} \frac{1}{\epsilon_0 \epsilon_{\mathrm{R}} c} \chi_{\mathrm{I}}^{(3)} \;\Leftrightarrow\; \chi_{\mathrm{I}}^{(3)} = \frac{2}{3} \frac{c^2 \epsilon_0 \epsilon_{\mathrm{R}}}{\omega} \alpha_{\mathrm{TPA}} \text{ and } \chi_{\mathrm{R}}^{(3)} = \frac{4}{3} c \epsilon_0 \epsilon_{\mathrm{R}} n_2. \tag{3.4.3}$$

These relations are useful since α_{TPA} and n_2 are usually the parameter values extracted from measurements, whereas $\chi_{\mathrm{R}}^{(3)}$ and $\chi_{\mathrm{I}}^{(3)}$ are used in Section 3.3.

3.4.3 Diffusion Effects

In order to describe nonlinearities that originate from carrier density changes, we need to couple Eq. (2.2.21) to equations governing the time variation of the carrier density. Again, we are interested in finding the first order perturbation correction to the resonance frequency of the cavity. Let us first recall Eq. (A.1.4), which relates changes in the dielectric function to changes in the resonance frequency

$$\omega^{(1)}(t) = -\frac{\omega^{(0)}}{2} \frac{\int_V \left[\Delta\epsilon_{\mathrm{R}}(\mathbf{r}, t) + i\Delta\epsilon_{\mathrm{I}}(\mathbf{r}, t)\right] \tilde{\mathbf{f}}_n(\mathbf{r}) \cdot \tilde{\mathbf{f}}_n(\mathbf{r}) dV}{\langle\langle \tilde{\mathbf{f}}_n | \tilde{\mathbf{f}}_n \rangle\rangle}.$$

Our approach will be to relate the change in carrier density to a change in the dielectric function ϵ_{r} by a first order Taylor expansion

$$\Delta\epsilon_{\mathrm{R}} = \frac{\partial \epsilon_{\mathrm{R}}}{\partial \mathcal{N}} \Delta\mathcal{N}, \quad \Delta\epsilon_{\mathrm{I}} = \frac{\partial \epsilon_{\mathrm{I}}}{\partial \mathcal{N}} \Delta\mathcal{N}, \quad \text{where} \quad \Delta\mathcal{N} = \mathcal{N} - \mathcal{N}_0, \tag{3.4.4}$$

and $\mathcal{N}_0$ is the unperturbed carrier density. We assume that electrons and holes have the same properties, which allows us to work with a single carrier species denoted $\mathcal{N}(\mathbf{r},t)$. The spatial and temporal dependence of the carrier density is found by solving the diffusion equation [12]

$$\frac{\partial \mathcal{N}(\mathbf{r},t)}{\partial t} = \nabla^2 \mathcal{N}(\mathbf{r},t) + G(\mathbf{r},t),$$

where $G(\mathbf{r},t)$ represents sources and drains that generate and remove carriers. In order to avoid having to couple a partial differential equation (PDE) to the TCMT equations, we shall make some simplifying assumptions, which are based on experimental and numerical observations [24, 50]. The relaxation of carriers have been observed to take place at two different time scales: An initial fast change of the distribution, which depends on the size of the cavity and is caused by diffusion, followed by a slower stage dominated by non-radiative recombination. In a simple approach to describe this complicated process, we introduce two ambipolar carrier density amplitudes $N_1(t)$ and $N_2(t)$ for the initial and slow stage carrier distributions. The exchange of carriers between the distributions is proportional to the density difference $\Delta N = N_1 - N_2$, which is our time-domain description of the particle current being proportional to the density gradient [12] in the spatial-domain. A further simplification is made by assuming that only the initial distribution interacts with the field. The physical picture is that carriers are generated by the optical field into a distribution having a large overlap with the field. This causes a large density gradient, which causes the carriers to diffuse away from the high field region and form a secondary distribution, from where they only decay through non-radiative recombination. To find the eigenfrequency correction, it is only necessary to consider $\mathcal{N}_1(\mathbf{r},t) = N_1(t) f_{N_1}(\mathbf{r})$, which is given in product form due to the assumptions mentioned above. The distribution function is chosen as

$$f_{N_1}(\mathbf{r}) = \frac{V_1 f_\epsilon(\mathbf{r}) |\tilde{\mathbf{f}}_n(\mathbf{r})|^{2p}}{\int_{V_1} f_\epsilon(\mathbf{r}) |\tilde{\mathbf{f}}_n(\mathbf{r})|^{2p} \, dV}.$$

The function f_ϵ was defined in Section 3.3 and the integer p in the exponent equals 1 for linear absorption and 2 for TPA. We note that $f_{N_1} = 0$ outside the volume V_1. The carrier distribution is proportional to $|\tilde{\mathbf{f}}_n|^{2p}$ since it is assumed to follow the optical field distribution. The total number of carriers is found by integrating $\mathcal{N}_1$ over all space and it equals $V_1 N_1$, which is seen to be the case, since

$$V_1 = \int_V f_{N_1}(\mathbf{r}) dV.$$

As mentioned above, the rate of change of the density N_1 due to diffusion is propotional to the density difference between the two distributions

$$\left.\frac{dN_1(t)}{dt}\right|_{\text{diff}} = -\frac{1}{\tau_{\text{diff}}} \left[N_1(t) - N_2(t)\right].$$

The corresponding term for N_2 can be found from the conservation of charge through the balancing equation

$$V_1 \frac{dN_1(t)}{dt}\bigg|_{\text{diff}} = -\,V_2 \frac{dN_2(t)}{dt}\bigg|_{\text{diff}} \quad \Rightarrow \quad \frac{dN_2(t)}{dt}\bigg|_{\text{diff}} = \frac{1}{\tau_{\text{diff}}}\left[N_1(t) - N_2(t)\right]\frac{V_1}{V_2}.$$

By introducing terms to represent non-radiative recombination of the carriers, the rate equations become

$$\frac{dN_1(t)}{dt} = -\frac{1}{\tau_{\text{diff}}}\left[N_1(t) - N_2(t)\right] - \frac{1}{\tau_{\text{nr}}}N_1(t) + \text{source terms} \tag{3.4.5}$$

$$\frac{dN_2(t)}{dt} = \frac{1}{\tau_{\text{diff}}}\left[N_1(t) - N_2(t)\right]\frac{V_1}{V_2} - \frac{1}{\tau_{\text{nr}}}N_2(t). \tag{3.4.6}$$

From Eqs. (3.4.5) and (3.4.6) it is seen that the details of the secondary distribution are included in the ratio V_1/V_2, which is a measure of how fast the secondary distribution saturates such that diffusion no longer plays a significant role in the carrier relaxation process. Recombination is assumed to take place in both carrier distributions, and to keep things simple, we assume the same non-radiative lifetime in both distributions.

From Eqs. (A.1.4) and (3.4.4), the perturbative change of the eigenfrequency originating from changes in the carrier distribution is

$$\omega^{(1)}(t) = -\omega^{(0)}\left[\frac{\partial \epsilon_{\text{R}}}{\partial \mathcal{N}_1} + i\frac{\partial \epsilon_{\text{I}}}{\partial \mathcal{N}_1}\right] N_1(t)\frac{\int_V f_{N_1}(\mathbf{r})\tilde{\mathbf{f}}_n(\mathbf{r})\cdot\tilde{\mathbf{f}}_n(\mathbf{r})dV}{2\langle\langle\tilde{\mathbf{f}}_n|\tilde{\mathbf{f}}_n\rangle\rangle}.$$

Let us write the frequency shift as

$$\omega^{(1)}(t) = \left[K_{\text{FCD}} - iK_{\text{FCA}}\right]N_1(t),$$

where the coefficients are given by

$$K_{\text{FCD}} = -\text{Re}\left\{\omega^{(0)}\zeta_{N_1}\right\}\frac{\partial \epsilon_{\text{R}}}{\partial \mathcal{N}} \qquad \text{and} \qquad K_{\text{FCA}} = \text{Im}\left\{\omega^{(0)}\zeta_{N_1}\right\}\frac{\partial \epsilon_{\text{I}}}{\partial \mathcal{N}}.$$

The dimensionless structural parameter ζ_{N_1} is defined as

$$\zeta_{N_1} = \frac{\int_V f_{N_1}(\mathbf{r})\tilde{\mathbf{f}}_n(\mathbf{r})\cdot\tilde{\mathbf{f}}_n(\mathbf{r})dV}{2\langle\langle\tilde{\mathbf{f}}_n|\tilde{\mathbf{f}}_n\rangle\rangle}.$$

The source term in Eq. (3.4.5) originating from linear absorption is found by noting that each absorbed photon creates one electron-hole pair. This gives rise to a balancing equation

$$V_1\frac{dN_1(t)}{dt} = -\frac{dN_{\text{P}}(t)}{dt} = -\frac{1}{\hbar\omega_{\text{C}}}\frac{d|a(t)|^2}{dt}\bigg|_{N_1} = \frac{2\gamma_{\text{LA}}}{\hbar\omega_{\text{C}}}|a(t)|^2 + \frac{2K_{\text{FCA}}N_1(t)}{\hbar\omega_{\text{C}}}|a(t)|^2,$$

where $N_{\rm P}$ is the number of photons in the cavity. To understand the last equality, let us write Eq. (2.2.21) including the first order perturbation due to carriers

$$\left.\frac{da(t)}{dt}\right|_{N_1} = -i\left[\delta_{\rm L} + K_{\rm FCD}N_1(t)\right]a(t) - \left[\gamma_{\rm LA} + \gamma_1 + \gamma_\perp + K_{\rm FCA}N_1(t)\right]a(t) \quad \Rightarrow$$
$$\left.\frac{d|a(t)|^2}{dt}\right|_{N_1} = -2(\gamma_{\rm LA} + \gamma_1 + \gamma_\perp)|a(t)|^2 - 2K_{\rm FCA}N_1(t)|a(t)|^2.$$

In the first equation, we expanded the total decay rate in its constituents $\gamma_{\rm C} = \gamma_1 + \gamma_{\rm loss}$, where $\gamma_{\rm loss}$ has a contribution from out of plane scattering $\gamma_\perp$ as well as linear absorption $\gamma_{\rm LA}$. The equations for the carrier densities including source terms due to linear absorption are then

$$\frac{dN_1(t)}{dt} = -\frac{1}{\tau_{\rm diff}}\left[N_1(t) - N_2(t)\right] - \frac{1}{\tau_{\rm nr}}N_1(t) + \frac{2\gamma_{\rm LA}}{\hbar\omega_{\rm C}V_1}|a(t)|^2 \tag{3.4.7}$$

$$\frac{dN_2(t)}{dt} = \frac{1}{\tau_{\rm diff}}\left[N_1(t) - N_2(t)\right]\frac{V_1}{V_2} - \frac{1}{\tau_{\rm nr}}N_2(t). \tag{3.4.8}$$

It is noted that the free carrier absorption (FCA) term is not included in Eq. (3.4.7), since it does not change the number of excited carriers.

Two photon absorption may be included in a similar manner by a balancing equation expressing conservation of charge. In the case of TPA, it takes two photons to generate an electron-hole pair

$$V_1\left.\frac{dN_1(t)}{dt}\right|_{\rm TPA} = -\frac{1}{2}\left.\frac{dN_{\rm P}(t)}{dt}\right|_{\rm TPA} = -\frac{1}{2\hbar\omega_{\rm C}}\left.\frac{d|a(t)|^2}{dt}\right|_{\rm TPA} = \frac{2K_{\rm TP}|a(t)|^2}{2\hbar\omega_{\rm C}}|a(t)|^2.$$

Adding this term to Eq. (3.4.7), we get

$$\frac{dN_1(t)}{dt} = -\frac{1}{\tau_{\rm diff}}\Delta N(t) - \frac{1}{\tau_{\rm nr}}N_1(t) + \frac{2\gamma_{\rm LA}}{\hbar\omega_{\rm C}V_1}|a(t)|^2 + \frac{K_{\rm TP}|a(t)|^2}{\hbar\omega_{\rm C}V_1}|a(t)|^2. \tag{3.4.9}$$

Finally, the equation for the cavity field including all the nonlinear effects is

$$\frac{da(t)}{dt} = -i\left[\delta_{\rm L} + K_{\rm FCD}N_1(t) - K_{\rm Kerr}|a(t)|^2\right]a(t) - \left[\gamma_{\rm C} + K_{\rm FCA}N_1(t) + K_{\rm TP}|a(t)|^2\right]a(t) + \sqrt{\gamma_1}s_{1+}(t) \tag{3.4.10}$$

With the TCMT equations developed in this chapter, it is possible to compare with experiments, in which the Kerr effect and carrier induced nonlinearities are assumed to be the only mechanisms facilitating the control of the signal by the pump. In Chapter 5 we consider such experiments, but first, a discussion about design of the structures is given in the next chapter.

4

Design of Waveguide-Cavity Structures

4.1 Introduction

Before moving on to a discussion of experimental techniques and comparisons of measurements and simulations based on the previous chapter, we will consider the structures used in these experiments in more detail. The first section of this chapter contains some general considerations related to the design of photonic crystal (PC) waveguide-cavity structures intended for all-optical switching. In the second section we illustrate this discussion with a specific example of a structure with two ports and an H0 cavity.

4.2 General Design Considerations

There are many degrees of freedom related to a PC membrane structure, such as membrane thickness d, lattice constant a, hole radii r_0, and a range of parameters related to the introduction of defects. This makes it a very versatile platform for creating devices, but also complicates the design of such structures. It therefore makes sense to have a procedure for the design, which starts from a minimum number of parameters and gradually adds complexity. In Section 1.3 we introduced the basic building blocks of PC membrane devices, and our design procedure is based on these.

The starting point is the infinite PC membrane, which is fully described by its thickness, lattice constant and hole radius. Since the interesting operation wavelength is 1550nm, the membrane parameters must be chosen so that this wavelength lies well within the band gap seen in Fig. 1.2(b). The next step is to consider the cavity without introducing waveguides into the structure. We may define the out-of-plane quality factor $Q_\perp = \omega_m / 2\gamma_\perp$ to be a measure of the

coupling to radiation modes from the cavity. The quality factor of the structure containing only the cavity is denoted the unloaded quality factor Q_{ul}, whereas the quality factor corresponding to cavity-waveguide coupling is $Q_{||} = \omega_m / 2\gamma_m$, and the loaded or total quality factor is $Q_m = \omega_m / 2(\gamma_m + \gamma_\perp)$. The out-of-plane and unloaded quality factors are not exactly equal due to the changes occurring by introducing waveguides into the structure. However, since the waveguides are well separated from the cavity to achieve a reasonable loaded Q, the difference between Q_{ul} and $Q_\perp$ is expected to be small. As a general rule, the out-of-plane quality factor should be as large as possible to increase the signal transmission in the "on" state of the switch. Thus, the structure containing only the cavity may be used to optimize Q_{ul} and thereby $Q_\perp$, while at the same time ensuring that the resonance frequency is close to 1550nm.

The final step is to design the waveguides such that the resonance frequency of the cavity lies within the frequency range of the guided mode of the waveguide. Generally, there will be multiple guided modes as in Fig. 1.3, but in most cases the even mode is preferred. This is because it is confined more tightly than the odd mode (see Figs. 1.3(b) and 1.3(c)), and hence, scattering loss due to side wall roughness of the holes caused by fabrication imperfections is smaller. Another important issue is the fact that experiments are usually performed by coupling light into the waveguide from a single mode optical fiber. The fiber mode has an even symmetry and will therefore predominantly couple to the even waveguide mode. The coupling rate between the cavity and waveguides should always be reduced as much as possible while maintaining a reasonable "on" state transmission at any given signal bandwidth. This will increase the switching contrast and reduce the switching energy as discussed in Chapters 7 and 8.

It is important to keep fabrication limitations in mind when designing devices. For instance, it is difficult to produce several different hole sizes with good accuracy. Therefore, the designs in this thesis are generally based on a common hole radius.

4.3 Example: Two Port Structure

Let us make use of the general considerations in the previous section and design a waveguide-cavity structure with an H0 cavity [17] coupled to two ports. The hole radii are chosen to be $r_0 = 0.23a$, which is inspired by the values in Refs. [23, 24]. We note that the dielectric constant used in all finite difference time domain (FDTD) simulations throughout the thesis is $\epsilon_{\mathrm{r}} = 10.01$. The cavity is formed by displacing two adjacent holes horizontally as illustrated in Fig. 4.1(a). This cavity design is single mode and from Fig. 4.1(b) the magnetic field H_z is observed to be confined to a very small volume.

As mentioned in Section 4.2, the out-of-plane Q of the cavity is an important performance parameter. It may depend critically on the location of the holes surrounding the cavity, but the problem easily becomes too computationally

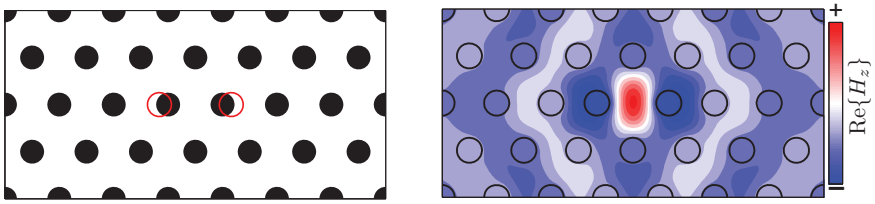

(a) (b)

Figure 4.1: (a) Photonic crystal H0 cavity formed by shifting two adjacent holes horizontally apart by δx, as illustrated with red circles. (b) Magnetic field distribution H_z for the same structure found by FDTD simulations with a cavity shift of $\delta x = 0.16a$, a membrane thickness of $d = 0.8a$ and $r_0 = 0.23a$.

demanding, if we allow too many degrees of freedom in the design. Let us therefore examine the dependence of the resonance frequency and unloaded quality factor on the cavity shift δx. This is shown in Fig. 4.2(a) for a fixed membrane thickness of $d = 0.8a$ and $r_0 = 0.23a$. The resonance frequency is seen to increase when δx is decreased and the space between the shifted holes becomes smaller. It is a general trend that the eigenfrequencies increase when the modes must fit into a smaller region of high index material. In an intuitive picture, this may be understood by considering a conventional Fabry-Perot cavity formed by two parallel mirrors. The resonance condition $\omega n L/c = \pi p$, where L is the mirror distance and p is an integer, shows that decreasing the cavity size increases the resonance frequency. Whether this argument is valid

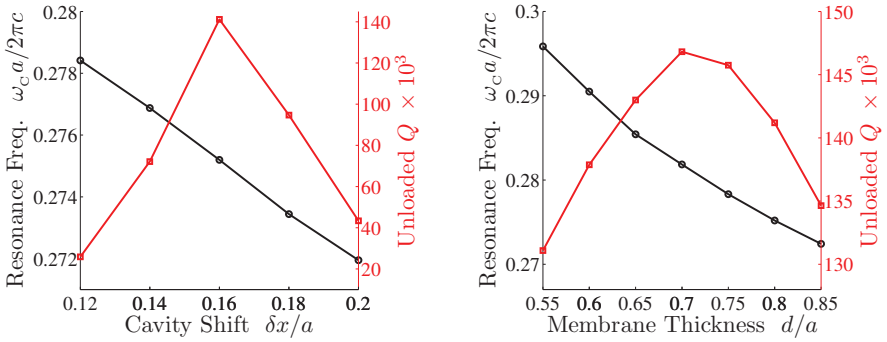

(a) (b)

Figure 4.2: (a) Dependence of the resonance frequency and unloaded Q on the cavity shift δx for an H0 cavity with $r_0 = 0.23a$ and $d = 0.8a$. (b) Dependence of the resonance frequency and unloaded Q on the membrane thickness d for an H0 cavity with $r_0 = 0.23a$ and $\delta x = 0.16a$.

for sub-wavelength cavities like the ones we are considering, however, is not

obvious.

Even though the resonance frequency changes with the cavity shift δx, it is still possible to achieve a physical resonance at $\lambda_C = 1550$nm by adjusting the lattice constant a. This would, however, change the physical membrane thickness since its ratio with a is fixed at $d = 0.8a$. The quality factor is seen to vary considerably as δx is changed and an optimum is found when the cavity shift is $0.16a$. From the discussion in Appendix B.4 it is clear that one should use caution regarding the absolute values of these results.

The dependence of the eigenfrequency and unloaded Q on the membrane thickness d is also investigated, and Fig. 4.2(b) shows the results at a fixed cavity shift of $\delta x = 0.16a$. Again, the resonance frequency increases as the thickness is decreased confirming the trend that a reduction in the available space increases the frequency. Fig. 4.2(b) also shows that the quality factor is not very sensitive to the membrane thickness within the considered range.

When a cavity design is found with a good unloaded quality factor and a resonance at the desired wavelength, the waveguides constituting the ports must be designed. In Refs. [23,24] the frequency range of the guided waveguide mode was adjusted by increasing the radius of the holes adjacent to the line-defect. As discussed in Section 4.2, we shall apply shifts of the holes instead, because such structures are easier to fabricate. The approach is illustrated in Fig. 4.3(a), where the first row of holes adjacent to the line-defect are shifted by l_{1p} perpendicularly towards the waveguide axis. In all our designs, the waveguide axis coincides with the x-axis, except for the cross waveguide structure in Chapter 6. In Fig. 4.3(b) the corresponding band diagrams are shown for different hole shifts. It is observed that the frequencies of both the even and odd mode (see Fig. 1.3) increase as l_{1p} is increased. Since the frequency range of the guided mode may readily be adjusted by tuning l_{1p}, the question arises, where to place the cavity resonance in this range. The slow light region close to the band edge at $k_x = 0.5 \times 2\pi/a$ is not preferable for our purpose, since it enhances scattering loss and nonlinear effects in the waveguide [19].

In Fig. 4.4 we show an example of a complete structure with the magnetic field intensity profile overlaid. From the logarithmic contour scale, it is clearly seen how the field is concentrated in the center of the cavity and leaks into the waveguides. The corresponding transmission spectrum is calculated using FDTD simulations as described in Appendix B.3 and the results are depicted in Fig. 4.5. We show the results from both method 1 and 2, see Appendix B.3. From the first method it is also possible to calculate the transmission of the waveguide alone, and this spectrum corresponds to the black circles in Fig. 4.5. The band edge of the waveguide is clearly observed close to a normalized frequency of $\omega = 0.263 \times 2\pi c/a$. The red curve shows a Lorentzian fit to the transmission found from method 2. The agreement is not particularly good, and this is believed to be caused by reflections from the interfaces between the strip waveguide and the PC waveguide, see Fig. 4.4. In other simulations, e.g. mode 2 in Fig. 8.9, the transmission shows a much better agreement with a

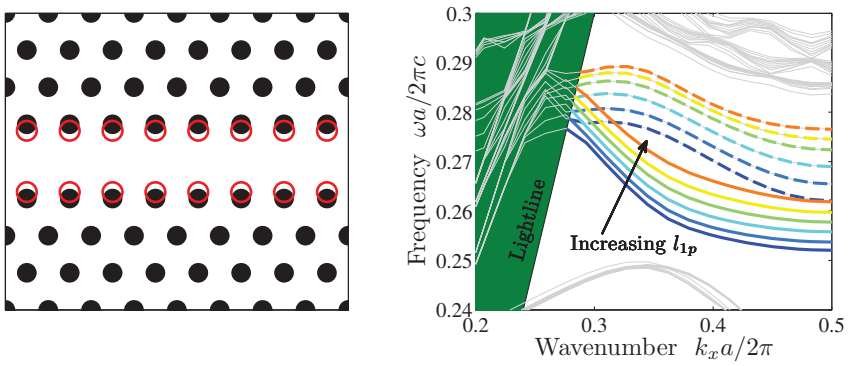

(a) (b)

Figure 4.3: (a) Line-defect waveguide with the first row of holes perpendicularly displaced by l_{1p} towards the waveguide axis. (b) Band diagrams for PC membrane line-defect waveguides with $r_0 = 0.23a$ and a membrane thickness of $d = 0.8a$ with varying l_{1p}. The range of l_{1p} is from -0.1a (blue) to +0.15a (orange) and as in Fig. 1.3(a), solid lines correspond to the even modes, and dashed lines to the odd modes.

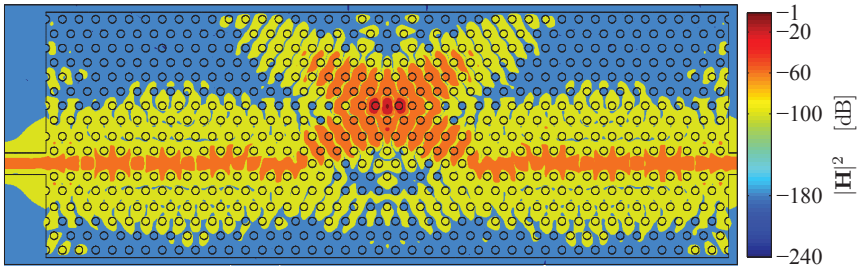

Figure 4.4: Complete structure with an H0 cavity and 2 ports. The magnetic field intensity is shown and normalized to a peak value of 1, and the shown contours match the values on the colorbar. The parameters are: $d = 0.8a$, $r_0 = 0.23a$, $\delta x = 0.2a$, $l_{1p} = 0.1a$, and $l_{2p} = 0.1a$.

Lorentzian. Hence, the result in Fig. 4.5 should not be taken as an indication that the temporal coupled mode theory (TCMT) description of the linear properties of PC waveguide-cavity structures is insufficient.

The inset in Fig. 4.5 shows a close up at the transmission peak, and we emphasize that the peak transmission is very close to 1, indicating a large out-of-plane quality factor, which is consistent with Fig. 4.2. The large peak transmission is observed, since the transmission from method 1 is very close to the waveguide transmission, and the transmission from method 2 is close to 1.

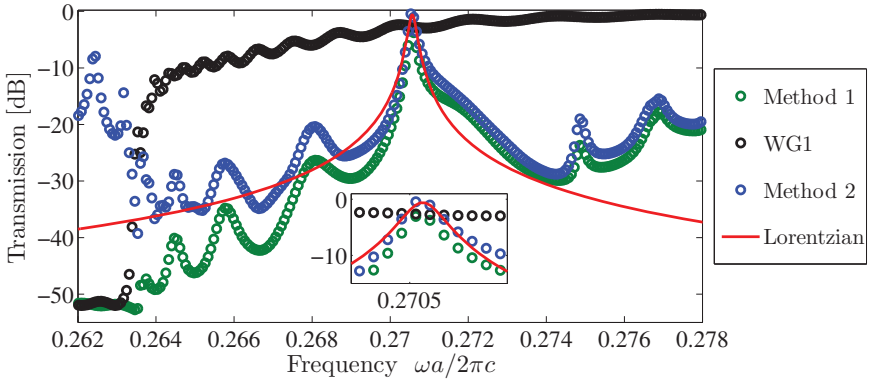

Figure 4.5: Transmission spectrum of the structure in Fig. 4.4 using the two different methods described in Appendix B.3. The black circles are from a calculation with only a waveguide as seen in Fig. B.3 .The inset shows a zoom-in at the transmission peak. The resonance frequency is $0.2705 \times 2\pi c/a$ and the loaded quality factor is 1400.

Having studied the structures containing 2 port and an H0 cavity in more detail in this chapter, we shall now move on to consider experiments performed using these structures in the next chapter.

5

Experiments

5.1 Introduction

This chapter contains a discussion about experimental techniques for investigating the nonlinear dynamics of waveguide-cavity structures as well as measurement results. All the work results from a close collaboration with Alfredo de Rossi and Sylvain Combrié from Thales Research and Technology in Palaiseau, France. During a visit at Thales in the fall of 2011, some of the measurements were carried out, while others were performed solely by Dr. de Rossi at later times as a result of an ongoing discussion. The chapter is divided into four sections, and the first two describe two different ways of measuring the cavity dynamics. The first is denoted the homodyne technique and is the standard method used in the literature [23, 24]. The second method is the heterodyne technique, which is commonly used in the characterization of nonlinear dynamical effects in waveguides [51, 52]. The last two sections are devoted to a comparison with simulations based on the model discussed in Chapter 3, as well as a numerical parameter investigation.

5.2 Homodyne Pump Probe Measurements

As discussed in Section 1.4, the basic functionality of an all-optical switch is to use a strong pump field to change the transmission properties experienced by a weak signal field. In an experiment, the obvious approach would be to couple the signal into the cavity while applying the pump simultaneously and referencing with a measurement obtained without the pump. The question arises, how to measure only the output of the signal without any contribution from the pump. If, for instance, the signal was coupled in through the waveguide and the pump was directed vertically onto the cavity from above the membrane, there would still be some finite coupling of the pump into the waveguide, where it would propagate with the signal to the detector and disturb the measurement.

Another issue with this approach is that it would be difficult to estimate the amount of optical power reaching the cavity from the pump, thereby making a quantitative comparison with models difficult.

Another approach is to couple the pump into the waveguide along with the signal and use some technique to enable a separation of the fields at the detector. Different polarizations is not an option, since only the TE-like polarization is guided by the photonic crystal (PC) waveguide. Spectral filtering would work, but it sets limitations on the frequency separation of the fields making it difficult to investigate all wavelength configurations of the signal and pump. In the homodyne pump probe technique, the signal and pump consist of a sequence of pulses originating from the same laser with a repetition period $1/\Gamma_{\mathrm{rep}}$, which is much larger than the full width at half maximum (FWHM) of the pulses $\Delta t_{\mathrm{S/P}}$. By applying a sinusoidal modulation with a frequency different from the repetition rate and using a Lock-in amplifier [53] after the detector, it is possible to filter out the part of the photo current, which oscillates at the modulation frequency.

5.2.1 Co-Propagating Setup

A schematic illustration of the setup used in the homodyne technique at Thales is shown in Fig. 5.1. The spectrally broad output of a 100fs mode locked fiber laser is split in two and passed through bandpass filters (BPFs) of widths 1.2nm (pump) and 0.72nm (signal). An amplitude modulation is applied to the sig-

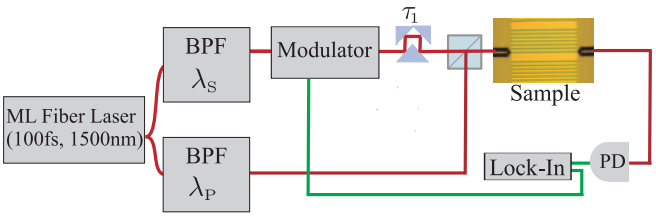

Figure 5.1: Schematic illustration of the setup for homodyne pump probe experiments with the pump and signal co-propagation through the sample. The red lines indicate the paths of optical signals, and the green show electrical signals. The variable delay line introduces a delay τ_1 in arrival time at the cavity between the pump and the signal. ML: Mode locked. BPF: Band pass filter. PD: Photo detector.

nal and it is passed through a variable delay line before being coupled into the sample. An electronic reference signal containing information about the modulation frequency Ω_{mod} is sent to the lock-in amplifier. Fig. 5.1 shows the co-propagating scheme, where the pump is coupled into the sample from the same side as the signal. Coupling the fields into the sample may be done by lensed fibers or free-space coupling. Using fibers makes the rough alignment easier, since an optical microscope may be used to visually keep track of the lo-

cation of the fiber tip relative to the waveguide end-facet. Free-space coupling makes it easy to control the polarization of the in-coupled light, because it may be measured with free-space optical components immediately before the sample. This is also the case for the input power. The polarization usually changes during propagation through a fiber, which complicates the polarization control when using lensed fibers. Stability of the optical output was also observed to be better when using free-space coupling. For these reasons, this was the coupling scheme used in all the experiments.

The mean power measured immediately before entering the sample $\overline{P}^{\mathrm{i}}_{\mathrm{P}}$ is related to the pulse energy arriving at the cavity inside the sample by the relation

$$U^{\mathrm{i}}_{\mathrm{P}} = \frac{\overline{P}^{\mathrm{i}}_{\mathrm{P}}}{\Gamma_{\mathrm{rep}}}\sqrt{T_{\mathrm{coup}}}, \tag{5.2.1}$$

where T_{coup} accounts for the coupling loss at the end-facet of the sample as well as propagation loss in the PC waveguide between the facet and the cavity. An accurate determination of T_{coup} is difficult. In principle, a reference structure containing only the PC waveguide could be used to normalize the output spectrum of the structure containing a cavity. From the peak of the normalized spectrum, the loss due to out-of-plane scattering from the cavity could be found, and the directly measured fiber-to-fiber loss of the reference structure would be $1-T_{\mathrm{coup}}$, provided the cavity is placed halfway between the end-facets or a low propagation loss compared to coupling loss. However, there will always be differences in coupling efficiencies and propagation loss between different structures, so the uncertainty in the value of T_{coup} is significant.

Since the signal and pump wavelengths are set by filtering the broadband femtosecond pulses from the fiber laser using narrow BPFs, the input spectra of the fields should correspond to the transmission spectra of the filters. Fig. 5.2 shows examples of input spectra of the pump (blue) and signal (green) normalized to reflect a typical ratio between their pulse energies of a factor of 20. The figure also shows Lorentzian (solid), Sech^2 (dashed), and Gaussian (dotted) fits to the spectral shapes of the inputs. The slope of the tails in the spectra is seen to lie somewhere between the steep slope of a Gaussian and slow decay of a Lorentzian. Information about chirp originating from the fiber laser is not contained in the spectra and we do not have autocorrelation measurements available to investigate the pulse shape in the time domain. However, since the pulses are spectrally narrow compared to the femtosecond pulses, it is expected that there is only a small amount of chirp. The uncertainty related to the chirp should, however, be kept in mind when comparing experiments with numerical modeling.

By varying the delay in arrival times of the pump and signal τ_1, it is possible to probe the time response of the cavity dynamics. The response consists of both a linear part related to the photon lifetime of the cavity, and a

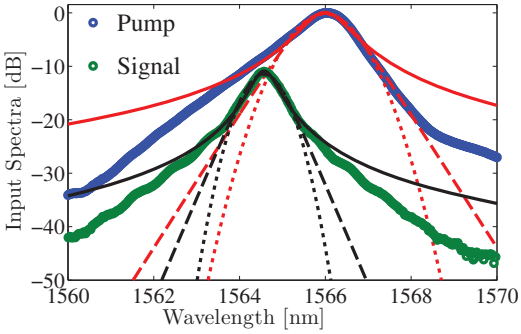

Figure 5.2: Example of input spectra of the pump (blue) and signal (green) normalized so $U_{\mathrm{P}}^{\mathrm{i}} = 20U_{\mathrm{S}}^{\mathrm{i}}$. The solid curves are Lorentzian fits, whereas the dashed and dotted are Sech^2 and Gaussian fits, respectively.

nonlinear part related to dynamical changes in the resonance frequency and absorption. Fig. 5.3 shows an example of the lock-in signal as a function of delay τ_1. The delay is defined such that a negative value indicates the signal arriving before the pump. Large negative delays therefore correspond to linear transmission. The measurement in Fig. 5.3 was performed using the setup

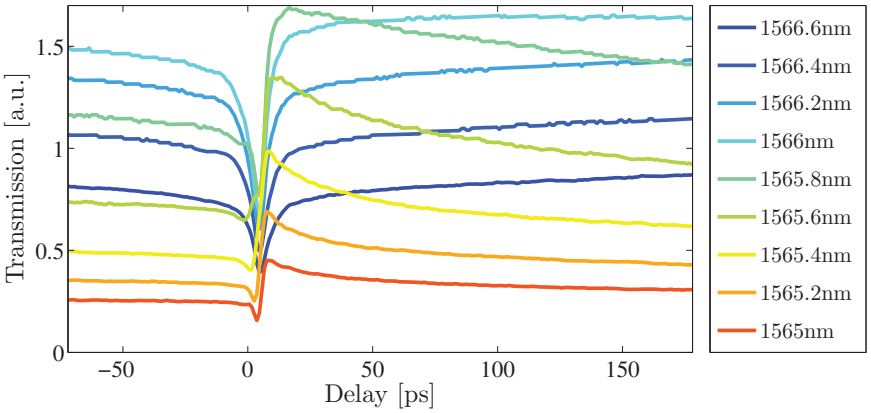

Figure 5.3: Lock-in signal as a function of delay between the pump and signal using the setup shown in Fig. 5.1. The sample is an InP two port device with an H0 cavity having a measured resonance at $\lambda_1 = 1566.0$nm and a total Q of 3200. The pump has a mean power of $\overline{P}_{\mathrm{P}}^{\mathrm{i}} = 23\mu$W and is centered at $\lambda_{\mathrm{P}} = 1566.2$nm. The mean power of the signal is $\overline{P}_{\mathrm{S}}^{\mathrm{i}} = 2\mu$W and the different curves correspond to different signal wavelengths λ_{S}.

in Fig. 5.1, where the signal and pump are co-propagating through the sample. It is difficult to determine the exact location of the origin on the delay axis,

so it is simply defined to be close to the onset of changes in the transmission curves. The signal is assumed to be weak enough not to cause nonlinear effects, but changes still occur at negative delays due to the finite width of the pulses as well as the photon lifetime of the cavity. There will be some small dependence on delay because the alignment is not equally good at all positions of the moving mirror in the variable delay line. This dependence was measured at $\lambda_S = \lambda_1$ with the pump turned off, and the curves in Fig. 5.3 have been normalized by the resulting curve to remove this artifact.

At positive detunings ($\lambda_S > \lambda_1$) the transmission is observed to decrease, which is consistent with a blue-shift of the resonance caused by free carrier dispersion (FCD) and/or nonlinear absorption. Fig. 5.3 shows that the transmission increases when the signal and pump arrive at the cavity simultaneously at negative detunings, $\lambda_S < \lambda_1$. Again, this is consistent with a blue-shift of the resonance. A small dip in the transmission is also observed at very short delays , which could be caused by a red-shift from the Kerr effect or two photon absorption (TPA). It is noted from Fig. 5.3 that the maximum transmission is larger in the nonlinear regime than in the linear at large negative delays. This is illustrated in Fig. 5.4, which plots the linear transmission $T_U(-70\text{ps})$ (blue) as well as the maximum transmission (red) as a function of wavelength. The blue curve is a measurement of the energy transmission

$$T_U(\delta_S, \Omega_S) = \frac{\int T_{CW}(\omega) P_S^i(\omega, \Omega_S) d\omega}{\int P_S^i(\omega, \Omega_S) d\omega}, \tag{5.2.2}$$

where $P_S^i(\omega)$ is the input spectrum of the signal seen in Fig. 5.2 and Ω_S is the FWHM of the input in the frequency-domain. Under the assumption that the nonlinear effect caused by the pump pulse only causes a resonance shift and nonlinear absorption, there is an upper limit on the nonlinear transmission set by the linear transmission on resonance $\lambda_S = \lambda_1$. The resonance changes

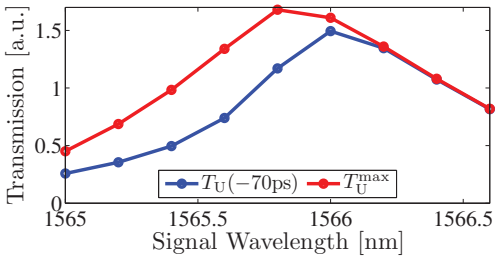

Figure 5.4: Lock-in signal at large negative delays (blue) and peak transmission (red) from Fig. 5.3. The blue curve corresponds to the linear transmission in Eq. (5.2.2).

dynamically during the passage of the signal and the effective detuning cannot equal zero at all times, which results in a lower transmission in the nonlinear

case. The observed behavior in Figs. 5.3 and 5.4 is incompatible with this assumption, since the nonlinear transmission is seen to exceed the peak of the linear transmission in Fig. 5.4. The pump can transfer energy to the signal via coherent nonlinear interactions in either the cavity or during propagation through the waveguide [51]. Energy transfer occurring in the cavity should only be significant within a time interval given by the photon lifetime, where the fields are in the cavity simultaneously. In the waveguide, energy transfer should only occur around zero delay in a time interval given by the width of the pulses. The larger nonlinear transmission is observed even at large delays, which makes energy transfer an implausible explanation. This experiment thus shows some artifacts, which are not readily explainable. We have seen indications of a contribution from coherent energy transfer from the pump to the probe, but no conclusive evidence. Historically, such effects have sometimes been termed "artifacts" in the literature on heterodyne pump probe measurements [51], because they were undesired in the measurement. For optical switches, these contribution could contribute to increase the switching contrast. In any case, it is important to be aware of such effects when interpreting the experimental data.

5.2.2 Counter-Propagating Setup

Even though it is not immediately clear whether the unexpected behavior observed in the co-propagating setup is related to interactions taking place in the waveguide, it is a natural next step to try a counter-propagating scheme, where the signal and pump are coupled into the waveguides at opposite ends of the sample. Fig. 5.5 illustrates this scheme. The nonlinear interaction between the

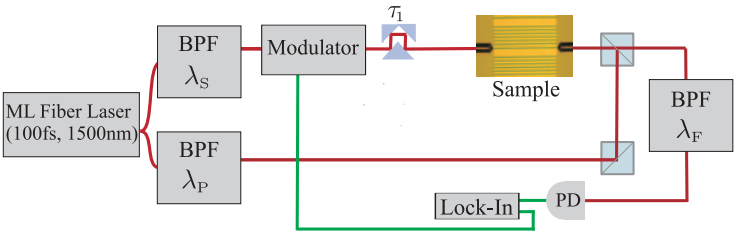

Figure 5.5: Schematic illustration of the setup for homodyne pump probe experiments with the pump and signal counter-propagation through the sample. This setup also contains a band pass filter before the detector with a center wavelength λ_F and bandwidth $\Delta\lambda_F$.

pulses as they pass each other in the waveguide should be negligible compared to the interaction in the cavity due to the field enhancement of the cavity. The setup in Fig. 5.5 also contains a BPF before the detector, which only transmits wavelengths around its center wavelength λ_F within a bandwidth of $\Delta\lambda_F$.

In Fig. 5.6(a) we show the transmission of the signal as a function of delay for a detuning of $\lambda_S - \lambda_1 = 3.5$nm at different pump power levels. The curves

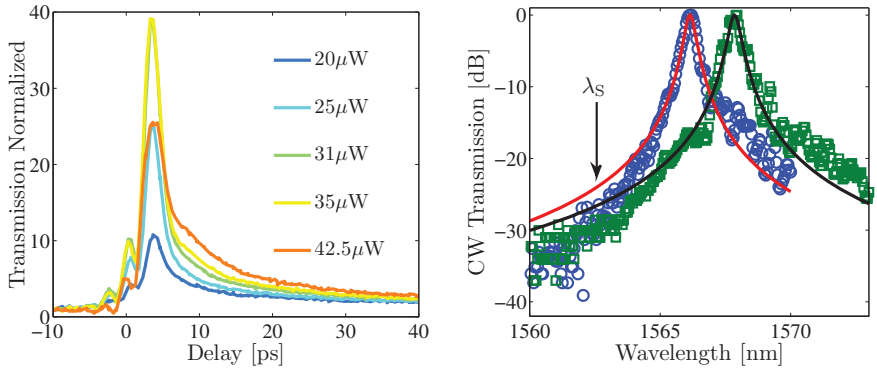

Figure 5.6: (a) Normalized signal transmission as a function of delay τ_1 for the same sample as in Fig. 5.3 using the setup in Fig. 5.5. The signal average power is $\overline{P}_{\mathrm{S}}^{\mathrm{i}} = 3.3\mu\mathrm{W}$ and it is centered at $\lambda_{\mathrm{P}} = 1562.5\mathrm{nm}$. The wavelength of the pump is $\lambda_{\mathrm{P}} = 1565.1\mathrm{nm}$ and the different curves correspond to different pump powers $\overline{P}_{\mathrm{P}}^{\mathrm{i}}$. The filter is centered at $\lambda_{\mathrm{F}} = \lambda_{\mathrm{S}}$ and has a FWHM bandwidth of $\Delta\lambda_{\mathrm{F}} = 0.8\mathrm{nm}$. (b) CW transmission measured three months apart. The solid lines show Lorentzian fits to the measured data. A normalization is used so the peak transmission equals 1.

are normalized such that the transmission at "infinite" negative delay equals 1. This allows the switching contrast to be read off the ordinate axis, and very large values are observed. If it is again assumed that the pump does not transfer energy to the signal, Eq. (5.2.2) may be used to calculate the maximum contrast as the ratio $T_{\mathrm{U}}(0)/T_{\mathrm{U}}(\delta_{\mathrm{S}})$. As discussed above, the linear transmission at zero detuning is the maximally achievable, and $T_{\mathrm{U}}(\delta_{\mathrm{S}})$ equals the transmission at large negative delays. The maximum contrast depends on the detuning as well as the ratio between the signal bandwidth and cavity linewidth. If the input spectrum of the signal is assumed to be Lorentzian, the configuration in Fig. 5.6(a) yields a maximum contrast of a factor of 26, which is seen to be smaller than the observed values. Unlike Fig. 5.3, the results in Fig. 5.6(a) could be explained by the pump transferring energy to the signal, since the large contrast is only observed in a delay interval, which is comparable to the cavity lifetime. Unfortunately, we do not have a trace scanning the signal wavelength across the cavity resonance as in Fig. 5.3, so it is not possible to compare the linear transmission on resonance with the maximum nonlinear transmission in this case.

Other explanations may be given for the large switching contrast. In Fig. 5.6(b) the continuous wave (CW) transmission of the structure is measured and fitted with a Lorentzian lineshape. The setup used for this measurement is different from the one in Fig. 5.5 in that a tunable CW laser is

used to scan across the resonance while measuring the output power. The data in Fig. 5.6(b) has been normalized to a maximum transmission of 1. The two data sets were obtained three months apart, and it is evident that the resonance frequency has changed considerably. Dr. de Rossi and Dr. Combrié has experienced many difficulties with degradation of the samples, which is believed to be due to oxidation at the surfaces of the InP membrane. Such effects can be enhanced if large optical fields are transmitted through the sample as in the pump probe experiments. These effects may be the reason for the observed resonance changes. From Fig. 5.6(b) it is also seen that the Lorentzian approximation of the CW transmission does not agree very well with the measurement for large detunings such as that used in Fig. 5.6(a). The larger slope of the measured spectrum on the blue side of the resonance should result in a larger contrast than the expected, since $T_{\mathrm{U}}(\delta_{\mathrm{S}})$ is smaller than for a Lorentzian line shape.

Another, and perhaps more significant reason for the observation of a larger contrast is the fact that a filter is used before detection. In this case, the linear transmission should be calculated as

$$T_{\mathrm{U}}^{\mathrm{F}}\big(\delta_{\mathrm{S}},\Omega_{\mathrm{S}}\big)=\frac{\int T_{\mathrm{CW}}(\omega)P_{\mathrm{S}}^{\mathrm{i}}(\omega,\Omega_{\mathrm{S}})T_{\mathrm{F}}(\omega)d\omega}{\int P_{\mathrm{S}}^{\mathrm{i}}(\omega,\Omega_{\mathrm{S}})d\omega}, \tag{5.2.3}$$

where T_{F} is the transmission spectrum of the band pass filter. The maximum switching contrast is given by

$$C_{\mathrm{switch}}^{\max}\big(\delta_{\mathrm{S}},\Delta\omega_1,\Omega_{\mathrm{S}}\big)=\frac{T_{\mathrm{U}}^{\mathrm{F}}(0)}{T_{\mathrm{U}}^{\mathrm{F}}(\delta_{\mathrm{S}})}=\frac{\int T_{\mathrm{CW}}P_{\mathrm{S}}^{\mathrm{i}}(\omega_1,\Omega_{\mathrm{S}})T_{\mathrm{F}}d\omega}{\int T_{\mathrm{CW}}P_{\mathrm{S}}^{\mathrm{i}}(\omega_{\mathrm{S}},\Omega_{\mathrm{S}})T_{\mathrm{F}}d\omega}. \tag{5.2.4}$$

It is seen from Eq. (5.2.4) that introducing the filter effectively corresponds to using a pulse with a spectrum having steeper descending tales if the filter is fixed at the signal wavelength. The convolution of the cavity transmission and the effective signal spectrum will exhibit a strong dependence on the detuning δ_{S}, if either T_{CW} or $P_{\mathrm{S}}^{\mathrm{i}}\times T_{\mathrm{F}}$ has sharp spectral features. Figs. 5.7(a) and 5.7(b) illustrate this with an example using the parameters from Fig. 5.6(a). In Fig. 5.7(a) the model spectra are shown along with two examples of filter lineshapes. The corresponding maximum switching contrast as a function of detuning is depicted in Fig. 5.7(b). It is observed that the contrast increases significantly when a filter is used, and the values seen in Fig. 5.6(a) may be explained by this.

It is interesting to note how the maximum switching contrast is improved by filtering the output. In Chapter 8 it is investigated how the device performance may be improved by introducing sharper features in the cavity transmission, and Chapter 9 discusses how the properties of the input fields may be optimized.

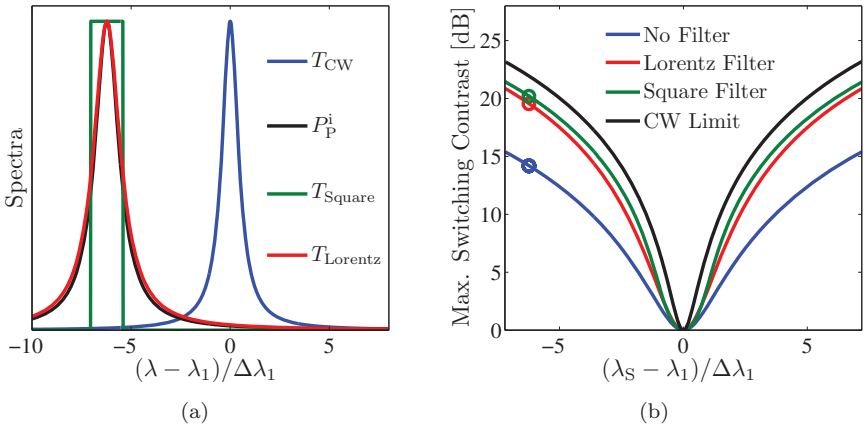

Figure 5.7: Illustration of the effect of filtering the output of the sample. (a) Lorentzian approximation of the cavity transmission (blue), spectrum of the input signal (black) along with a square (green) and Lorentzian (red) filter line shape. The parameters are the same as in Fig. 5.6(a). (b) Maximum switching contrast with the same parameters as in (a). The circles indicate the detuning corresponding to Fig. 5.6(a) and the black line indicates the limit of a CW input field or filter bandwidth approaching zero.

5.3 Heterodyne Pump Probe Measurements

The second type of time-domain experiment, which we will discuss, is the heterodyne pump probe measurement. The name comes from the fact that the signal is divided into two parts, where one serves as a reference for detection. The setup is shown in Fig. 5.8. The two parts of the signal are passed through

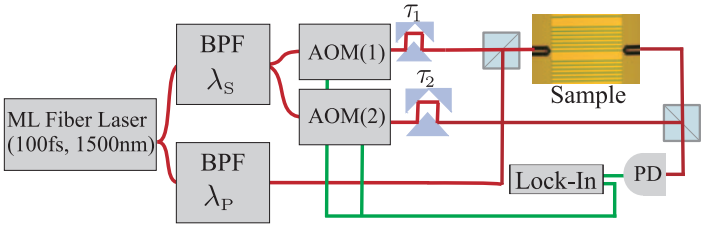

Figure 5.8: Schematic illustration of the setup for heterodyne pump probe experiments with the pump and signal co-propagation through the sample. The signal is split into two arms, which are frequency modulated by AOMs at different frequencies. The reference is delayed by τ_2 by passing through a separate delay line.

AOMs that introduce different microwave frequency shifts of $\Omega_1 = 80\text{MHz}$ and

$\Omega_2 = 82$MHz. The reference is needed for detection, where it interferes with the signal and the lock-in amplifier receives electrical reference signals from the AOMs enabling detection only at the difference frequency $\Omega_2 - \Omega_1$. The reference is also passed through a variable delay line to enable a convolution with the signal at the detector. The field arriving at the photo detector is $|s_{\mathrm{S}}^{\mathrm{i}}(t-\tau_2)\exp(i\Omega_2 t) + s_{\mathrm{S}}^{\mathrm{o}}(t-\tau_1)\exp(i\Omega_1)|^2$, where the first term is the reference and the second is the output from the sample. The beating terms are $s_{\mathrm{S}}^{\mathrm{i}}(t-\tau)s_{\mathrm{S}}^{\mathrm{o}*}(t-\tau_2)\exp(i\Delta\Omega) + c.c.$, and after integration in the photo detector, the electric signal is

$$S_{\mathrm{PD}}(t) = \exp(i\Delta\Omega t)\int_{\mathrm{pulse}} s_{\mathrm{S}}^{\mathrm{i}}(t-\tau_2)s_{\mathrm{S}}^{\mathrm{o}*}(t-\tau_1)dt + c.c., \tag{5.3.1}$$

where the integration is only over the pulse duration. Eq. (5.3.1) is valid if the response time of the detector is much slower than the pulse duration, but fast enough to detect the frequency difference $\Delta\Omega$ of the AOMs. The lock-in signal is given by

$$\begin{aligned} S_{\mathrm{L}}(\tau_1,\tau_2) &= \sqrt{\overline{S_{\mathrm{PD}}(t)\cos(\Delta\Omega t)}^2 + \overline{S_{\mathrm{PD}}(t)\sin(\Delta\Omega t)}^2} \quad \Rightarrow \\ S_{\mathrm{L}}(\tau_1,\tau_2) &= \int_{\mathrm{pulse}} \left| s_{\mathrm{S}}^{\mathrm{i}}(t-\tau_2)s_{\mathrm{S}}^{\mathrm{o}*}(t-\tau_1)\right| dt, \end{aligned} \tag{5.3.2}$$

where the bar denotes a time average. If the pulse shapes of the input and output are identical and $\tau_2 = \tau_1$, it is seen from Eq. (5.3.2) that the ratio $S_{\mathrm{L}}(\tau_1,\tau_2)/S_{\mathrm{L}}(-\infty,\tau_2)$ equals the ratio of the output energies and therefore also the ratio of the transmission in the nonlinear and linear regime. In waveguide systems, this will usually be the case [51], but for waveguide-cavity structures the shape of the output signal may be significantly distorted compared to the input. Hence, the lock-in signal does not correspond exactly to the output energy of the signal. The dependence on τ_2 may be removed in various ways, and in Fig. 5.9 we show results obtained by integrating S_{L} over τ_2. The three panels correspond to different signal detunings and in each panel, the pump power is varied. Even though the lock-in signal does not measure the energy transmission directly, the observed behavior in Fig. 5.9 is as expected for $T_{\mathrm{U}}(\delta_{\mathrm{S}},\tau_1)$. When the signal is on resonance, the transmission drops since the resonance is shifted away from the center wavelength of the signal (Fig. 5.9(a)). At an intermediate detuning, the transmission increases as the resonance is shifted towards the signal due to FCD (Fig. 5.9(b)). The increase saturates at a certain power level indicating that the resonance has been shifted by an amount equal to the detuning. At a large detuning, there is no saturation of the increase in transmission for the power levels used in Fig. 5.9(c). The details of the dynamical behavior observed in Fig. 5.9 are discussed in the next section, where we also compare with simulations using the temporal coupled mode theory (TCMT) model developed in Chapter 3.

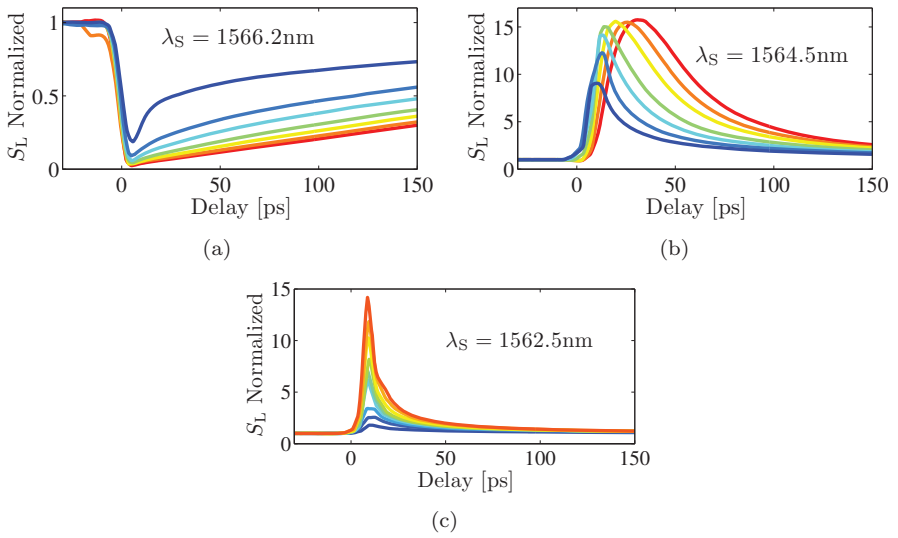

Figure 5.9: Pump probe measurement using the setup in Fig. 5.8. A sketch of the sample in the measurement is shown in Fig. 5.10(a) and is similar to that of Section 5.2. The resonance wavelength is measured to be $\lambda_1 =$ 1566.2nm, and the total quality factor equals 3400. The pump is on resonance $\lambda_P = \lambda_1$ and the lock-in signal S_L is normalized to 1 at large negative delays in all three cases. (a) Signal on resonance. The pump power is varied from $\overline{P}_P^i = 7\mu$W (blue) to 60μW (red). (b) Intermediate signal detuning. The pump is varied from $\overline{P}_P^i = 15\mu$W (blue) to 60μW (red). (c) Large signal detuning. The pump power is varied from $\overline{P}_P^i = 15\mu$W (blue) to 75μW (red). (Measurement performed by A. de Rossi).

5.4 Comparison with Modeling Results

The band gap of InP is larger than the energy corresponding to the wavelength range of interest here, so linear absorption may be neglected in Eq. (3.4.9). The dynamical changes of the material observed in the previous section happen on time scales shorter than the thermal relaxation time, so a constant temperature is assumed. With these assumptions and including the nonlinearities discussed in Chapter 3, the cavity field is governed by Eq. (3.4.10), which we state again for convenience

$$\frac{da(t)}{dt} = -i\left[\delta_P + K_{FCD}N_1(t) - K_{Kerr}|a(t)|^2\right]a(t) - \left[\gamma_C + K_{FCA}N_1(t) + K_{TP}|a(t)|^2\right]a(t) + \sqrt{\gamma_1}s_{1+}(t) \quad (5.4.1)$$

The problem of separating the pump and signal at the output waveguide when using a single mode cavity is also present from a modeling perspective. Since

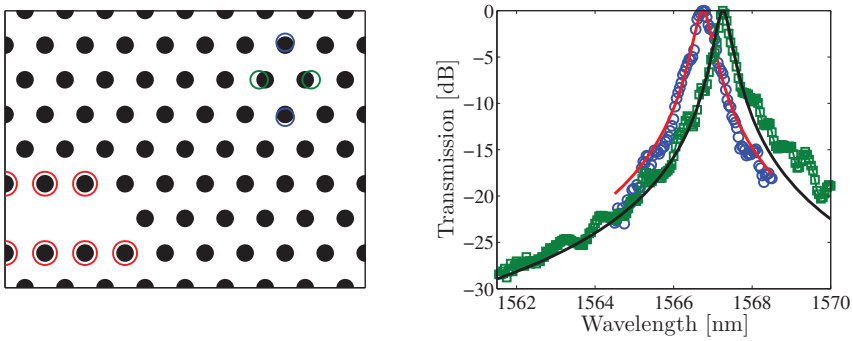

(a) (b)

Figure 5.10: Properties of the structure used in the experiments in this section. (a) Design details of the structure (the second waveguide is symmetrically placed as in Fig. 3.2, but not shown). It is noted that this structure is designed by our collaborators in the EU project "Copernicus" from the university of Ferrara in Italy. The red circles show holes with a radius of $0.3a$, the green circles are shifted by $\delta x = 0.15a$, and the blue circles indicate holes that are shift by $\delta y = 0.07a$. The lattice holes have radii of $r_0 = 0.22a$ and the membrane thickness is $d = 250$nm. (b) Linear characterization of the sample in (a). The green squares show the measurement before any nonlinear experiments had been performed on the sample, and the blue circles show a measurement taken at the same time as the pump probe experiments in this section. Unfortunately, the blue trace does not cover the same wavelength range, but it seems that the good agreement with the Lorentzian fit for the green squares has gotten worse in the second measurement.

the signal is assumed to be much weaker than the pump, the input field may be written as

$$s_{1+}(t) = f_0(t) + \zeta f_1(t-\tau_1)\exp[-i(\omega_S - \omega_P)(t-\tau_1)], \tag{5.4.2}$$

where f_0 and f_1 represent the pump and signal, respectively. The fast oscillation is defined as the pump frequency, $\omega_L = \omega_P$ in Eq. (2.2.20), and ζ is a small parameter. Since the input spectra of f_0 and f_1 overlap, as seen in Fig. 5.2, it is not possible to distinguish between contributions originating from f_0 and f_1 in the output, given by $f_{out}(t) = \sqrt{\gamma_1}a(t)$. The correct approach is to multiply f_1 by either $\cos[\Omega_{mod}(t-\tau_1)]$ or $\exp[i\Omega_1(t-\tau_1)]$ from the modulation in the homodyne and heterodyne techniques, and model the entire experimental process. This is time consuming due to the very different time scales appearing in the equations in this case as well as the large number of fitting parameters in the model. Therefore, we shall adopt a simpler approach in which the cavity

field is expanded in the small parameter ζ

$$a(t,\zeta) = a_0(t) + a_1(t) + \mathcal{O}(\zeta^2), \quad \text{where} \tag{5.4.3}$$

$$a_0(t) = a(t,0) \quad \text{and} \quad a_1(t) = \frac{\partial a(t,0)}{\partial \zeta}\zeta. \tag{5.4.4}$$

Including only zero order terms in ζ, Eq. (5.4.1) becomes

$$\frac{da_0}{dt} = -i\left[\delta_{\mathrm{P}} + K_{\mathrm{FCD}}N_1 - K_{\mathrm{Kerr}}|a_0|^2\right]a_0 - \left[\gamma_{\mathrm{C}} + K_{\mathrm{FCA}}N_1 + K_{\mathrm{TP}}|a_0|^2\right]a_0 + \sqrt{\gamma_1}f_0. \tag{5.4.5}$$

Collecting terms proportional to ζ, the equation for a_1 is

$$\frac{da_1}{dt} = \left[-i\delta_{\mathrm{P}} - \gamma_{\mathrm{C}} - (iK_{\mathrm{FCD}} + K_{\mathrm{FCA}})N_1\right]a_1 + (iK_{\mathrm{Kerr}} - K_{\mathrm{TP}})\left(2|a_0|^2a_1 + a_1^*a_0^2\right) + \sqrt{\gamma_1}\zeta f_1(t-\tau)\exp[-i(\omega_{\mathrm{S}} - \omega_{\mathrm{P}})(t-\tau_1)]. \tag{5.4.6}$$

The response when only the pump is coupled into the cavity is a_0, and a_1 describes the first order correction when the signal is applied as well. We interpret a_1 as the response of the signal when both fields are coupled into the cavity and use $\sqrt{\gamma_1}a_1^*$ as $s_{\mathrm{S}}^{\mathrm{o}*}$ in Eq. (5.3.1). The interpretation fits well with the physical picture that the pump changes the properties of the material, which is subsequently probed by the signal. Mathematically, Eq. (5.4.5) may be solved first along with Eqs. (3.4.7) and (3.4.6) for the material response, which can then be inserted into Eq. (5.4.6) for a_1. The wave mixing term $a_1^*a_0^2$ generates new frequencies around $2\omega_{\mathrm{P}} - \omega_{\mathrm{S}}$ and a label (like the $\cos[\Omega_{\mathrm{mod}}t]$) is needed to identify the origin of these new waves. Again, since we avoid such a labeling, the term is neglected. Mathematically, the term will be small compared to $2|a_0|^2a_1$ if the frequency separation of the pump and probe is large relative to their bandwidths. The expansion in ζ should have been done for N_1 as well and included in Eq. (3.4.9), but this results in similar mixing terms, which are also neglected.

Let us state all the equations of the model with the assumptions mentioned

above

$$\frac{da_0}{dt} = \left[-i\delta_{\mathrm{P}} - \gamma_{\mathrm{C}} + (iK_{\mathrm{FCD}} - K_{\mathrm{FCA}})N_1\right] a_0 + \left[(iK_{\mathrm{Kerr}} - K_{\mathrm{TP}})|a_0|^2\right] a_0 + \sqrt{\gamma_1} s_{\mathrm{P}}^{\mathrm{i}} \tag{5.4.7a}$$

$$\frac{da_1}{dt} = -i\left[\delta_{\mathrm{P}} + \delta_{\mathrm{NL}}\right] a_1 - \left[\gamma_{\mathrm{C}} + \gamma_{\mathrm{NL}}\right] a_1 + \sqrt{\gamma_1} s_{\mathrm{S}}^{\mathrm{i}}(t-\tau_1) e^{[-i(\omega_{\mathrm{S}}-\omega_{\mathrm{P}})(t-\tau_1)]} \tag{5.4.7b}$$

$$\frac{dN_1}{dt} = -\frac{1}{\tau_{\mathrm{diff}}}\Delta N - \frac{1}{\tau_{\mathrm{nr}}} N_1 + \frac{K_{\mathrm{TP}}}{\hbar\omega_{\mathrm{R}} V_1}|a_0|^4 \tag{5.4.7c}$$

$$\frac{dN_2}{dt} = \frac{1}{\tau_{\mathrm{diff}}}\Delta N \frac{V_1}{V_2} - \frac{1}{\tau_{\mathrm{nr}}} N_2 \tag{5.4.7d}$$

$$\delta_{\mathrm{NL}} = K_{\mathrm{FCD}} N_1 - 2K_{\mathrm{Kerr}}|a_0|^2 \tag{5.4.7e}$$

$$\gamma_{\mathrm{NL}} = K_{\mathrm{FCA}} N_1 + 2K_{\mathrm{TP}}|a_0|^2 \tag{5.4.7f}$$

$$s_{\mathrm{S}}^{\mathrm{o}} = \sqrt{\gamma_1} a_1. \tag{5.4.7g}$$

The time dependence of the parameters is only written explicitly for the signal input. The perturbations of the real- and imaginary part of the eigenfrequency for the signal are introduced by the functions δ_{NL} and γ_{NL}, respectively. Some of the parameters in Eq. (5.4.7) can be calculated from finite difference time domain (FDTD) simulations, while others must be used as fitting parameters when comparing with the experimental data.

To improve the basis for such a comparison, another type of experiment is performed to provide additional information. It consists of passing only the pump through the sample and measuring the input and output spectra as a function of pump power. Results from such a measurement are shown in Fig. 5.11. The output spectra are observed to broaden towards shorter wavelengths with increasing pump power, which is consistent with a decrease in the refractive index caused by FCD. Even though the transmission blue-shifts as seen from Fig. 5.11(b), a significant part of the output spectrum is located near λ_1. Because the resonance shift happens dynamically during the passage of the pulse, some of the majority of the pulse energy centered at λ_1 is transmitted, which gives rise to the double peak feature observed in Fig. 5.11(a).

Eq. (5.4.7) contains a substantial number of parameters, which are not known with good accuracy, so a strategy for fitting to the experimental data should be devised. Here, we choose a few representative data sets from both the spectral- and pump probe measurements. In Fig. 5.10(b) it is shown that the CW transmission of the sample used in these experiments showed a good agreement with a Lorentzian line shape when it was originally characterized. However, the measurement of the CW transmission taken at the same time as the other experiments in this section, indicates that the agreement has gotten worse at large detunings. For this reason, only pump probe measurements

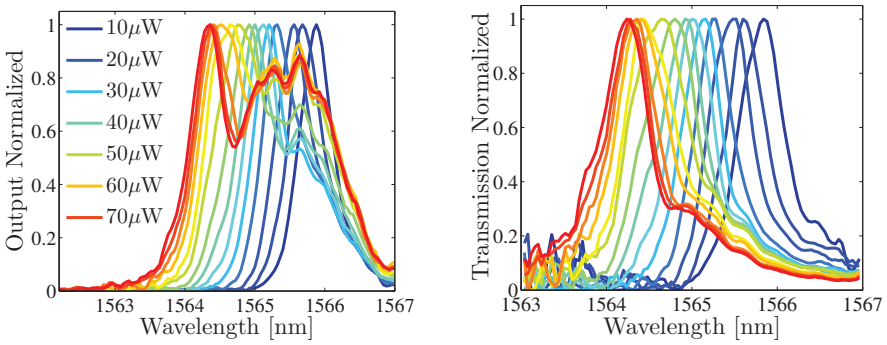

(a) (b)

Figure 5.11: Frequency domain measurements where the pump is on resonance $\lambda_P = \lambda_1 = 1566.2$nm and the spectrum of the output is measured with an optical spectrum analyzer while the power $\overline{P}_P^i$ is increased. The sample is the same as in Fig. 5.9. (a) Output spectra normalized to have a peak value of one. (b) Transmission spectra using the same normalization as in (a). (Measurement performed by A. de Rossi).

from Figs. 5.9(a) and 5.9(b) are included in the model comparison. Three different power levels (20μW, 40μW, and 60μW) are chosen at the signal wavelengths $\lambda_S = 1566.2$nm and 1564.5nm, while four different power levels (10μW, 20μW, 40μW, and 60μW) are chosen from the spectral measurements. Furthermore, the time-domain data is compared with the model result for S_L in Eq. (5.3.2) by integrating over τ_2 as well as the result from taking the maximum value as a function of τ_2. The comparison is quantified by calculating overlap integrals of the data with the model result

$$O = \frac{\left|\int f(x)g^*(x)dx\right|^2}{\int f(x)f^*(x)dx \int g(x)g^*(x)dx}, \tag{5.4.8}$$

where f and g represent the data sets and simulation results, and x is delay or wavelength for the two experiments. The overlap O equals 1 if $f(x) = kg(x)$ for any constant k. The time-domain data is normalized to one at large detunings before the overlap is calculated, and thus, O will only approach 1 if $f \approx g$. For the spectral data, we only compare the shape of the curves and do not require agreement in the absolute values. Since the overlap integrals from all the data sets have values between 0 and 1, they can be multiplied together and the resulting product is used as a figure of merit for the overall agreement between the model and experimental data. In Figs. 5.12 and 5.13 we show the experimental data and simulations using Eq. (5.4.7). All the parameters are identical in both figures, except we allow a shift of the delay axis for the experimental data for each signal wavelength. This accounts for small differences in optical path length resulting in the signal reaching the

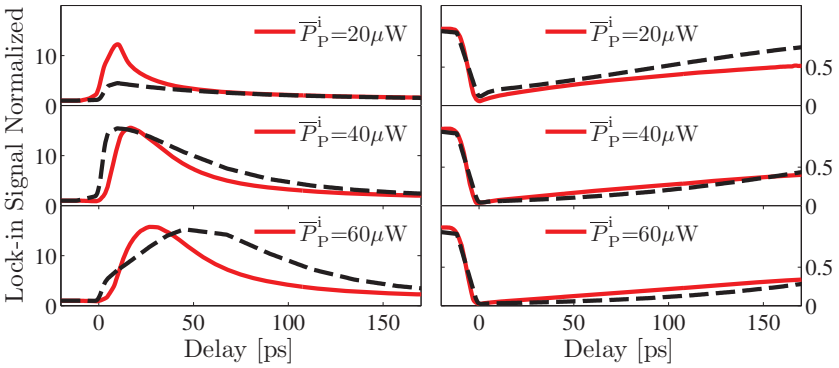

Figure 5.12: Comparison of experimental data and results from Eq. (5.4.7). The red lines show data from Figs. 5.9(a) and 5.9(b) and the dashed black lines are solutions of Eq. (5.4.7) using the parameters in Table 5.1.

cavity at different times. The origin of the delay-axis in Fig. 5.12 is that of the simulations. As mentioned above, only the shapes of the spectral curves are compared, so a normalization is used in Fig. 5.13 so the peak of the data and simulation result have the same value.

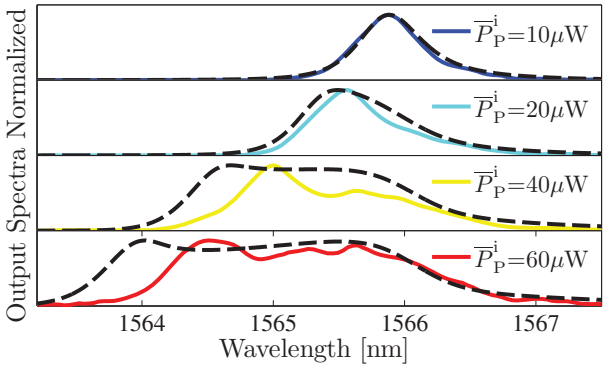

Figure 5.13: Comparison of experimental data and results from Eq. (5.4.7). The colored lines show data from Fig. 5.11(a) and the dashed black lines are simulations. Both curves are normalized to a peak value of 1.

Qualitatively, the model is able to reproduce the features of the measurements. However, it seems that the model underestimates the resonance shift at low pump power in the time-domain data, but matches well in the frequency-domain data. The spectra of the input pulses used in the simulations are assumed to have Lorentzian line shapes (see Fig. 5.2). With the assumptions made in the model and the uncertainties related to the measurements, it is per-

haps not surprising that a good quantitative agreement is difficult to achieve. If only the time-domain measurements or only the spectral data are used to fit the model parameters, it is possible to get a better agreement, but not for a common set of parameters as in Figs. 5.12 and 5.13. In Appendix D we

Model Parameters

$\partial\epsilon_{\text{FCD}}/\partial N_1$	=	-3.30×10^{-26} m^3	V_1/V_2	=	3.3
$\partial\epsilon_{\text{FCA}}/\partial N_1$	=	5.26×10^{-27} m^3	$1/\gamma_{\text{diff}}$	=	8ps
$\text{Im}\{\chi^{(3)}\}$	=	4.19×10^{-18} m^2/V^2	$1/\gamma_{\text{nr}}$	=	150ps
$\text{Re}\{\chi^{(3)}\}$	=	2.70×10^{-18} m^2/V^2	$\gamma_1/\gamma_{\text{C}}$	=	0.98
V_1	=	0.92 $(\lambda_{\text{C}}/n_{\text{R}})^3$	T_{coup}	=	0.06
V_χ	=	(280-i38)×$(\lambda_{\text{C}}/n_{\text{R}})^3$	ζ_{N1}	=	0.0213 + i0.0017
α_{TPA}	=	94cm/GW	σ_{FCA}	=	0.23×10^{-17}cm^2

Table 5.1: Model parameter values. V_χ and ζ_{N1} are calculated from FDTD simulations using the structure in Fig. 5.10(a).

show results from such a separate comparison. From the effective parameters in Eq. (5.4.7) used in Figs. 5.12 and 5.13, the derived material parameters are listed in Table 5.1. Let us compare these with values found in the literature.

From Refs. [35, 54] the values of changes in the dielectric function are $\partial\epsilon_{\text{FCD}}/\partial N = -2.93\times10^{-26}\text{m}^3$ and $\partial\epsilon_{\text{FCA}}/\partial N = 1.06\times10^{-28}\text{m}^3$ by using an effective mass $m_e = 0.075m_0$ and a mobility $\mu_e = 5400\text{cm}^2/\text{Vs}$ [55]. From Eq. (3.4.3) the TPA coefficient is related to the imaginary part of the third order susceptibility by $\alpha_{\text{TPA}} = 3\omega\text{Im}\{\chi^{(3)}\}/(2c^2\epsilon_0\epsilon_{\text{r}})$. In Ref. [56] a value of 14.6cm/GW is given, and by extrapolating the values of $\text{Im}\{\chi^{(3)}_{xxxx}\}$ reported in Ref. [57] to a wavelength of 1566nm, the value is: $\text{Im}\{\chi^{(3)}\} = 2.95\times10^{-18}\text{m}^2/\text{V}^2$. The effective free carrier absorption (FCA) coefficient K_{FCA} is related to the absorption cross section by $\sigma_{\text{FCA}} = 2K_{\text{FCA}}n_{\text{R}}/c$, and in Ref. [56] a value of $7.2\times10^{-17}\text{cm}^2$ was obtained. A value of the Kerr coefficient is given in Ref. [58] and it is $\text{Re}\{\chi^{(3)}\} = 1.6\times10^{-17}\text{m}^2/\text{V}^2$.

There is a significant difference between some of the parameters in Table 5.1 and those found in the literature, but it also appears that there is no clear consensus on the values in the literature. It should also be noted that the large space of fitting parameters does not necessarily result in a unique set. In Tables D.1 and D.2 we list the parameters resulting from the fitting procedure, where only the time-domain or frequency-domain data are used in the comparison. It seems difficult to make clear conclusions from these results. The qualitative agreement between the model and experiments indicate that the relevant physical mechanisms are accounted for by the model, but one should be careful about making quantitative conclusions. To gain more insight into the relevance of the different terms in the model, the next section contains a

parameter investigation.

5.5 Parameter Dependence

To investigate the effect of the parameters in Eq. (5.4.7), we examine the changes in δ_{NL} and γ_{NL} as the parameters are changed individually. The pump pulse is centered at $\lambda_{\mathrm{P}} = \lambda_1$ and has a mean power of $\overline{P}^{\mathrm{i}}_{\mathrm{P}} = 40\mu\mathrm{W}$. It is common to all the figures in this section that the solid lines show the frequency shift represented on the left ordinate axis, while dashed lines show absorption changes represented on the right axis. The color scheme is chosen so blue corresponds to the lowest value of the varied parameter and the colors change gradually towards red for increasing values of the parameter. All parameter values are taken from Table 5.1.

In Fig. 5.14(a) the Kerr coefficient K_{Kerr} is varied. The Kerr effect causes

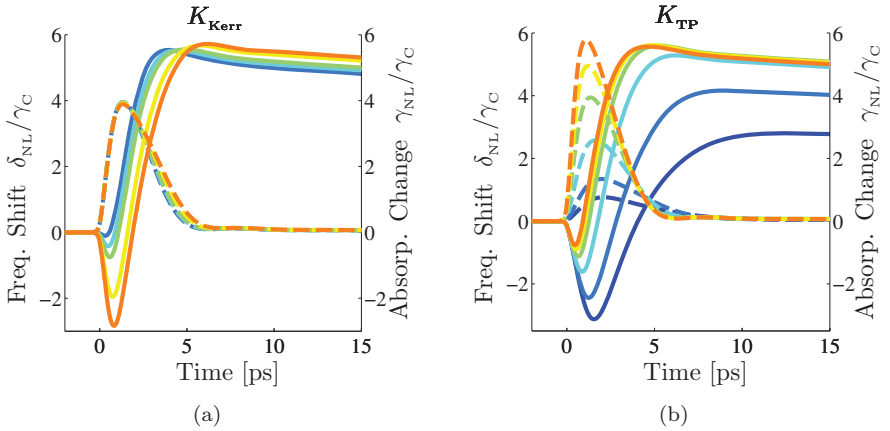

Figure 5.14: Dependence of the real and imaginary part of the nonlinear change in eigenfrequency. Solid lines correspond to the left axis and dashed lines belong to the right axis. (a) Different values of the Kerr coefficient K_{Kerr} from 0.2 (blue) to 2 (orange) times the value corresponding to Table 5.1. (b) Different values of the TPA coefficient K_{TP} from 0.1 (blue) to 2 (orange) times the value corresponding to Table 5.1.

a red-shift of the resonance, which is seen to be more pronounced as K_{Kerr} is increased. From Fig. 5.14(a) it is also seen that the build up of carriers, which causes a blue-shift of the resonance, reach the same level even at larger values of the Kerr coefficient. The effect on the absorption is observed to be negligible, except for small changes related to the build up of carriers. The steep slope of $\gamma_{\mathrm{NL}}(t)$ at short times and the small value at longer times indicate that TPA dominates over FCA in the nonlinear absorption. The dependence on the TPA coefficient K_{TP} shown in Fig. 5.14(b) is interesting. At relatively small values,

an increase in K_{TP} increases both the frequency shift and nonlinear absorption. This is due to the fact that more carriers are generated. However, at values close to the one in Table 5.1, it is seen that the frequency shift saturates while γ_{NL} increases significantly as K_{TP} is increased further. This means that

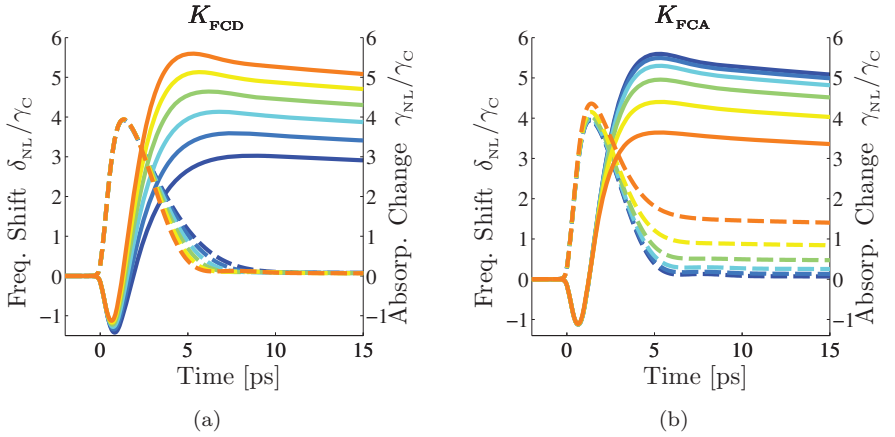

Figure 5.15: Dependence of the real and imaginary part of the nonlinear change in eigenfrequency. Solid lines correspond to the left axis and dashed lines belong to the right axis. (a) Different values of the FCD coefficient K_{FCD} from 0.5 (blue) to 1 (orange) times the value corresponding to Table 5.1. (b) Different values of the FCA coefficient K_{FCA} from 1 (blue) to 32 (orange) times the value corresponding to Table 5.1.

the nonlinear absorption becomes large enough to decrease the cavity field significantly and thereby decrease the carrier generation.

In Fig. 5.15(a) the effect of changing the FCD coefficient is depicted. The behavior is relatively simple in that the frequency shift increases with K_{FCD}, whereas the nonlinear absorption is almost unaffected.

The free carrier absorption coefficient is varied in Fig. 5.15(b). The initial part of the nonlinear absorption is still dominated by TPA, but as the carriers build up, it is observed that the absorption starts following the carrier density when K_{FCA} is increased sufficiently. The increase in K_{FCA} results in a decrease of the cavity energy, which causes a smaller carrier density and thereby a smaller resonance shift.

Fig. 5.16(a) shows how the dynamics depend on the volume ratio V_1/V_2. The interpretation of this ratio is related to the amount of time, in which carriers may flow from the initial to the secondary carrier distribution discussed in Section 3.4. If the ratio is large, it is seen from Eq. (5.4.7d) that the secondary distribution fills up fast, after which the exchange of carriers between the distributions is small and the carrier relaxation is dominated by the slow time constant. This is illustrated in Fig. 5.16(a), where the blue curve indicates a fast carrier relaxation and a small volume ratio, whereas the orange curve

indicates a slow relaxation for a larger volume ratio. The nonlinear absorption is basically unaffected, since it is dominated by TPA in this case.

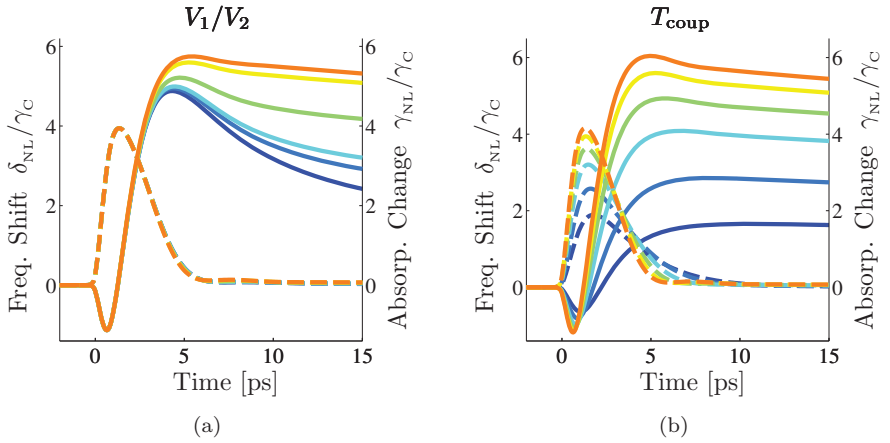

Figure 5.16: Dependence of the real and imaginary part of the nonlinear change in eigenfrequency. Solid lines correspond to the left axis and dashed lines belong to the right axis. (a) Different values of the volume ratio V_1/V_2 from 0.125 (blue) to 1.25 (orange) times the value corresponding to Table 5.1. (b) Different values of the coupling constant T_{coup} from 0.1 (blue) to 1.2 (orange) times the value corresponding to Table 5.1.

In Fig. 5.16(b) the effect of increasing the coupling into the device is shown. This basically corresponds to increasing the pump power, and it is observed that both the frequency shift and absorption increases due to the increased cavity energy and carrier density.

6

Four Port Structure

6.1 Introduction

In this chapter, we address how the difficulties in measuring the nonlinear dynamics in single-mode cavity devices may be overcome. The suggested solution is to use separate waveguides for the pump and signal, which means that four ports are required. The pump and signal will be spatially separated at the output, such that no filtering or additional modulation of the two light fields is required. A real device should be functional without any of the modulation techniques discussed in Chapter 5, so for a two port structure, the only means of separating the fields is spectral filtering. However, the wavelength configuration of the pump and signal relative to the cavity resonance, which minimizes the switching energy, may not be compatible with a filtering scheme since the wavelengths could be close compared to the spectral widths of the fields. The accompanying increase in switching energy is avoided by using spatial filtering, which also provides additional flexibility in terms of independent tuning of the coupling rates γ_{mn} experienced by the pump and the signal.

The price to pay for the advantages of a four port structure lies in the increased design and fabrication complexity. Below we shall describe how a four port structure may be formed, which fulfills the spatial separation requirement while being relatively simple from a fabrication viewpoint.

6.2 Structure Design

In this section we shall consider the design of a multi-mode cavity coupled to four ports. The idea for such a design is inspired by Ref. [59] and in particular Ref. [60]. The key difference is that the design presented below uses a single hole size. The cavity under consideration is denoted an H1 cavity, since it is formed by removing one hole from the photonic crystal (PC) lattice. The cavity has six modes [61] and we shall concentrate on the degenerate quadrupole

modes as in Ref. [60]. The transmission elements T_{jk} represent the transmission from port j to port k and since the structure is reciprocal such that $T_{jk} = T_{kj}$, we may group the 4 ports in two pairs, which are denoted waveguide 1 (WG1) and 2 (WG2), respectively. The range of j and k is then limited to 1 and 2, such that e.g. T_{12} represents the transmission from WG1 to WG2. In order to achieve spatial separation of the pump and signal at the output, it is necessary to minimize the cross-talk between WG1 and WG2 while maximizing the transmission from the input to the output of either waveguide. In terms of the transmission elements, this means $T_{jk} \approx 0$ and $T_{jj} \approx 1$. The cavity design is shown in Fig. 6.1. In order to eliminate cross-talk, the waveguides must couple

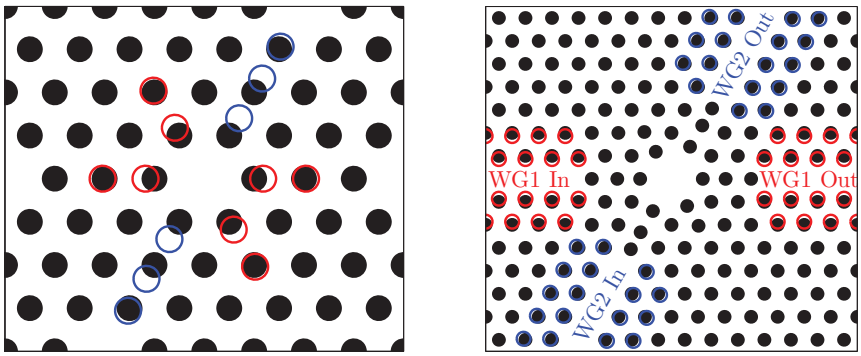

Figure 6.1: Top view of the four port structure. (a) The holes surrounding the cavity are shifted as illustrated by the colored rings. The shifts are denoted $l_{11c} = 0.18a$, $l_{12c} = 0.04a$ (red), $l_{21c} = 0.42a$, $l_{22c} = 0.34a$, and $l_{23c} = 0.06a$ (blue), where the first subscript enumerates the modes, the second denotes the distance of the shifted hole to the cavity center ("1" means the first ring around the cavity center, "2" the second, etc.), and the "c" indicates that the shifted holes are near the cavity. (b) A zoom-out showing the four ports. The holes near the waveguides are shifted by $l_{11p} = 0.12a$, $l_{12p} = 0.12a$ (red), $l_{21p} = -0.08a$, and $l_{22p} = -0.08a$ (blue), where the first subscript enumerates the waveguide, the second indicates the distance to the waveguide axis ("1" means the closest row and "2" the second closest), and the p signifies that the shift is perpendicular to the waveguide axis. The hole radii are $r_0 = 0.26a$, and the membrane thickness is $d = 0.77a$.

to two different cavity modes with different resonance frequencies. Furthermore, each mode must couple to only one of the waveguides. The quadrupole modes are degenerate in the symmetric case, where only the central hole is removed [61], so the neighboring holes must be shifted to break the symmetry and separate the eigenfrequencies. In Fig. 6.1(a) it is shown how the holes close to the cavity are shifted. The reasoning for shifting these specific holes may be explained by considering the eigenmodes, which are shown in Fig. 6.2. The

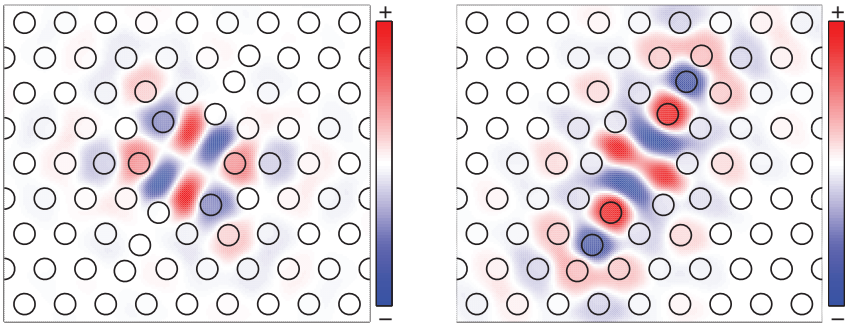

(a) (b)

Figure 6.2: Quadrupole eigenmodes ($\mathrm{Re}\{H_z\}$) of the cavity design shown in Fig. 6.1, except the membrane thickness is $d=0.8a$ here. (a) Mode 1, which couples to waveguide 1, has a resonance frequency of $\omega_1 = 0.2826\times 2\pi c/a$. (b) Mode 2, which couples to waveguide 2, has a resonance frequency of $\omega_2 = 0.2725\times 2\pi c/a$.

field distribution of mode 1 (M1) seen in Fig. 6.2(a) is large close to the red circles in Fig. 6.1(a) relative to the distribution of mode 2 shown in Fig. 6.2(b). Thus, shifting these holes is expected to predominantly affect the resonance frequency of M1. Similarly, mode 2 (M2) has a high field density around the blue circles in Fig. 6.1(a) relative to mode 1. By shifting the blue holes further away from the center than the red, mode 1 is expected to have a larger resonance frequency than mode 2, since mode 2 will distribute itself over a larger region, cf. Section 4.3.

There are two ways to ensure that each mode only couples to one of the waveguides. One is to utilize symmetry-mismatch between the cavity- and waveguide modes, and the other is to design the waveguides to have a band gap at one of the cavity resonances. From Fig. 6.2(a) it is seen that mode 1 is odd with respect to reflections in the central axis of WG2. The even mode of WG2 is therefore not expected to couple to M1. The odd mode, however, will couple to M1 unless the dispersion of WG2 is designed such that ω_1 lies outside the frequency range of the odd mode of WG2. To get a better overview of our design possibilities, the effects of three different types of hole shifts on the band diagram of the waveguide are investigated in Fig. 6.3. The upper panels illustrate the shifts, and the lower panels show the corresponding changes in the dispersion curves.

As in Fig. 1.3(a), it is seen from Fig. 6.3(d) that a perpendicular shift of the closest holes blue-shifts the mode frequencies and also separates the even and odd modes.

The effect of a perpendicular shift of the second row of holes is largest where the mode profile extends furthest away from the waveguide axis. This is the

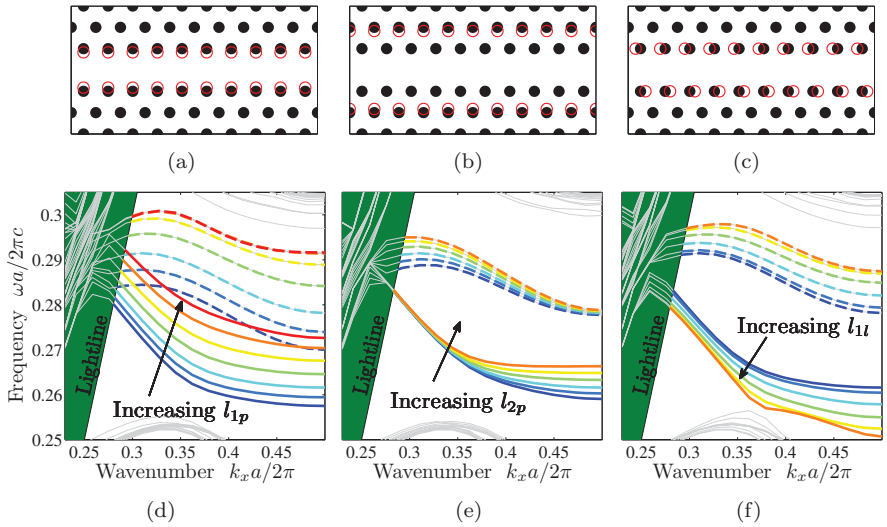

Figure 6.3: Modification of the band diagram of PC membrane waveguides for three types of hole shifts. The upper panels illustrate the shift types, and the corresponding band diagrams are shown in the lower panels. As in Fig. 1.3(a), the solid lines correspond to even modes, wile dashed lines correspond to odd modes. (a) and (d) show the effect of shifting the first row perpendicularly towards the waveguide axis by l_{1p} in the range -0.1a (blue) to 0.2a (red), while fixing l_{2p} and l_{1l} at 0. (b) and (e) shows the same for the second row of holes, where l_{2p} is varied between -0.1a (blue) and 0.15a (orange), while $l_{1p} = l_{1h} = 0$. (c) and (f) displays the effect of a longitudinal shift of the first row by l_{1l} in opposite directions along the waveguide axis above and below the line-defect in the interval 0 (blue) to 0.25a (orange). The parameters in all three cases are: $d = 0.77a$ and $r_0 = 0.26a$.

case in the slow light regime of the even mode and close to the light line for the odd mode. It is interesting to note that the dispersion curve of the even mode becomes flatter in the slow light regime when l_{2p} is increased. This may prove to be useful since it essentially reduces the necessary frequency separation of the cavity modes.

The hole shifts shown in Fig. 6.3(c) break the mirror symmetry of the waveguide axis, and the modes may no longer be classified as even or odd with respect to reflections in the waveguide axis. It is observed that increasing l_{1l} results in a significant splitting of the even-like and odd-like bands, which may be understood from arguments based on group symmetry theory [62].

At least two different schemes for minimizing the cross-talk may be envisioned from the results in Fig. 6.3. One is based on perpendicular shifts alone and is illustrated in Fig. 6.4(a), while the second is based on a combination of

perpendicular and longitudinal shifts and is shown in Fig. 6.4(b). In the first

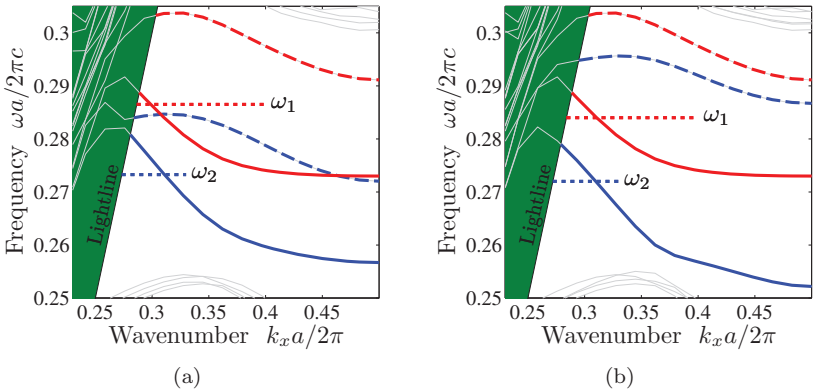

Figure 6.4: Specific waveguide designs for minimized cross-talk. All parameters are the same as in Fig. 6.3. (a) Design with $l_{11p} = 0.12a$, $l_{12p} = 0.12a$, $l_{11l} = 0$, $l_{12l} = 0$, $l_{21p} = -0.08a$, $l_{22p} = -0.08a$, and $l_{21l} = 0$. (b) Design with $l_{11p} = 0.12a$, $l_{12p} = 0.12a$, $l_{11l} = 0$, $l_{12l} = 0$, $l_{21p} = -0.03a$, $l_{22p} = 0$, and $l_{21l} = 0.2a$. The frequencies ω_1 and ω_2 show examples of the location of the resonances of the two modes to achieve zero cross-talk.

scheme, the first and second rows of holes are shifted towards the waveguide axis by $0.12a$ in WG1, whereas the rows in WG2 are shifted away from the axis by $0.08a$. From Fig. 6.4(a) it is evident that the dispersion curves are separated sufficiently to enable zero cross-talk, if the cavity frequencies are placed as shown. The second scheme uses the same configuration for WG1, but in WG2 the first row is shifted slightly away from the waveguide axis as well as longitudinally. As it is seen from Fig. 6.4(b), the splitting of the even-like and odd-like mode is sufficiently large for the even mode of WG1 to be placed in between. Again, this provides a way of removing the cross-talk.

The four port design considered in this chapter has been fabricated and characterized by Yi Yu from our group, and the results may be found in Ref. [63]. The device in Ref. [63] is based on the first design scheme mentioned above. For completeness we show simulation results for a design based on the second scheme in Fig. 6.5. The magnetic field intensity is overlaid on the structure to illustrate how the two cavity modes only couple to one of the waveguides. The structure contains bends that are designed with inspiration from topology optimized structures [64]. Each bend is an annulus with a thickness of r_0 and a radius of curvature, which makes it follow the bend smoothly. The mode profiles in Figs. 6.5(a) and 6.5(b) are found from finite difference time domain (FDTD) simulations by placing a transient source in either WG1 or WG2 to the left of the PC structure. After the transient time, the power flux passing through WG1 and WG2 on the right side of the structure was

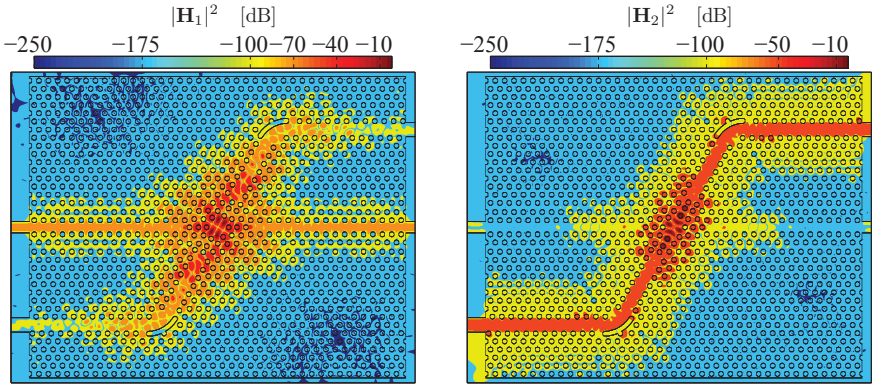

Figure 6.5: Modes of the four port cross waveguide structure corresponding to the design scheme in Fig. 6.4(b). The parameters are: $l_{11c}=0.18a$, $l_{12c}=0.04a$, $l_{21c}=0.4a$, $l_{22c}=0.32a$, $l_{23c}=0.06a$, while the rest are the same as in Fig. 6.4(b). The fields are normalized to a peak of 1, and the displayed contours match the numbers on the color bars. A bend is introduced in WG2 to make the structure more compact. (a) Mode 1. (b) Mode 2.

monitored in time. Fig. 6.6 shows the power ratio between the waveguides, P_1^o/P_2^o for an excitation of WG2 and P_2^o/P_1^o for an excitation of WG1. The

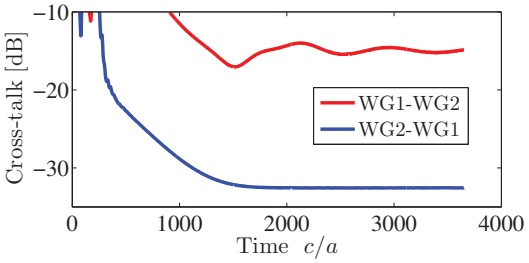

Figure 6.6: Ratios of power passing through the outputs of WG1 and WG2. The red curve is found by exciting the structure with a source in WG1 and monitoring P_2^o/P_1^o after the transient time of the source. The blue curve shows the ratio P_1^o/P_2^o after the transient time when exciting the structure with a source in WG2.

power leakage from WG2 to WG1 is less than -30dB, whereas the leakage from WG1 to WG2 is approximately -15dB. From the field pattern in Fig. 6.5(a) it is expected that the leakage from WG1 to WG2 can be reduced by increasing the length of the PC waveguide. The waveguide bands lying above the light line are exponentially decaying, but it requires a finite length of the waveguide

to completely suppress frequencies in the band gap of the infinite waveguide structure shown in Fig. 6.4(b).

We note that designs of the type shown in Fig. 6.5 has the important flexibility that the pump and signal may be separated spatially on the chip. Furthermore, the coupling between the cavity modes and the waveguides may be tuned independently allowing for the pump and signal to experience different quality factors. In the analysis of the cavity dynamics in the next chapter, this will turn out to be advantageous.

7

Energy-Bandwidth Trade-off

7.1 Introduction

In this chapter we shall use the temporal coupled mode theory (TCMT) model to analyze the trade-off between operation speed and switching energy, which persists in waveguide-cavity structures. The work is contained in Ref. [65]. There are several contributions to such a trade-off. The practically instantaneous Kerr nonlinearity is relatively weak compared to carrier induced nonlinearities such as free carrier dispersion (FCD), which, on the other hand, require a finite time to relax back to the initial state. Another important point for cavity structures is the trade-off between the field enhancement and increased photon lifetime as well as decreased transmission, which follows by increasing the quality factor. To simplify the analysis and ease interpretation, we shall restrict ourselves to an investigation of the latter only. Thus, we consider the real part of $\chi^{(3)}$ to be the only nonlinearity in the system. The analysis aims to investigate the limitations set by the cavity alone and should provide valuable information for use in designing structures. Increasing the photon lifetime reduces the switching energy, but also causes patterning effects, which restrict the signal bandwidth, hence the term "energy-bandwidth trade-off". Previous work [66] has considered patterning effects in semiconductor optical amplifier (SOA) based switches as well as the high bit rate performance of photonic crystal switches based on shifting the photonic band gap edge and an interferometric approach enhanced by the slow light property of photonic crystals [67]. We shall consider a generic waveguide-cavity structure with four ports coupling to two resonances as in Chapter 6. Even with the simplifications mentioned above, it will be shown that such a structure contains a rich dynamical behavior.

To make the energy-bandwidth trade-off quantitative, it is necessary to

introduce some figure of merit (FoM) for the switching performance. Since there are a large number of possible applications for a switching device, as discussed in Section 1.2, a single figure of merit does not quantify them all. Here, we shall consider demultiplexing of optical time division multiplexing (OTDM) signals as a particular application example.

7.2 TCMT Model

In Chapter 6 it was seen that four port structures may by designed with negligible cross-talk. We shall consider such a structure with a mirror-plane at $x=0$, which allows us to reduce the number of independent coupling rates. The model is further simplified by neglecting direct scattering between the waveguides ($|t_1|=0$) and an infinite out-of-plane quality factor ($\gamma_\mathrm{C}=\gamma_1$). Including a nonlinearity consisting of only the real part of the third order susceptibility, the TCMT equations are

$$\dot{a}_\mathrm{S} = \left(-i\left[\delta_\mathrm{S} - K^{11}_\mathrm{Kerr}|a_\mathrm{S}|^2 - K^{12}_\mathrm{Kerr}|a_\mathrm{P}|^2\right] - \gamma_1\right) a_\mathrm{S} + \sqrt{\gamma_1}s^\mathrm{i}_\mathrm{S} \tag{7.2.1a}$$

$$\dot{a}_\mathrm{P} = \left(-i\left[\delta_\mathrm{P} - K^{21}_\mathrm{Kerr}|a_\mathrm{S}|^2 - K^{22}_\mathrm{Kerr}|a_\mathrm{P}|^2\right] - \gamma_2\right) a_\mathrm{P} + \sqrt{\gamma_2}s^\mathrm{i}_\mathrm{P} \tag{7.2.1b}$$

$$s^\mathrm{o}_\mathrm{S} = -\sqrt{\gamma_1}a_\mathrm{S} \quad \text{and} \quad s^\mathrm{o}_\mathrm{P} = \sqrt{\gamma_2}a_\mathrm{P}. \tag{7.2.1c}$$

It is seen from Eq. (7.2.1) that there is no linear coupling between the cavity modes a_S and a_P due to the assumption of zero cross-talk. The equations are only coupled via the nonlinearity, and Appendix A.3 contains the perturbation theory with two fields needed to evaluate the coefficients K^{jk}_Kerr with $j,k=1,2$. The work in this chapter was done prior to the perturbation analysis in Appendix A, so the values of K^{jk}_Kerr as well as the eigenfrequencies are taken from Ref. [59]. The relationship between the K^{jk}_Kerr coefficients and κ_{jk} from Ref. [59] is given by

$$K^{jj}_\mathrm{Kerr} = 10^{-3}\frac{a\omega_j^3\kappa_{jj}}{2\epsilon_\mathrm{r}c}\frac{1}{P_0} \quad \text{and} \quad K^{jk}_\mathrm{Kerr} = 10^{-3}\frac{a\omega_j^2\omega_j\kappa_{jk}}{\epsilon_\mathrm{r}c}\frac{1}{P_0}, \tag{7.2.2}$$

where $P_0=10^{-3}\epsilon_0 ac/\chi^{(3)}$ is the unit of power used here. The parameter values are: $\omega_1=2.344\ c/a$, $\omega_2=2.231\ c/a$, $\kappa_{11}=0.0943$, $\kappa_{22}=0.105$, $\kappa_{12}=0.0312$, and $\kappa_{21}=0.0343$. For an easy overview of the parameters in the model, they are illustrated in Fig. 7.1 along with an illustration of the signal and pump input spectra as well as the transmission spectra of the two modes.

7.3 Transmission of a Single Signal Pulse

In order to understand the dynamics of systems described by Eq. (7.2.1), we start by considering the case of a single signal pulse and no pump. The very

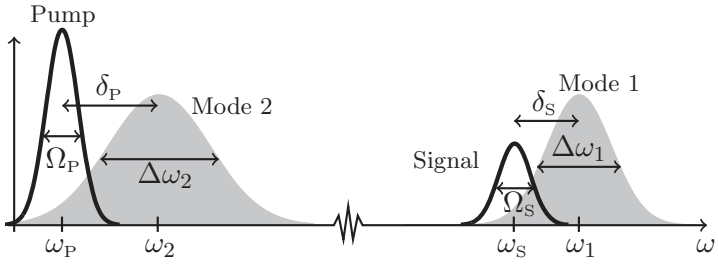

Figure 7.1: Illustration of the input power spectra of the signal and pump as well as the Lorentzian transmission spectra of the two cavity modes. The parameters of Eq. (7.2.1) are shown for easy reference.

short pulses employed in OTDM signals typically originate from mode-locked lasers, which emit pulses with a shape that is well approximated by a Gaussian function

$$P_S^i(t) = P_S^0 \exp\left[-\ln(2)\left(\frac{2t}{\Delta t_S}\right)^2\right],$$

where Δt_S is the full width at half maximum (FWHM) of the pulse.

First, we consider the transition from a quasi steady state regime of very long pulses to the case of ultra short pulses, where the pulse bandwidth Ω_S is larger than the cavity linewidth $\Delta\omega_1$. Although we will primarily focus on Gaussian pulses, it is more illustrative to use square pulses for this purpose, because the steady state appears as the limit of an infinitely long square pulse. While keeping the cavity linewidth constant, we have varied the peak power of the input pulse for different values of the pulse bandwidth. Fig. 7.2(a) shows the ratio of output energy and pulse width as a function of the input power for different values of $\Delta\omega_1/\Omega_S$ for a square pulse.

The steady state solution of Eq. (7.2.1a) is also plotted (dashed red) and agrees well with the results in [59]. It shows the same bistable behavior that was observed in Section 3.3.1. When the pulse bandwidth Ω_S is larger than the cavity linewidth $\Delta\omega_1$, the output energy shows local extrema as a function of input power. The same behavior is observed for a Gaussian pulse, which is shown in Fig. 7.2(b).

The reason for the appearance of the local extrema is oscillations in the output power as a function of time. To illustrate this point, Fig. 7.3 shows the input (black) and output (red) power corresponding to the local extrema indicated by green dots in Fig. 7.2(b). The oscillations reflect a purely linear phenomenon, which is most clearly illustrated by considering the solution of the linear part of Eq. (7.2.1a) in the case of a step function input

$$P_S^i(t) = P_S^0\Theta(t), \quad \Theta(t) = \begin{cases} 1 & \text{for} \quad t \geq 0 \\ 0 & \text{for} \quad t < 0 \end{cases}.$$

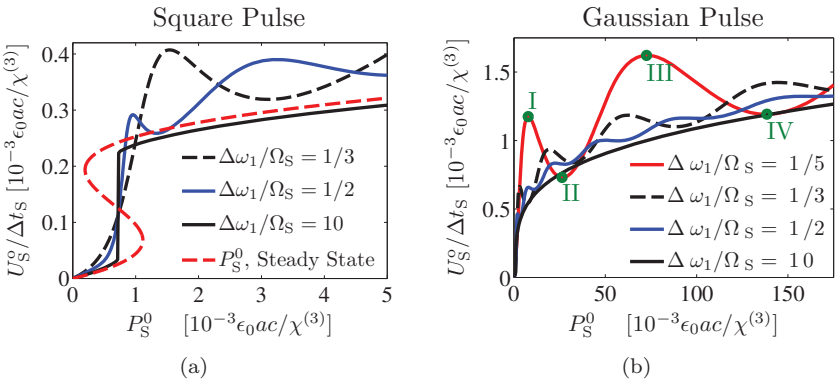

Figure 7.2: (a) Ratio of output energy to input pulse width as a function of the input peak power P_S^0 for a square pulse. The different curves correspond to different pulse widths, while the cavity linewidth is fixed. The dashed red line shows the characteristic bistability curve found from the steady state solution of Eq. (7.2.1a). (b) The same as (a), but for a Gaussian pulse. Notice the different scales on the abscissa in (a) and (b). The green dots indicate local extrema in the output as a function of P_S^0. The parameters are: $\Delta\omega_1 = 2.344 \times 10^{-3} c/a$ and $\delta_S = 3\Delta\omega_1$.

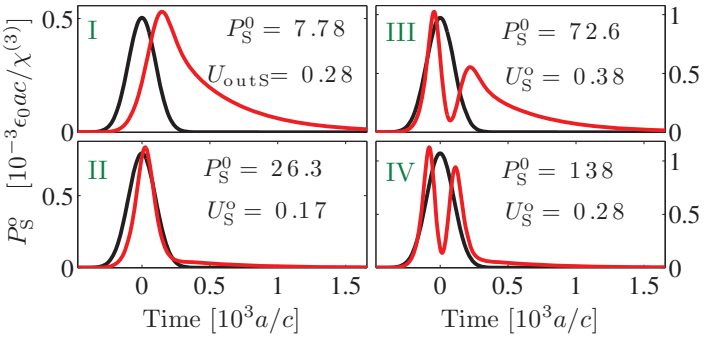

Figure 7.3: Input (black) and output (red) power of a Gaussian pulse with input powers corresponding to the green dots in Fig. 7.2(b). The curve of the input power has been scaled to be comparable to the output. The values of input power and output energy are given in units of $[10^{-3}\epsilon_0 ca/\chi^{(3)}]$ and $[\epsilon_0 a^2/\chi^{(3)}]$, respectively. The parameters are the same as in Fig. 7.2.

The output power can in this case be expressed analytically, and is given by

$$P_S^o(t) = P_S^0 \frac{\Delta\omega_1^2}{\Delta\omega_1^2 + 4\delta_S^2} \big[1 + \exp(-\Delta\omega_1 t) \; - \; 2\exp(-\Delta\omega_1 t/2)\cos(\delta_S t)\big]\Theta(t), \quad (7.3.1)$$

which oscillates with a period given by the detuning δ_S. The physical origin of the oscillations is a transient interference beating between the incoming pulse oscillating at ω_S and the excited cavity mode oscillating at ω_1. In the top left panel of Fig. 7.3, the oscillation period is $\sim$4 times the pulse width, and the output energy is at a local maximum. In the bottom left panel, the period is $\sim$2 times the pulse width and the output energy is at a local minimum. In the upper (lower) right panel, the oscillation period is $\sim 4/3$ ($\sim$1) times the pulse width and again the output energy is at a maximum (minimum). Thus, it makes a big difference whether the output pulse has reached a maximum or a minimum of the oscillation in a time determined by the pulse width. As the input power is varied, the instantaneous detuning $\delta_S - K^{11}_{\mathrm{Kerr}}|a_S(t)|^2$ changes due to the nonlinear frequency shift of the cavity. This, in turn, changes the effective oscillation period of the output pulse, causing the local extrema of the curves in Figs. 7.2(a) and 7.2(b). It is interesting to note that the fields in the upper panels of Fig. 7.3 escape the cavity in a time set by the photon lifetime, while the fields in the lower panels escape faster. As mentioned above, this is possible when the pulse width is close to an integer number of half oscillation periods. In Chapter 9 we will discuss further, how interference effects may allow us to drive energy in and out of the cavity arbitrarily fast.

The regime of short pulses, $\Delta\omega_1/\Omega_S < 1$, is thus seen to be qualitatively different from the quasi steady state regime, $\Delta\omega_1/\Omega_S > 1$. For short pulses, the nonlinear change of the resonance frequency relative to the *pulse bandwidth* has a significant effect on the transmission properties of the switch. For long pulses, the switching mechanism can be understood from the bistability curve in Fig. 7.2(a). By increasing the input power, the transmission jumps from a small to a large value. The criterion for the bistability to occur is $\delta_S > \sqrt{3}\gamma_C$, cf. Eq. (3.3.12), and therefore it is the change of resonance frequency relative to the *cavity linewidth*, which is important for the transmission in the quasi steady state regime.

Here, we have investigated the single pulse case in order to understand the more complicated case of de-multiplexing. However, single pulse transmission is also relevant for regeneration applications, where the S-shaped transfer function is used to improve the signal properties, [68]. In this case, the changes in pulse shape observed in Fig. 7.3 need to be considered in detail.

7.4 Demultiplexing a Data Signal

Since we are ultimately interested in the performance of switches in high speed data transmission systems, it is crucial to consider their operation on a sequence of pulses. For a demultiplexing application, the target signal pulse should be transmitted in the presence of a pump pulse, while its transmission should be as small as possible in the absence of the pump, see Section 1.2. The optical demultiplexing is necessary due to the limited response time of the electronics in the receiver. Here, and in Section 7.5 we will consider, as an example, a

detector with a response time of 80 ps corresponding to a bandwidth of 12.5 GHz. The total OTDM bandwidth that we will consider is 125 GHz, which corresponds to 10 channels. The detector thus integrates over 10 bit periods, and the decision between "0" or "1" is based on the amount of energy carried by the signal over the integration period. To avoid having to test all the possible bit sequences, we focus on a worst case scenario, where the difference in energy arriving at the detector in the "0" and "1" case is minimal. The maximum received energy in the case of a "0" occurs when the following 9 bits of the OTDM signal are all "1"s. This is shown in the left panel of Fig. 7.4(a) and we

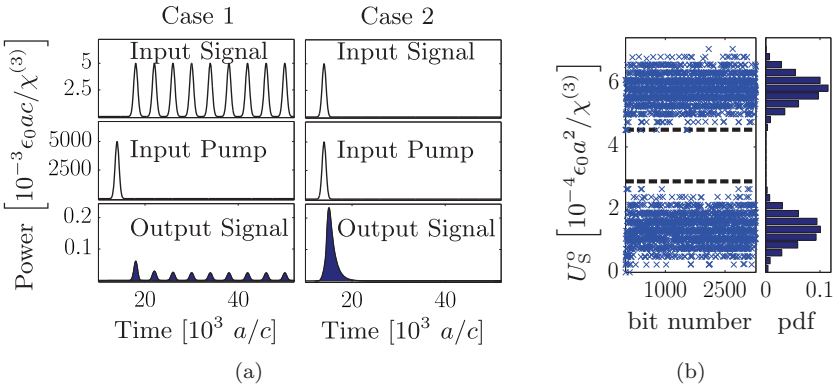

Figure 7.4: (a) left: The top graph shows the input signal, when the target bit slot is "0" and the following bits are all "1"s. The middle graph shows the input pump pulse in the target bit slot. The lower graph shows the corresponding signal output, and $U_{\mathrm{So}}^{0\{1\}}$ is given by the blue area under the curve. (a) right: The top graph shows the input signal, when the target bit is "1" followed by 9 "0"s. The middle graph shows the pump pulse. The lower graph shows the corresponding signal output, and $U_{\mathrm{So}}^{1\{0\}}$ is the area under the curve. (b) The left graph shows the detected energy for a PRBS consisting of $2^{15}-1$ bits. The dashed black lines indicate the worst case scenario energies, $U_{\mathrm{So}}^{1\{0\}}$ and $U_{\mathrm{So}}^{0\{1\}}$. The right graph shows the corresponding probability distribution function (pdf).

denote this energy $U_{\mathrm{So}}^{0\{1\}}$. The minimum received energy in the case of a "1" occurs when the following 9 bits are all "0"s. The right panel in Fig. 7.4(a) illustrates this case, and the corresponding energy is denoted $U_{\mathrm{So}}^{1\{0\}}$. A figure of merit (FoM) is defined to quantify the ability of the detector to distinguish between "0" and "1" bits in the signal. It is defined as the ratio between the two worst case energies

$$\mathrm{FoM} = \frac{U_{\mathrm{So}}^{1\{0\}}}{U_{\mathrm{So}}^{0\{1\}}}. \tag{7.4.1}$$

To achieve a large value of the FoM, it is important that the pump pulse exits the cavity fast enough to leave the succeeding signal pulses unaffected. Otherwise, $U_{\mathrm{So}}^{0\{1\}}$ might become large and thus decrease the FoM. This patterning effect is caused by a large lifetime of cavity mode 2. To confirm the validity of using $U_{\mathrm{So}}^{0\{1\}}$ and $U_{\mathrm{So}}^{1\{0\}}$ to define a figure of merit, we have simulated the case of a pseudo random binary signal (PRBS) [66], consisting of $2^{15}-1$ bits as the input in Eq. (7.2.1). Fig. 7.4(b) shows the output energy registered by the detector as a function of the bit number. The figure also shows the probability distribution function (pdf) of the detected energies. The dashed black lines in Fig. 7.4(b) indicate $U_{\mathrm{So}}^{0\{1\}}$ and $U_{\mathrm{So}}^{1\{0\}}$, and it is observed that they are, in fact, upper and lower bounds on the received energy.

We have solved Eq. (7.2.1) numerically to investigate how the FoM depends on the different parameters describing the system. In all calculations, the peak power of the input signal is $P_{\mathrm{S}}^{0}=10^{-6}\times\epsilon_0 ac/\chi^{(3)}$, which is small enough compared to the pump power to have a negligible effect on the nonlinear frequency shift. The signal and pump pulses have equal widths, $\Delta t_{\mathrm{S}}=\Delta t_{\mathrm{P}}=10^{3}\times a/c$, constant phases, $\phi_{\mathrm{S}}^{\mathrm{i}}(t)=\phi_{\mathrm{P}}^{\mathrm{i}}(t)=0$, the delay between them is zero, and the bit rate B is $1/(4\Delta t_{\mathrm{S}})$. The varied parameters are the detunings, the cavity linewidths, and the peak power of the pump pulse P_{P}^{0}. In Section 7.6, we vary the response time of the detector. This is done by varying the pulse width while keeping the bit rate at $1/(4\Delta t_{\mathrm{S}})$ and the number of OTDM channels fixed at 10. This corresponds to a variation of the signal bandwidth, and the energy-bandwidth trade-off is investigated by evaluating the amount of energy, which is required to obtain a certain FoM for each bandwidth.

The parameter values from Ref. [59] are based on a 2D calculation, so the powers and energies used here are in units of W/m and J/m. To compare with real 3D devices, we may assume that the extent of the field in the transverse plane is on the order of a, if the structure is a slab with a thickness of some fraction of a. By choosing $a=0.6$ μm and $\chi^{(3)}=6.5\times10^{-19}$ m^2/V^2, which corresponds to a nonlinear refractive index of $n_2=1.5\times10^{-17}$ m^2/W [34], we have an energy unit of $\epsilon_0 a^2/\chi^{(3)}a=3$ pJ, and a time unit of $10^{3}\times a/c=2$ ps, giving a bit rate of 125 Gbit/s. The value of n_2, we are using is achievable in AlGaAs below half the electronic band gap [59], in which case two photon absorption is negligible.

7.5 Switching Dynamics with Signal and Pump Pulses

First, we consider the case of a fixed linewidth of cavity mode 2, $\Delta\omega_2=2\Omega_{\mathrm{P}}$. The pump energy $U_{\mathrm{P}}^{\mathrm{i}}$ and the linewidth of cavity mode 1 $\Delta\omega_1$ are varied, while the pulse widths of the signal and pump are fixed. For each $\left(U_{\mathrm{P}}^{\mathrm{i}},\Delta\omega_1\right)$, both detunings are varied in order to find the maximum FoM. Fig. 7.5 shows how the FoM depends on δ_{S} and δ_{P} for 4 different values of $\left(U_{\mathrm{P}}^{\mathrm{i}},\Delta\omega_1\right)$. In Fig. 7.5(a), the quasi steady state limit with $\Delta\omega_1/\Omega_{\mathrm{S}}=10$ is shown, while Fig. 7.5(b) gives

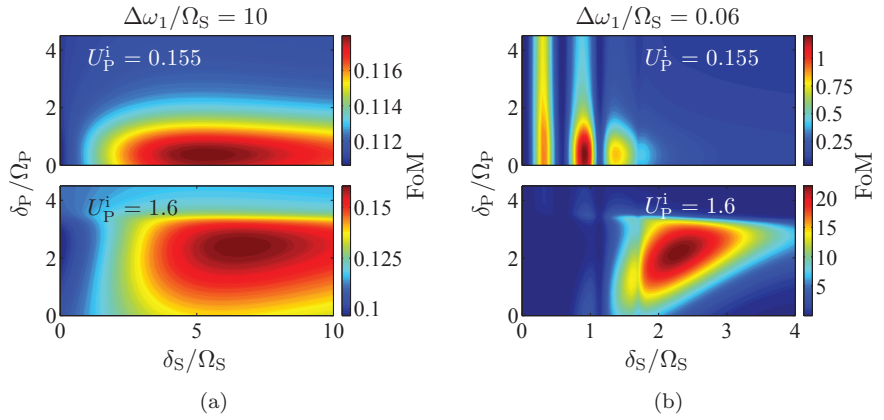

Figure 7.5: (a) Variation of the FoM as a function of the signal detuning δ_S and pump detuning δ_P for $\Delta\omega_1/\Omega_S = 10$ and $\Delta\omega_2/\Omega_P = 2$. The top graph corresponds to a pump energy of $U_P^i = 0.155 \times \epsilon_0 a^2/\chi^{(3)}$, while the bottom graph corresponds to $U_P^i = 1.6 \times \epsilon_0 a^2/\chi^{(3)}$. (b) Same as (a), except the linewidth of mode 1 is $\Delta\omega_1/\Omega_S = 0.06$.

the dependence in the short pulse regime with $\Delta\omega_1/\Omega_S = 0.06$. Generally, the maximum FoM occurs at a larger δ_S when the pump energy is increased. A large pump energy provides a large nonlinear frequency shift of cavity mode 1, which in combination with a large signal detuning results in a large change in the signal transmission. This is the reason that the FoM may be increased by using a larger pump energy. Fig. 7.5(b) also shows that there is a large qualitative difference in the dependence of the FoM on the detunings in the quasi steady state and short pulse regimes. This is expected from the results in Section 7.3. The presence of multiple extrema in the FoM as a function of δ_S in Fig. 7.5(b) is caused by the same effect as the one discussed in relation to the appearance of local extrema in Fig. 7.2(b). Here, we have varied the detuning instead of the power as in Fig. 7.2(b), but it is still the oscillations in the output power that causes the extrema. A local extremum occurs for values of δ_S, where the fixed pump power causes the effective oscillation period to change by $\sim$4 times the pulse width.

Another important observation, which can be made from Fig. 7.5, is that the FoM is much larger in the short pulse regime than in the quasi steady state case. In the upper panel of Fig. 7.6(a) we show the maximum FoM found by varying the detunings as a function of U_P^i and $\Delta\omega_1$. The increase in FoM with decreasing cavity linewidth is also seen there. It is noted that FoM < 1 is possible, although not practically acceptable, since the energy in the denominator of Eq. (7.4.1) is an integral over 9 pulses, whereas the numerator results from an integration over a single pulse. The price to pay for the increase in the FoM is a reduction in transmission, $U_{So}^{1\{0\}}/U_{Si}^{1\{0\}}$, which is illustrated in the lower

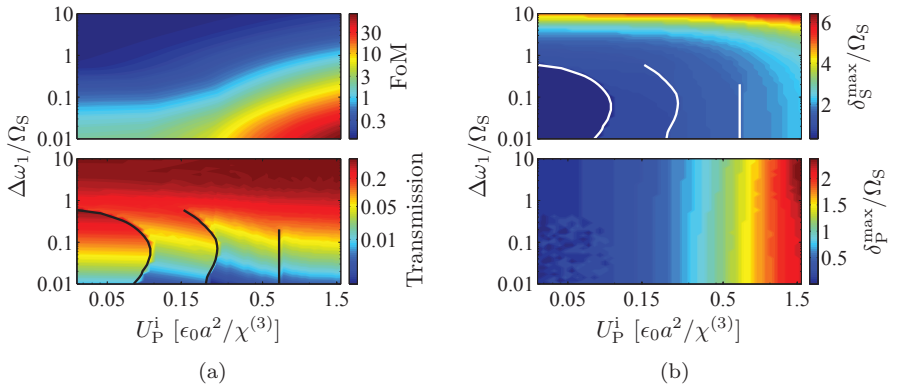

Figure 7.6: (a) Upper panel: The maximum of the FoM found by varying (δ_S, δ_P) as a function of U_P^i and $\Delta\omega_1$. (a) Lower panel: The transmission of the signal pulse, $U_{So}^{1\{0\}}/U_{Si}^{1\{0\}}$, corresponding to the maximum of the FoM in the upper panel. The black lines indicate discontinuity boundaries, where the transmission suddenly changes value. (b) Upper panel: The value of δ_S^{max}/Ω_S corresponding to the maximum of the FoM. The white lines indicate discontinuity boundaries. (b) Lower panel: The value of δ_P^{max}/Ω_P, which corresponds to the maximum of the FoM.

panel of Fig. 7.6(a). The discontinuities in the transmission occur when the global maximum of the FoM shifts from one local maximum to another in the (δ_S, δ_P)-plane, cf. Fig. 7.5(b). The value of the signal detuning, where the maximum in the FoM occurs, δ_S^{max}, is plotted in the upper panel of Fig. 7.6(b) and the discontinuity boundaries are indicated by the white lines. The lower panel of Fig. 7.6(b) shows δ_P^{max} and it is observed to depend much stronger on U_P^i than $\Delta\omega_1$. Since the signal power is too small to shift the resonance frequency of cavity mode 2, it makes sense that $\Delta\omega_1$ does not have a significant influence on δ_P^{max}. The maximum in the pump detuning increases with increasing pump energy because a larger power causes a larger shift of ω_2, and in order to get a maximum amount of power in the cavity, δ_P^{max} must also increase.

Many of the tendencies observed in Figs. 7.6(a) and 7.6(b) may be understood from the solution of Eq. (7.2.1a) in the linear limit. For a single Gaussian input pulse, the output energy is given by

$$U_S^o = P_S^0 \Delta t_S \frac{\pi}{4} X e^{\ln(2)(X-i2Y)^2} \left(\mathrm{Erfc}\left[\sqrt{\ln(2)}(X - i2Y)\right] + e^{i8\ln(2)XY} \mathrm{Erfc}\left[\sqrt{\ln(2)}(X + i2Y)\right] \right), \quad (7.5.1)$$

where

$$X = \frac{\Delta\omega_1}{\Omega_S}, \quad Y = \frac{\delta_S}{\Omega_S}, \quad \text{and} \quad \mathrm{Erfc}(z) = 1 - \frac{2}{\sqrt{\pi}} \int_0^z e^{-t^2} dt.$$

The switching contrast of a single pulse is defined as

$$C_{\text{switch}} = \frac{U_{\text{So}}^{\text{on}}}{U_{\text{So}}^{\text{off}}}, \tag{7.5.2}$$

where $U_{\text{So}}^{\text{on}}$ and $U_{\text{So}}^{\text{off}}$ are the output energy of the signal in the "on" and "off" state of the switch. Since the primary switching mechanism is a shift of the cavity resonance, we may define a switching contrast in the linear regime by $U_{\text{S}}^{\text{o}}(\delta_{\text{S}} + \delta_{\text{NL}})/U_{\text{S}}^{\text{o}}(\delta_{\text{S}})$. The change in detuning δ_{NL} is induced by the presence of the pump as seen in Eq. (7.2.1a). For small shifts, this expression may be expanded in δ_{NL} as

$$\frac{U_{\text{S}}^{\text{o}}(\delta_{\text{S}} + \delta_{\text{NL}})}{U_{\text{S}}^{\text{o}}(\delta_{\text{S}})} \approx 1 + \frac{\partial U_{\text{S}}^{\text{o}}}{\partial \delta_{\text{S}}} \frac{1}{U_{\text{S}}^{\text{o}}} \delta_{\text{NL}}. \tag{7.5.3}$$

It is therefore expected that the signal detuning resulting in a maximum contrast is found close to where the relative change of U_{S}^{o} as a function of δ_{S} has a maximum. We define this relative change in the normalized units of Eq. (7.5.1) as

$$\partial U_{\text{S}}^{\text{o}}(\delta_{\text{S}}/\Omega_{\text{S}}) = \left| \frac{\partial U_{\text{S}}^{\text{o}}(\delta_{\text{S}}/\Omega_{\text{S}})}{\partial(\delta_{\text{S}}/\Omega_{\text{S}})} \right| \frac{1}{U_{\text{S}}^{\text{o}}(\delta_{\text{S}}/\Omega_{\text{S}})}. \tag{7.5.4}$$

In Fig. 7.7(a) the dependence of the maximum of $\partial U_{\text{S}}^{\text{o}}(\delta_{\text{S}}/\Omega_{\text{S}})$ on $\Delta\omega_1/\Omega_{\text{S}}$ is shown. The observed increase in $\max\{\partial U_{\text{S}}^{\text{o}}\}$ as $\Delta\omega_1$ is decreased thus explains

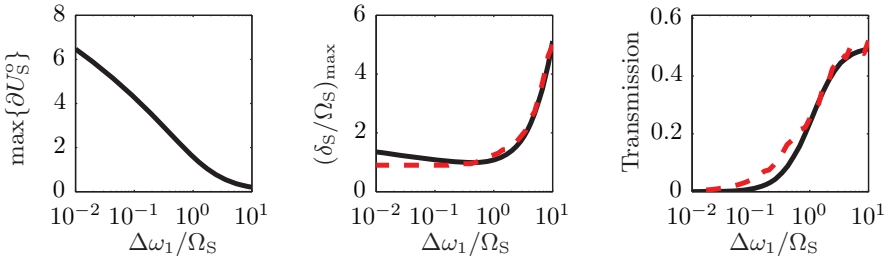

Figure 7.7: (a) The maximum value of $\partial U_{\text{S}}^{\text{o}}(\delta_{\text{S}}/\Omega_{\text{S}})$, defined in Eq. (7.5.4), plotted as a function of the ratio between the cavity linewidth and the pulse bandwidth. (b) The value of $\delta_{\text{S}}/\Omega_{\text{S}}$ corresponding to the maximum in (a) (solid black) and a cross section of $\delta_{\text{S}}^{\max}/\Omega_{\text{S}}$ at $U_{\text{P}}^{\text{i}} = 0.105 \times \epsilon_0 a^2/\chi^{(3)}$ from Fig. 7.6(a) (dashed red). (c) Transmission at the maximum in (a) (solid black) and a cross section of the transmission at $U_{\text{P}}^{\text{i}} = 0.105 \times \epsilon_0 a^2/\chi^{(3)}$ from Fig. 7.6(a) (dashed red).

why the FoM also increases when $\Delta\omega_1$ is decreased, as it is seen in Fig. 7.6(a). Another way of understanding this behavior in the short pulse regime, is to consider the transient oscillations resulting from a step function input given

in Eq. (7.3.1). As $\Delta\omega_1$ is decreased, the ratio between the maxima and minima of the oscillations as well as the cavity lifetime increase, which causes a larger difference in the output energy between the upper and lower panels in Fig. 7.2(a). This means that the change in output energy, due to the presence of the pump pulse, increases as $\Delta\omega_1$ is decreased.

Fig. 7.7(b) shows the value of δ_S/Ω_S, where the maximum in ∂U_S^o occurs (solid black curve) and a cross section of δ_S^{max}/Ω_S from Fig. 7.6(a) at $U_P^i = 0.105\times\epsilon_0 a^2/\chi^{(3)}$ (dashed red curve). The agreement between the curves is seen to be good for large values of $\Delta\omega_1$, but there is a discrepancy when the cavity linewidth decreases. This is also the case for the transmission corresponding to the maximum of ∂U_S^o, which is plotted in Fig. 7.7(c) (solid black curve) along with a cross section of the signal transmission, $U_{So}^{1\{0\}}/U_{Si}^{1\{0\}}$, at $U_P^i = 0.105\times\epsilon_0 a^2/\chi^{(3)}$ from Fig. 7.6(a) (dashed red curve). The reason for this discrepancy is that the denominator in Eq. (7.4.1) is an integration over 9 bits. When $\Delta\omega_1$ decreases, the signal energy in one bit does not escape the cavity before the next pulse arrives. This gives rise to a much more complicated behavior, which cannot be accounted for by an analysis based on a single pulse. The discontinuities in Fig. 7.6 are not described by the linear analysis either. These can only be understood as an interplay between the nonlinear frequency shift and the transient oscillations of the output pulses observed in Fig. 7.3. This conclusion is supported by the fact that the discontinuities appear in the short pulse regime, where the oscillations were observed in Fig. 7.3. Even though the linear analysis is not able to describe all the details of Fig. 7.6, it is still very useful for understanding the general trends.

From Figs. 7.6 and 7.7 we have learned that decreasing the linewidth of cavity mode 1 provides a large figure of merit, but at the cost of a reduction in transmission. Here, we will use a lower bound on the transmission of 0.1, corresponding to a cavity linewidth of $\Delta\omega_1 \sim\Omega_S/3$, or equivalently, a quality factor of, $Q_S \sim$2500. Fig. 7.6(a) also shows that to achieve a figure of merit well above 1 with this cavity linewidth, a larger pump energy must be applied.

Using a fixed value of $\Delta\omega_1 = \Omega_S/3$, we now vary the pump energy and the linewidth of cavity mode 2 in the same way as in Fig. 7.6. The results are shown in Fig. 7.8. From the upper panel in Fig. 7.8(a) it is observed that there is an optimum value of $\Delta\omega_2$, which minimizes the required pump energy to achieve a certain value of the figure of merit. If the cavity linewidth is large, the field enhancement inside the cavity is small, and thus, it requires a larger input power to achieve a certain frequency shift. On the other hand, if the linewidth becomes smaller, the figure of merit is reduced by patterning effects as mentioned in Section 7.4. The lower panel in Fig. 7.8(a) shows the dependence of the signal transmission, $U_{So}^{1\{0\}}/U_{Si}^{1\{0\}}$. Like in Fig. 7.6(a), a discontinuity is also observed here and is indicated with a white curve. Again, it is caused by the global maximum of the FoM shifting from one local maximum to another in the $(\delta_S,\ \delta_P)$-plane.

The values of detuning, which correspond to the maximum in the FoM, are depicted in Fig. 7.8(b). It is clearly seen from these graphs that the disconti-

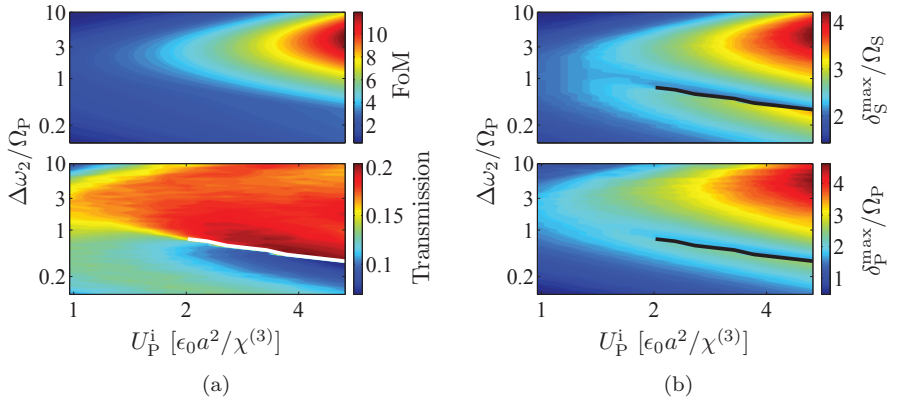

Figure 7.8: (a) Upper panel: The maximum FoM found by varying (δ_S, δ_P) as a function of U_P^i and $\Delta\omega_2$. (a) Lower panel: The transmission of the signal, $U_{So}^{1\{0\}}/U_{Si}^{1\{0\}}$, corresponding to the maximum of the FoM in the upper panel. As in Fig. 7.6(a), the white line indicates a discontinuity boundary, where the transmission suddenly changes value. (b) Upper panel: The value of δ_S^{max}/Ω_S corresponding to the maximum of the FoM. The discontinuity boundary is also shown with a black line. (b) Lower panel: The value of δ_P^{max}/Ω_P, which corresponds to the maximum of the FoM along with the discontinuity boundary.

nuity in Fig. 7.8(a) corresponds to a discontinuous change in δ_S^{max} and δ_P^{max}. By comparing Figs. 7.8(a) and 7.8(b) it is observed that the maximum in the FoM is coincident with a maximum in δ_S^{max}. This makes sense because the difference between the numerator and denominator in Eq. (7.4.1) can be made larger by using a larger detuning if sufficient pump power is available to cause a correspondingly large frequency shift. From the lower panel in Fig. 7.8(b) it is observed that the behavior of δ_P^{max} closely resembles that of δ_S^{max}. It is to be expected that δ_P^{max} is the value of δ_P, where a maximum amount of pump power is available to shift the resonance frequency of cavity mode 1. This is the reason for the increase in δ_P^{max} with U_P^i, because the shift of ω_2 also increases with pump power.

7.6 Energy-Bandwidth Trade-Off

From Fig. 7.8(a), it was learned that there is an optimum ratio between the linewidth of cavity mode 2 and the pulse bandwidth, which results in a minimum in the pump energy required to achieve a given value of the FoM. To quantify the energy-bandwidth trade-off, we now vary the linewidth $\Delta\omega_2$ and pump energy as in Fig. 7.8(a) for different values of the two pulse widths, $\Delta t_S = \Delta t_P$. The bit rate is still given by $1/(4\Delta t)$, so this allows us to investi-

gate the dependence of the minimum required pump energy on the bit rate of the signal. We keep the ratio $\Delta\omega_1/\Omega_S$ fixed at 1/3 to get sufficient transmission, cf. Section 7.5. The result is shown in Fig. 7.9(a). The different curves correspond to the minimum energy required to achieve different values of the FoM. It is clearly observed how the energy requirement increases as the bit

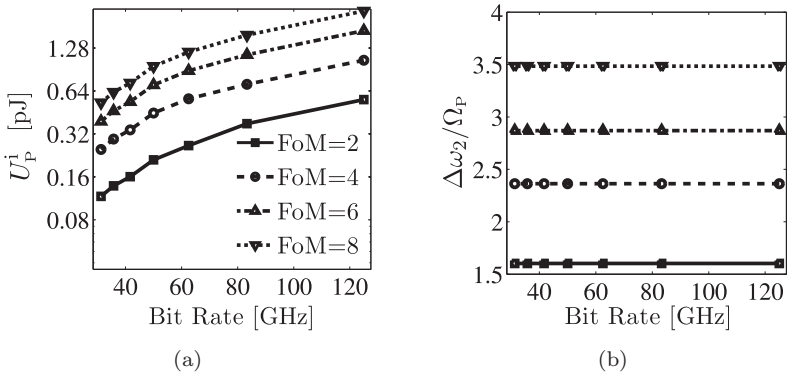

Figure 7.9: (a) Minimum required pump energy to obtain different values of the FoM (indicated by the different curves) as a function of the signal bit rate. (b) The ratio of the linewidth of cavity mode 2 and the pulse spectral width corresponding to the minimum energies shown in (a). The different curves correspond to the same values of the FoM as in (a). In both (a) and (b), the parameter values from Section 7.4 have been used.

rate increases, and as the value of the FoM increases. Fig. 7.9(b) shows the optimum ratio, $\Delta\omega_2/\Omega_P$, corresponding to the minimum in U_P^i. The different curves correspond to the same values of the FoM as in Fig. 7.9(a). The optimum ratio is seen to be independent of the bit rate, but increases as the value of the FoM is increased. Since the bit rate is varied by changing Ω_P, we see that the optimum linewidth of cavity mode 2 changes, corresponding to a quality factor of $Q_2 \approx 900$ for $B = 40$ GHz and $Q_2 \approx 300$ for $B = 125$ GHz, when $\Delta\omega_2/\Omega_P \approx 3$. For a bit rate of 125 GHz, the quality factors of the two modes, Q_1 and Q_2, differ by a factor of 9. Such a large difference is easy to achieve in a structure with spatially separated waveguides, cf. Chapter 6, suggesting that such structures are advantageous when operating at high bit rates.

8

Energy Reduction by using Fano Resonances

8.1 Introduction

The waveguide-cavity structures considered so far, have Lorentzian transmission spectra characterized by $|t_1| = 0$ in Eq. (2.2.19). The Lorentzian function falls off as $1/\delta_S^2$, where δ_S is the detuning of the signal from the cavity resonance. If it was possible to design a filter with sharper transmission features, the required detuning for a certain switching contrast would be reduced, leading to a reduction in the energy consumption. In this chapter we shall investigate the use of so-called Fano resonances [69] to improve the performance of photonic crystal (PC) waveguide-cavity structures. The work is contained in Ref. [70]. Fano resonances appear in a range of physical systems due to interference effects between discrete- and continuous level systems [69]. Thus, waveguide-cavity structures, where the continuous modes of the waveguide couple to the discrete modes of the cavity, is a natural candidate for observing such resonances. It has been shown both theoretically [40,71,72] and experimentally [73,74] that sharp asymmetric transmission features can be obtained by introducing defects into the waveguide-cavity system. In all these examples, the defect is characterized by at least two degrees of freedom: Resonant wavelength and quality factor for double-cavities [71, 73], and transmittance and mirror distance for waveguide defects [40,74]. A single defect system has been studied theoretically for a coupled resonator optical waveguide structure [75], and we shall adopt a similar approach in a the line-defect waveguide system. In Section 8.2 it is discussed how to realize Fano resonances in a simple way, which is expected to make the fabrication easier than the above examples of structures with two degrees of freedom. Then, in Section 8.3, it is analyzed using temporal coupled mode theory (TCMT), how such designs may improve the device performance. To provide a validation of the developed design concept, we end the chapter with

a few examples of real devices that have been fabricated and characterized by Yi Yu based on these designs.

8.2 Structure Design

The idea for the design presented in this section originates in the formulation of the TCMT equations in Section 2.2.1, where scattering directly between the ports is included in a general way. If a scattering element is introduced in the waveguide with a transmittance in the range $|t_1| \in [0;1]$, it is seen from Eq. (2.2.19) that a family of transmission curves arise, which spans from the configurations normally denoted "in-line" ($|t_1| = 0$) and "side-coupled" ($|t_1| = 1$) [13]. This is illustrated in Fig. 8.1, where the continuous wave (CW) transmission from Eq. (2.2.19) is plotted at different values of the waveguide transmittance for a cavity, which is odd with respect to reflections in the plane $x = 0$. It is observed that $|t_1| = 0$ gives rise to the well-known Lorentzian

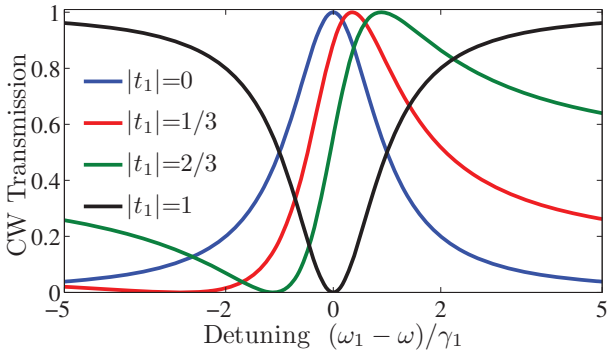

Figure 8.1: Plot of Eq. (2.2.19) for different values of the transmittance between the two ports for an odd cavity mode. The ouf-of-plane Q is assumed infinite, so $\gamma_1/\gamma_C = 1$.

resonance from Fig. 4.5. For intermediate values of the transmittance, it is seen that the CW transmission exhibits both a maximum and minimum. The incoming light may pass through the structure via two different paths: Either coupling to the cavity or by simple transmission through the waveguide blockade. Light traveling through the different paths may interfere constructively (destructively) leading to a transmission maximum (minimum).

The design idea simply consists of reducing the number and possibly the size of the holes separating port 1 and 2 in Fig. 4.4, which is expected to yield values of $|t_1|$ ranging from zero to one. The switching scheme of primary interest is for the pump to change the state of the switch from "off" to "on". This is, in principle, more difficult to achieve than the "on" to "off" scheme, because nonlinear absorption will increase the switching contrast, while decreasing it

in the "off" to "on" scheme. For an asymmetric filter transmission, it is important to consider the intended scheme. A nonlinearity dominated by free carrier dispersion (FCD) will increase the resonance frequency, whereas a Kerr nonlinearity will decrease it. Remembering that the detuning is defined as the difference between the frequency of the resonance and the input $\delta_1 = \omega_1 - \omega$, it is noted that an FCD nonlinearity will increase the detuning. From Fig. 8.1 it is observed that the sharp transmission feature may be utilized in an "off" to "on" scheme by having a signal frequency larger than the resonance $\delta_1 < 0$ and relying on FCD to shift the eigenfrequency. From Section 2.2.1 and Fig. 8.1 it therefore follows that the cavity resonance must be odd with respect to reflections in the mirror-plane $x = 0$. Fig. 4.1(b) shows that the H0 cavity is even, and therefore not suited for this design. Furthermore, if the Fano resonance design should be implemented in a four port structure, the cavity must be multi-mode. The already familiar H1 cavity then seems like a natural choice. Due to the smaller mode volume of the dipole modes [61], they will be considered for the design.

In Fig. 8.2(a) the basic design of the cavity is shown along with an illustration of the hole shifts used to split the degeneracy of the dipole modes. The symmetry of the hole shifts is rotated compared to Fig. 6.1(a) to reflect the intended rectangular symmetry of the structure. The notation and color convention is the same as in Section 6.2, such that the red circles indicate holes, which primarily influence the frequency of mode 1 and blue circles indicate holes that primarily affect mode 2. Fig. 8.3 shows the modes, and as in Section 6.2, the mode distributions are used to decide, which holes to shift for a maximum impact on the resonance frequencies. From Fig. 8.3(a) it is observed that mode 1 has the desired odd symmetry. In Section 6.2 the pump and signal could, in principle, be coupled into either of the waveguides. Here, however, waveguide 1 is designated for the signal and must be designed to couple to mode 1 only. Fig. 8.2(b) shows the location of WG1 relative to the cavity as well as the hole shifts that are introduced to ensure an appropriate coupling to the cavity. A hole is introduced in the waveguide to act as a partial blockade as discussed above.

It should be noted from Fig. 8.2(a) that the central hole of the cavity is not removed, but has a reduced radius. This violates our previous design rule of a single hole size. Keeping the hole is not strictly necessary for the design, but it serves two important purposes: The first is to increase the area for surface recombination close to the peak of the optical energy distribution. The relaxation of the carriers back to the ground state is therefore expected to be faster, which increases the overall operation speed of the switch. The second purpose is to increase the out-of-plane quality factor of the structure, which was observed to increase by introducing the central hole in finite difference time domain (FDTD) simulations.

Using the methods described in Appendix B, the eigenmode and transmission spectrum of the structure in Fig. 8.2(b) is found. Fig. 8.4 shows the

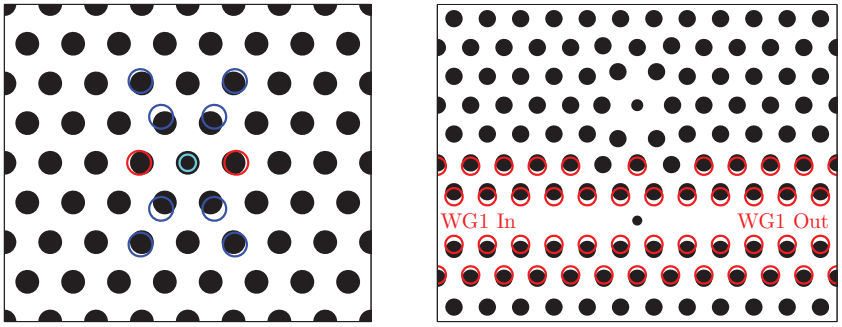

(a) (b)

Figure 8.2: Top view of the cavity design and the waveguide intended for the signal. The radii of holes in the lattice are $r_0 = 0.26a$ and the membrane thickness is $d = 0.8a$. (a) The indexing of the hole shifts follows the convention from Fig. 6.1(a) and the values are: $l_{11c} = 0.06a$, (red), $l_{21c} = 0.16a$, and $l_{22c} = 0.08a$ (blue). The central hole has a reduced radius $r_C = 0.18a$. (b) A zoom-out showing the cavity as well as waveguide 1. The holes surrounding WG1 are shifted by $l_{11p} = 0.15a$ and $l_{12p} = 0.10a$. Only the holes indicated by red circles are shifted, such that shifts of the cavity holes take precedence over shifts of the waveguide holes. The waveguide contains a blockade hole with radius $r_b = 0.15a$.

eigenmode of the magnetic field, and Fig. 8.5 depicts the transmission spectrum. The transmission spectrum in Fig. 8.5(a) (blue curve) shows sharp transmission features similar to Fig. 8.1 as expected. The peak transmission is observed to be close to the waveguide transmission (red curve), and the transmission dip is close to zero. This is a clear indication that $\gamma_1/\gamma_C \approx 1$, which is promising for the device performance. The black curve in Fig. 8.5 shows the transmission of a structure without the cavity, which should provide information about the blockade transmittance. It is seen to vary considerably in the frequency range of the resonance. However, from Fig. 8.5(b) it shows a clear oscillatory behavior consistent with Fabry-Perot fringes due to reflections from the interfaces between the PC and strip waveguides (see Fig. 8.4). The frequency spacing of the fringes for this particular structure should be given by $\Delta\omega = (1/60n_g)2\pi c/a$, where 60 is two times the interface distance in units of a and n_g is the group index. From Fig. 8.5(b) this corresponds to a group index of about 20 close to the waveguide band gap edge at $\omega = 0.276 \times 2\pi c/a$ and 3.1 at $\omega = 0.29 \times 2\pi c/a$, which is reasonable. The large variation observed in Fig. 8.5 is therefore not expected to be a property of the blockade hole itself, although it is expected to have some smaller frequency dependence.

The next step is to implement the Fano resonance in a four port structure

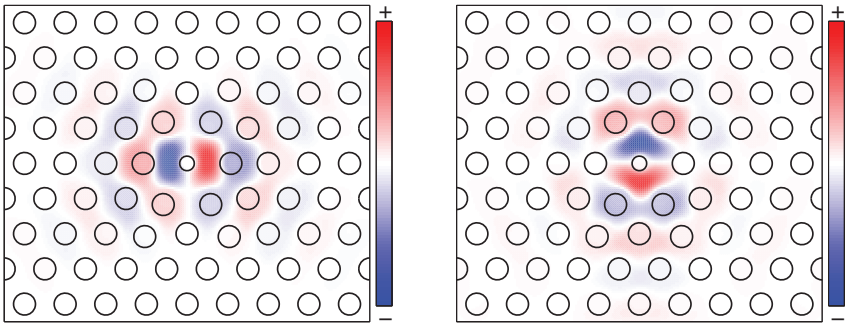

Figure 8.3: Dipole modes ($\mathrm{Re}\{H_z\}$) of the cavity structure described in Fig. 8.2(a). (a) Mode 1 (M1), which is odd and is therefore designated to couple to the signal to benefit from the sharp transmission features as discussed above. (b) Mode 2, which is even and couples to WG2, which is designated for the pump.

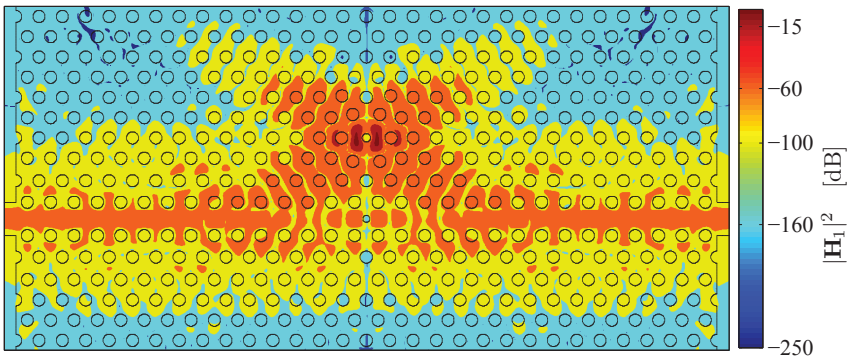

Figure 8.4: Eigenmode of the Fano resonance structure. A normalization is used, so the maximum value of $|\mathbf{H}_1|^2 = 1$ and the logarithmic scale clearly shows the field enhancement inside the cavity as well as the confinement within the waveguide. The contours in the figure correspond to the values on the axis of the colorbar.

to achieve the advantages discussed in Chapter 6. The second waveguide is placed above the cavity and running in parallel to WG1. The design is illustrated in Fig. 8.6. From Eq. (2.2.21) it is seen that the cavity energy does not depend on the direct scattering between the waveguides. Therefore, the important design parameter is the cavity-waveguide coupling rate γ_2. The blockade configuration is chosen such that $|t_2| = 0$ and the pump is transmitted on resonance. The number of blockade holes is chosen to achieve a total quality factor

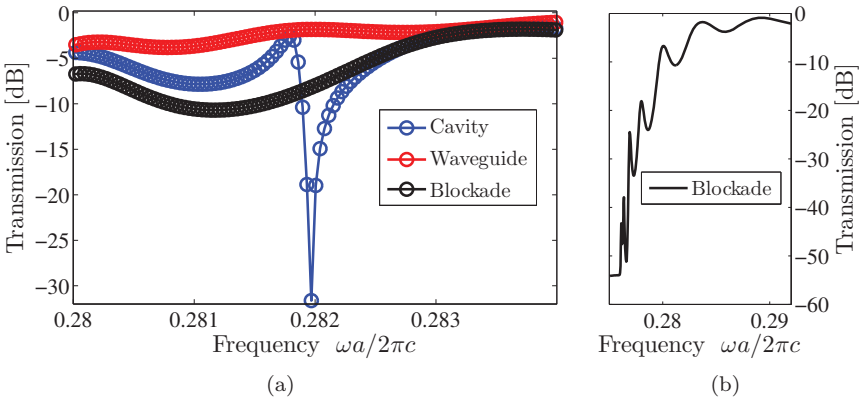

Figure 8.5: Transmission spectra found from FDTD simulations corresponding to the structure in Fig. 8.2(b). (a) The blue curve shows the spectrum of the full structure, the red curve corresponds to the waveguide alone without the blockade hole, and the black curve to the waveguide including the blockade. (b) Blockade transmission shown in a larger frequency range to illustrate the oscillatory behavior.

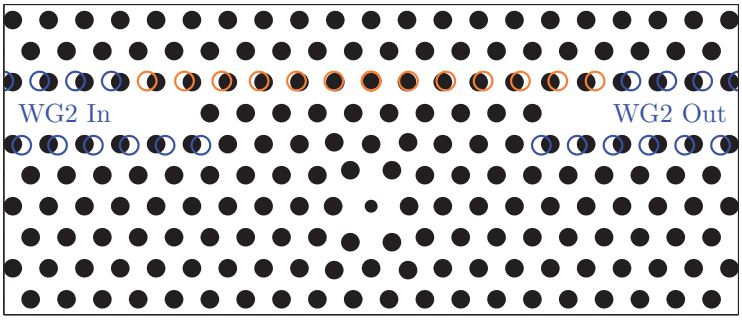

Figure 8.6: Design details of waveguide 2 for the four port Fano structure. Only the first row of holes is shifted by $l_{21h} = 0.25a$ and $l_{21p} = -0.03a$. To avoid any additional cavity formation near $x = 0$, the orange holes are shifted gradually in the horizontal direction between 0 and l_{21h} in steps of $l_{21h}/6a$.

Q_2 of a few thousand. Again, the design is chosen to have a mirror-plane at $x = 0$. Since the holes of WG2 are shifted longitudinally, additional cavities may form close to the $x = 0$ plane, which complicates the design unnecessarily. To avoid this, the holes of the upper row are shifted gradually as indicated by the orange circles in Fig. 8.6.

The entire structure along with the two eigenmodes are shown in Figs. 8.7 and 8.8. The region of strong field enhancement is seen to be localized to the

cavity indicating that the gradual shift of holes in WG2 works as intended. Furthermore, from the logarithmic scale, it is clearly seen that each mode

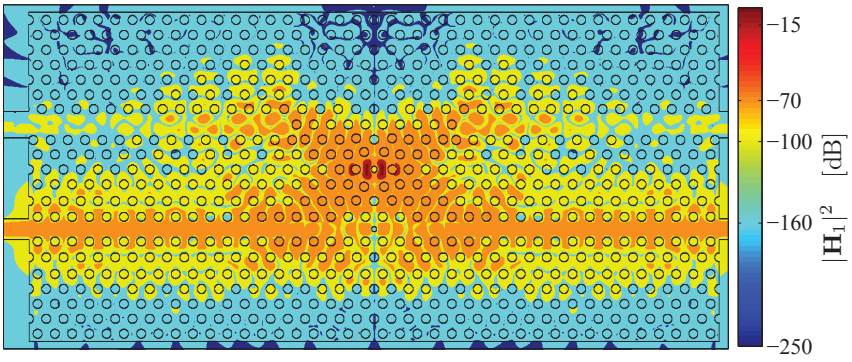

Figure 8.7: Mode 1 (M1) of the four port structure with a Fano resonance in the signal transmission. The peak value is normalized to 1 and the shown contours match the numbers on the colorbar. From the mode distribution, it is clearly seen that mode 1 only couples to WG1.

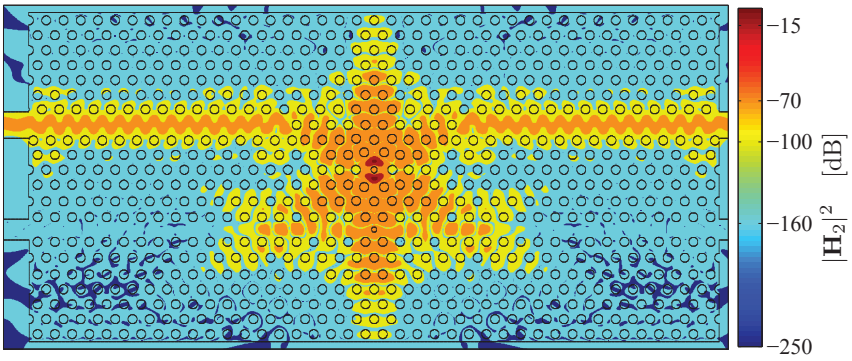

Figure 8.8: Mode 2 (M2) of the four port structure with a Fano resonance in the signal transmission. The peak value is normalized to 1 and the shown contours match the numbers on the colorbar. From the mode distribution, it is clearly seen that mode 2 only couples to WG2.

only couples to its respective waveguide. As in Fig. 6.6, the output power in the two waveguides after the transient time of the source was monitored, and we find $P_2^o/P_1^o = -19.5$dB with an input in WG1, and $P_1^o/P_2^o = -27.7$dB with an input in WG2. This is a small cross-talk for a very small device footprint. The mechanism behind the elimination of cross-talk is illustrated in Fig. 8.9, which shows the transmission properties of the structure. The red

and blue curves show the transmission around the resonance of mode 1 and 2, respectively. The dashed curves show the cross-talk transmission, and the ratios between the solid and dashed lines correspond well with the numbers found from monitoring the power output in time. The green and black curves show the transmission through waveguides 1 and 2. It is clearly seen how the band

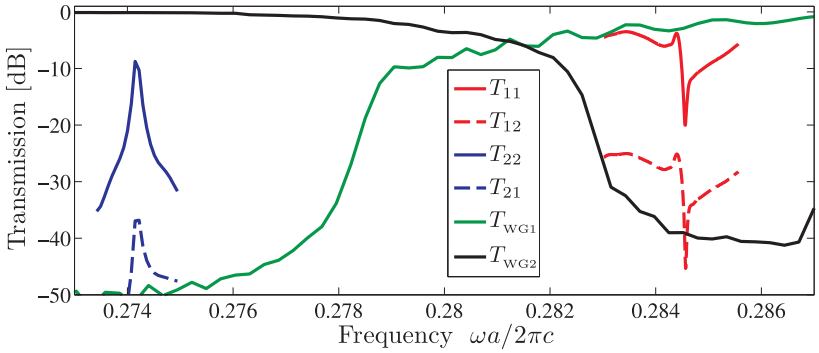

Figure 8.9: Transmission spectra of the structure in Figs. 8.7 and 8.8 found from FDTD simulations. The resonance frequencies are $\omega_1 = 0.2845 \times 2\pi c/a$, $\omega_2 = 0.2742 \times 2\pi c/a$, and the quality factors are $Q_1 = 3300$ and $Q_2 = 3400$.

gaps of the waveguides are designed to coincide with the resonance intended to couple only to the other waveguide. The design is intended for a wafer with a thickness of 340nm. This means that the lattice constant would be 340/0.77nm = 441.6nm, and the resonance wavelengths $\lambda_1 = 441.6\text{nm}/0.2845 = 1552\text{nm}$, and $\lambda_2 = 441.6\text{nm}/0.2742 = 1610\text{nm}$. It is noted that the peak transmission of mode 2 is relatively small. From a study of the unloaded quality factors of the two modes, they appear to be similar. The absence of a higher peak is partly due to the frequency resolution of the FDTD simulation, but this alone cannot account for the low peak. The switching energy is only related to the waveguide-cavity coupling of the pump, so the low peak transmission of mode 2 does not affect the device performance. However, the mechanism behind it should be investigated further.

8.3 TCMT Analysis

From Figs. 8.1 and 8.5 of the previous section, there is a clear indication that the TCMT may be used to describe the linear transmission properties of the Fano devices. In order to use the TCMT to investigate the system behavior and optimize parameters, it is necessary to carry out a quantitative comparison with results obtained from FDTD. In Fig. 8.10(b) the transmission spectra obtained with FDTD are fitted using Eq. (2.2.19) for the different blockade configurations in Fig. 8.10(a), and the agreement is good. It should be noted

that the frequency dependence of $|t_1|$ found from FDTD (see Fig. 8.5) was included in Eq. (2.2.19) to obtain a better agreement. From Fig. 8.10(b) it

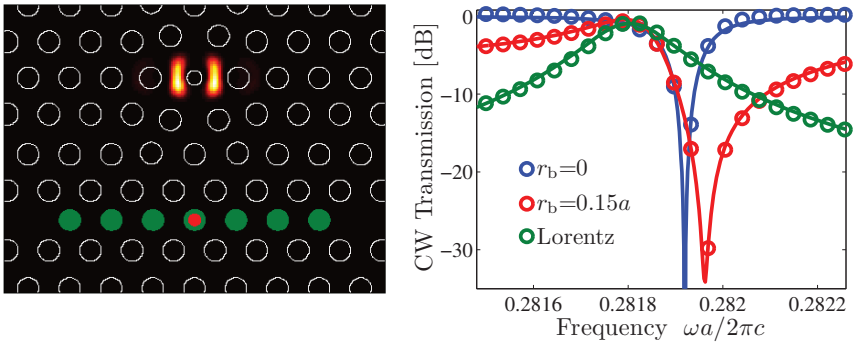

Figure 8.10: Comparison of FDTD and TCMT. (a) A structure with the same parameters as in Fig. 8.2. A blockade hole configuration of a Lorentzian resonance (green) and Fano resonance (red) are shown as well as the odd cavity mode $|\mathbf{H}_1|^2$. (b) Transmission spectra found from FDTD calculations (circles) for the different blockade configurations in (a). The blue curve corresponds to an empty waveguide, and the red and green curves match the colors in (a). The solid lines are fits using Eq. (2.2.19). The eigenfrequencies and Q factors are: Blue: $\omega_1 = 0.28192 \times 2\pi c/a$ and $Q = 2350$. Red: $\omega_1 = 0.28184 \times 2\pi c/a$ and $Q = 1740$. Green: $\omega_1 = 0.28180 \times 2\pi c/a$ and $Q = 1440$.

is noted that the total quality factor varies significantly between the design configurations. Since the maximum transmission approaches unity, the total Q must be dominated by the cavity-waveguide coupling. The coupling in the case of an empty waveguide depends critically on the interference between the two optical paths through the system, which was discussed in Section 8.2. Thus, even the introduction of a single hole with reduced radius may significantly change the cavity-waveguide coupling.

The ability of the TCMT to reproduce results from FDTD simulations provides confidence that Eq. (2.2.19) may be used to analyze the behavior of structures exhibiting Fano resonances. Let us begin by studying its properties. Introducing the normalized parameters $X = \delta_1/\gamma_C$ and $Y = \gamma_1/\gamma_C$, Eq. (2.2.19) may be expanded as

$$T_{CW}(X) = \frac{Y^2 + \left(1 - 2Y + X^2\right)|t_1|^2 + 2YX|t_1|\sqrt{1-|t_1|^2}}{X^2 + 1}. \tag{8.3.1}$$

The minimum distance between the maximum and minimum of T_{CW} is found when $|t_1|^2 = Y/2$ and is given by $\Delta X = 2$. For an infinite out-of-plane Q, this means that the transmission may change from zero to unity in just one cavity linewidth $\delta_1 = 2\gamma_C$. In comparison, the transmission of a Lorentzian line

with $|t_1| = 0$ only changes by a factor of 5 when moving one linewidth away from the peak transmission. To investigate the dependence on the coupling rate ratio γ_1/γ_C, we plot the maximum transmission as well as the frequency separation of the extrema of T_{CW} in Figs. 8.11(a) and 8.11(b). As expected,

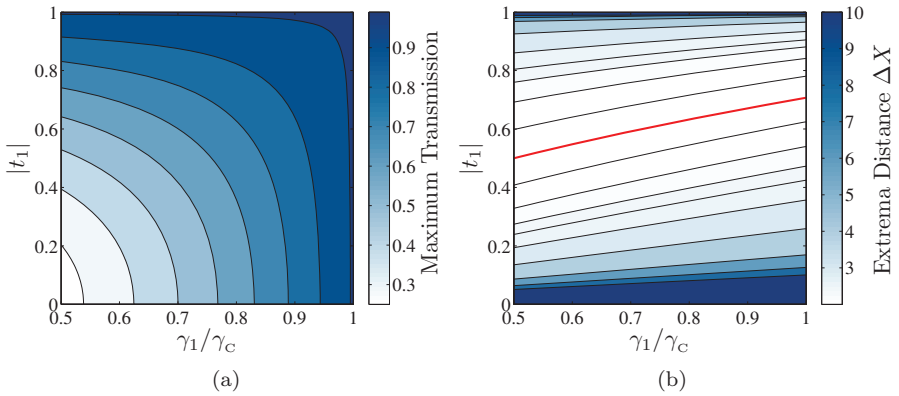

Figure 8.11: Properties of the CW transmission in Eq. (8.3.1). (a) The maximum transmission as a function of coupling rate ratio and the blockade transmittance. (b) The frequency distance between the maximum and minimum transmission. The red line shows the minimum given by $|t_1| = \sqrt{\gamma_1/2\gamma_C}$.

the peak transmission decreases as the proportion of waveguide coupling to out-of-plane scattering is decreased. The ratio Y is related to $Q_\perp$ and Q_1 by $Q_\perp/Q_1 = 1/(1-Y)$, so if $Y = 0.9$ the out-of plane Q factor is ten times larger than Q_1. From Fig. 8.11(a) it is observed that the peak transmission drops significantly even at relatively large coupling ratios. Hence, it is important to optimize $Q_\perp$ in the design process.

The frequency separation in Fig. 8.11(b) diverges as $|t_1|$ approaches the limits 0 or 1, because there is only one extremum in those cases. It is noteworthy that ΔX depends weakly on $|t_1|$ for a quite large range of blockade transmittances. As discussed in Section 4.2, it is preferable from a fabrication point of view to have a single hole size for the entire structure. Since we propose to change the blockade transmittance by varying the radius of the blockade hole, the low sensitivity on $|t_1|$ observed in Fig. 8.11(b) should translate into a low sensitivity on r_b, which is promising for fabrication.

From the CW transmission properties considered above, it is expected that a Fano resonance will yield a larger switching contrast than a Lorentzian line. However, it is important to remember that the switching contrast is defined in terms of the output energy of the signal, cf. Eq. (7.5.2). It is therefore the energy transmission in Eq. (5.2.2), which is relevant when investigating the switching performance of the structure. The energy-bandwidth trade-off discussed in Chapter 7 may be understood from Eq. (5.2.2). In Fig. 8.12(a)

the energy transmission is plotted for a fixed cavity linewidth $\Delta\omega_1$ at different bandwidths Ω_S of a Gaussian input pulse and a Lorentzian resonance. When

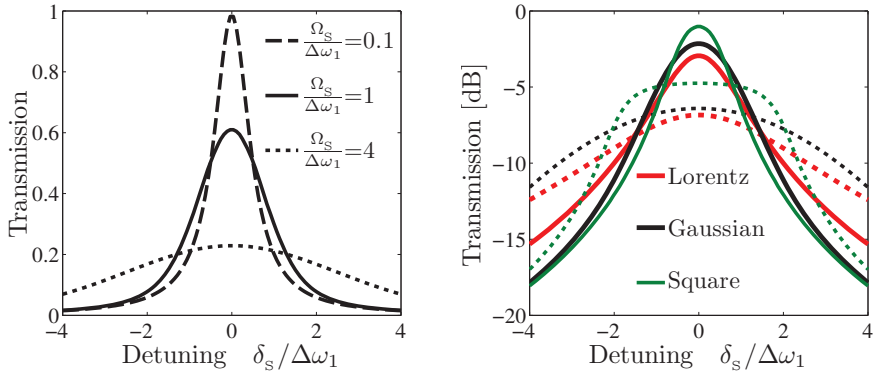

Figure 8.12: (a) Energy transmission for Gaussian pulses with different bandwidths. (b) Energy transmission for pulses with different spectral shapes, but equal bandwidth. The solid and dotted curves correspond to the $\Omega_S/\Delta\omega_1$ ratios in (a).

the signal bandwidth is small compared to the cavity linewidth, $P_S^i(\omega)$ may be approximated by a Dirac delta distribution [76] in Eq. (5.2.2) and the CW transmission is recovered. If the signal bandwidth is comparable to the cavity linewidth, the energy transmission spectrum broadens due to the convolution in Eq. (5.2.2). When the slope of the transmission spectrum is large, it means that a small change in the detuning causes a large change in the transmission and thereby a large switching contrast. From Fig. 8.12(a) it is therefore evident that a large signal bandwidth requires a larger resonance shift to achieve a certain switching contrast, which then requires more energy in the pump pulse.

In Fig. 8.12(b) we re-plot the solid and dotted curves from Fig. 8.12(a) along with transmission spectra for pulses with different spectral shapes but the same bandwidth. Due to the convolution in Eq. (5.2.2), it is expected that a pulse with sharper spectral features will enable an increase in the switching contrast, in the same way that a resonance with sharper features is expected to. Indeed, it is observed that the slope of the transmission spectrum in Fig. 8.12(b) may be increased (decreased) by using pulses with sharper (broader) spectra, such as a square (Lorentzian). It is noted that the optimum operation frequency is different for the different pulse shapes. In Chapter 9 an investigation of optimizing the switching performance by controlling both the amplitude and phase properties of the input pulses is carried out.

In Chapter 7 it was discussed how a figure of merit must be defined to evaluate the performance of switching structures. Here, we will only consider

the switching contrast of a single pulse from Eq. (7.5.2), which does not take patterning effects into account. Our aim is to investigate the possible advantages of using Fano resonances compared to the more conventional Lorentzian lines. So, the question is: For a given signal bandwidth, how should the cavity properties $|t_1|$ and $\Delta\omega_1$ be chosen to minimize the switching energy? The signal bandwidth sets the time- and frequency scale of the problem, and thus, all times and frequencies should be given relative to Ω_S. To quantify the switching performance of the structure, some requirements must be imposed on the "on" and "off" state transmission levels T_U^{on} and T_U^{off}, corresponding to the pump being present or not. As an example, we choose lower limits on the "on" state transmission $T_U^{on} \geq 0.7$ and switching contrast $T_U^{on}/T_U^{off} \geq 12$dB and use Gaussian pulses.

Under the assumption that the nonlinear effect caused by the pump pulse simply frequency shifts the linear transmission spectrum, Eqs. (2.2.19) and (5.2.2) contain important information about the maximum achievable switching contrast at any given signal detuning δ_S. To see this, we first note that the resonance changes dynamically during the passage of the signal in the nonlinear case. The maximum transmission is found when the detuning δ_S and the nonlinear resonance shift δ_{NL} equal zero at all times, so the transmission in the nonlinear case is always smaller than in this case. Let us first investigate how the maximum transmission and switching contrast depends on the blockade transmittance and resonance linewidth. This is depicted in Figs. 8.13(a) and 8.13(b). The red lines indicate contours corresponding to our device re-

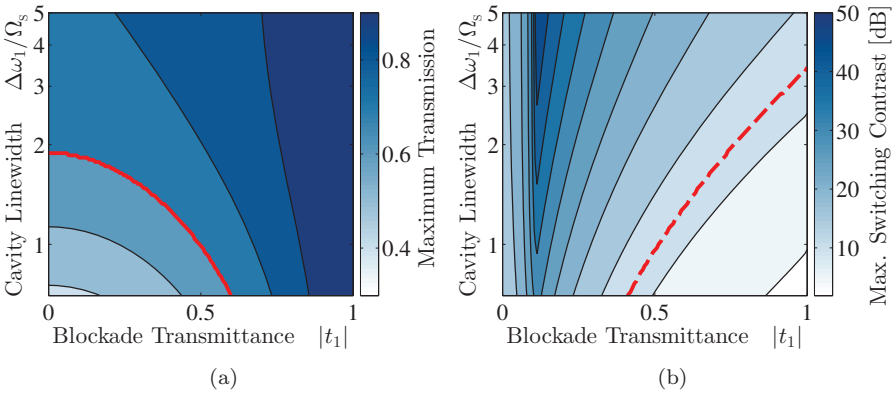

Figure 8.13: (a) Maximum energy transmission as a function of the blockade transmittance and cavity linewidth. The solid red line indicates the curve $T_U = 0.7$. (b) Maximum switching contrast as a function of the blockade transmittance and cavity linewidth. The dashed red line indicates the curve $T_U^{max}/T_U^{min} = 12$dB.

quirements. It is thus seen from Fig. 8.13 that certain regions of the parameter space $(|t_1|, \Delta\omega_1)$ may be excluded, since the requirements cannot be fulfilled in

those subspaces.

In the discussion related to Figs. 7.6(a) and 7.6(b) in Chapter 7, we used the relative change in the output energy, cf. Eq. (7.5.4), to explain the observed behavior. Here, we shall generalize this approach to investigate the exact differences defined by our performance criteria instead of the differential in Eq. (7.5.4). Using the differential corresponds to the special case, where the requirement on the contrast is very small and there is no bound on the "on" state transmission. From Eqs. (2.2.19) and (5.2.2) we can calculate which detuning $\delta_{\mathrm{S}}^{\mathrm{min}}$ will result in a minimum nonlinear shift $\delta_{\mathrm{NL}}^{\mathrm{min}}$, such that the "on" state transmission $T_{\mathrm{U}}(\delta_{\mathrm{S}}^{\mathrm{min}} + \delta_{\mathrm{NL}}^{\mathrm{min}}) \geq 0.7$ and the switching contrast $T_{\mathrm{U}}(\delta_{\mathrm{S}}^{\mathrm{min}} + \delta_{\mathrm{NL}}^{\mathrm{min}})/T_{\mathrm{U}}(\delta_{\mathrm{S}}^{\mathrm{min}}) \geq 12\mathrm{dB}$. The procedure is illustrated in Fig. 8.14(a). A detuning range $\delta_{\mathrm{S}} \in [-4\Delta\omega_1; 4\Delta\omega_1]$ is scanned for pairs $(\delta_{\mathrm{S}}^{\mathrm{min}}, \delta_{\mathrm{NL}})$ fulfilling

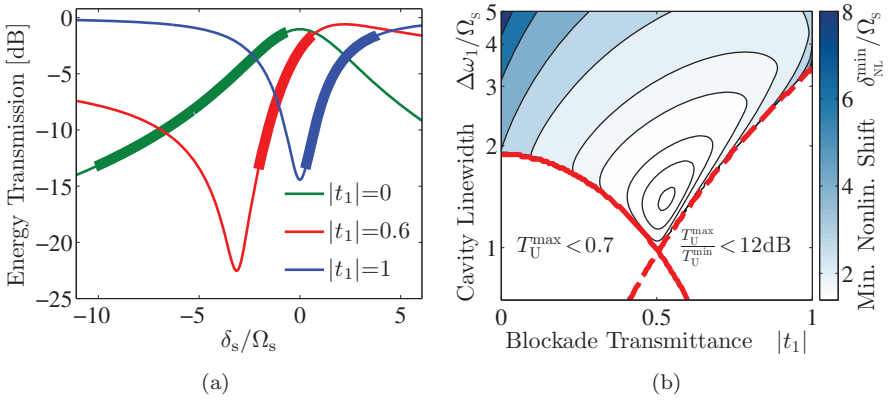

Figure 8.14: (a) Illustration of the minimum resonance shift for different values of the blockade transmittance. The detuning at the left and right ends of the thick parts of the curves are $\delta_{\mathrm{S}}^{\mathrm{min}}$ and $\delta_{\mathrm{S}}^{\mathrm{min}} + \delta_{\mathrm{NL}}^{\mathrm{min}}$, respectively. A cavity linewidth of $\Delta\omega_1 = 5\Omega_{\mathrm{S}}$ was used. (b) Dependence of the minimum resonance shift on the blockade transmittance and the cavity linewidth. The red curves are the same as in Figs. 8.13(a) and 8.13(b). In both panels a coupling ratio of $\gamma_1/\gamma_{\mathrm{C}} = 0.9$ was used.

the mentioned relations. In Fig. 8.14(a) the thick parts of the curves indicate the intervals $[\delta_{\mathrm{S}}^{\mathrm{min}}; \delta_{\mathrm{S}}^{\mathrm{min}} + \delta_{\mathrm{NL}}^{\mathrm{min}}]$, which result in the minimum required resonance shift for three different blockade transmittances shown. $\delta_{\mathrm{S}}^{\mathrm{min}}$ is thus expected to correspond to the optimum operation frequency. It is evident from Fig. 8.14(a) that the Fano resonance results in a significantly smaller detuning shift than the Lorentzian line. Even though Ω_{S} sets the frequency scale of our problem, the scanned detuning range is relative to the cavity linewidth, because the range of validity of the perturbation theory yielding the resonance shift must be related to $\Delta\omega_1$. This has not been investigated in detail, and the chosen range is therefore somewhat arbitrary.

In Fig. 8.14(b) we map out the dependence of the minimum resonance shift

$\delta_{\mathrm{NL}}^{\mathrm{min}}$ on the blockade transmittance as well as the cavity linewidth. When the cavity linewidth increases, the transmission broadens, which increases the required nonlinear shift $\delta_{\mathrm{NL}}^{\mathrm{min}}$ to achieve the targeted switching contrast. When the cavity linewidth becomes small compared to the pulse bandwidth, the behavior is more complicated. For $|t_1|$ close to 1, the energy transmission will be close to its maximum and almost independent of the detuning. For $|t_1|$ close to zero, the CW transmission can be approximated by a Dirac delta distribution causing the energy transmission to follow the shape of the input pulse spectrum. From Fig. 8.14(b) it appears that a minimum in the nonlinear shift exists for any given blockade transmittance, unless the transmission requirements are violated before this minimum occurs.

The relation between the nonlinear shift δ_{NL} and the pump energy inside the cavity depends on the nature of the nonlinearity, see Eq. (5.4.7e). The cavity energy, however, increases with decreasing cavity linewidth in a manner, which is independent of $|t_1|$ as seen from Eq. (2.2.21). Therefore, for any given $\Delta\omega_1$, the switching energy is expected to be reduced by choosing $|t_1|$ to minimize $\delta_{\mathrm{NL}}^{\mathrm{min}}$, because it sets a lower bound on the nonlinear shift, and hence, on the required pump energy. From Fig. 8.14(b) it is seen that the advantage of the Fano resonance compared to the Lorentzian resonance (at $|t_1| = 0$) is twofold: First, a smaller nonlinear shift is required, and second, a smaller cavity linewidth may be used without violating the requirements.

As discussed above, it is necessary to consider the exact dependence of δ_{NL} on pump energy to investigate the switching energy reduction corresponding to the reduction in $\delta_{\mathrm{NL}}^{\mathrm{min}}$ seen in Fig. 8.14(b). As a simple example, we shall consider a system similar to the one studied in Chapter 7, which is described by Eqs. (7.2.1a) and (7.2.1b). Here, we will assume $K_{\mathrm{Kerr}}^{11} = K_{\mathrm{Kerr}}^{21} = 0$ and $K_{\mathrm{Kerr}}^{12} = K_{\mathrm{Kerr}}^{22}$. Since our design is intended for a free carrier induced nonlinearity, which shifts the resonance oppositely to the Kerr effect, we simply change the sign on the Kerr coefficient in the analysis, so it may be used in the "switch on" scheme.

The relation between the signal output and the cavity field is given by Eq. (2.2.23). We vary the blockade transmittance $|t_1|$ and resonance linewidth $\Delta\omega_1$. For each parameter set, the signal detuning is chosen to be $\delta_{\mathrm{S}} = \delta_{\mathrm{S}}^{\mathrm{min}}$ corresponding to the minimum nonlinear shifts in Fig. 8.14(b). A minimum pump energy $U_{\mathrm{Pi}}^{\mathrm{min}}$ is then found by varying the pump parameters: Detuning δ_{P}, bandwidth Ω_{P}, and delay with respect to the signal τ_1. The result is shown in Fig. 8.15. It is observed that the features of Fig. 8.15 are very similar to those in Fig. 8.14(b). From Eq. (7.2.1a) it is seen that the nonlinear effect only frequency shifts the linear transmission spectrum. Furthermore, $\delta_{\mathrm{NL}}^{\mathrm{min}}$ and $\delta_{\mathrm{NL}}(t)$ scale similarly with the cavity linewidth, because δ_{NL} is directly proportional to the cavity energy. In fact, the deviations between Fig. 8.15 and Fig. 8.14(b) are only caused by the dynamical shift of the resonance in the nonlinear case, as discussed above.

We observe that the optimum switching energy in Fig. 8.15 corresponding to the Fano resonance with $|t_1| \simeq 0.5$ is an order of magnitude smaller than for

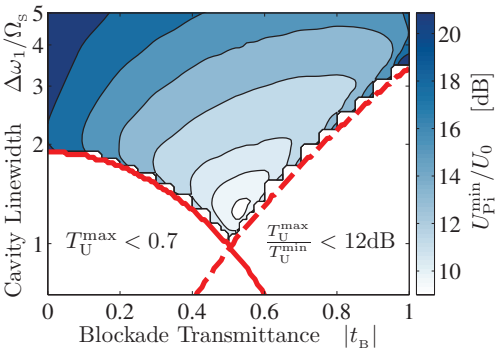

Figure 8.15: Minimum switching energy $U_{\mathrm{Pi}}^{\mathrm{min}}$ as a function of the resonance linewidth $\Delta\omega_1$ and blockade transmittance $|t_1|$. The characteristic energy is given by $U_0 = \Omega_{\mathrm{S}}/K_{\mathrm{Kerr}}^{22}$.

the Lorentzian line with $|t_1| = 0$. The size of this reduction generally depends on the nonlinear mechanism responsible for the resonance shift, but from the considerations related to Fig. 8.14(b) above, a significant reduction is expected in the general case. Finally, we note that the increased sensitivity to the resonance frequency of the Fano resonance may find application in a broader range of devices including sensors and external modulators.

8.4 Fabricated Devices

To validate that our design can be used to fabricate devices with the desired properties, we show a few examples of fabricated structures in this section. It is stressed that all the work on fabrication and characterization presented here, has been carried out by Yi Yu. Fig. 8.16 shows scanning electron microscope images (SEM) of three different structure types (upper panels) as well as measured CW transmission spectra (lower panels). The different structures are similar to those in Fig. 8.10, and it is clearly observed that the fabricated devices show the expected behavior.

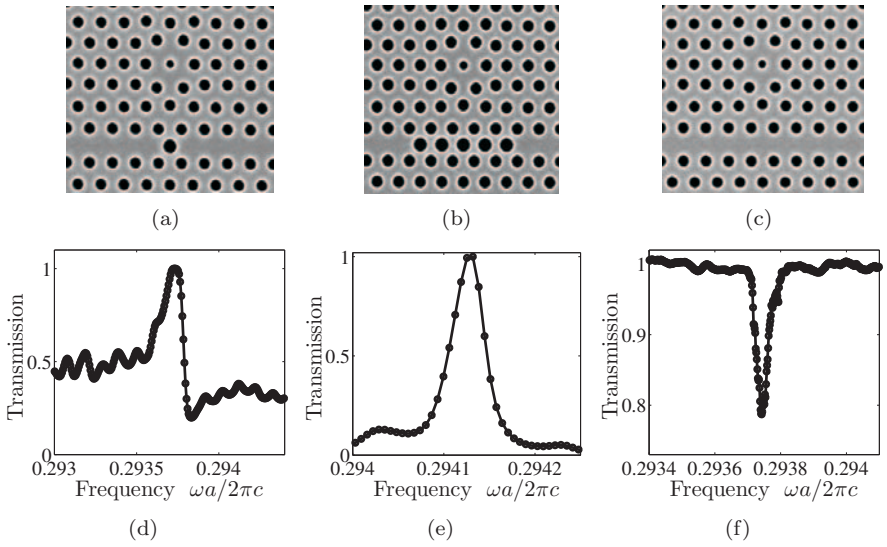

Figure 8.16: Fabricated structures with a Fano resonances. The upper panels show SEM images of the devices and the lower panels contain measured transmission spectra. (a) and (d) show a structure with a Fano resonance similar to the red curve in Fig. 8.10. (b) and (e) show a conventional Lorentzian resonance similar to the green curve in Fig. 8.10. (c) and (f) show a side coupled configuration similar to the blue curve in Fig. 8.10. (Courtesy of Yi Yu).

9

Energy Reduction by Tailoring the Input Pulse Properties

9.1 Introduction

In Sections 5.2.2 and 8.3 it was observed that the switching contrast in the linear regime found from Eq. (5.2.2) could be increased by using an input field with sharp spectral features, see Figs. 5.7(b) and 8.13(b). In this final chapter we will use the general mathematical framework of optimal control theory [77] to investigate how the device performance may be improved by controlling the properties of the input fields. All the degrees of freedom of the fields may be included in this optimization, including the phase.

9.2 Optimal Control Theory

In the formulation of the optimal control problem in Ref. [77], there is an objective function J, a set of ordinary differential equations (ODEs), and a set of boundary conditions

$$J = \int_{t_i}^{t_f} L(t, \mathbf{u}, \mathbf{x}) dt \tag{9.2.1}$$

$$\dot{\mathbf{u}} = \mathbf{f}(t, \mathbf{u}, \mathbf{x}) \quad , \quad \mathbf{u}(t_i) = \mathbf{u}_i \quad \text{and} \quad \boldsymbol{\beta}(\mathbf{u}_f) = \mathbf{0}. \tag{9.2.2}$$

The problem is defined on the time interval $t \in [t_i;\ t_f]$, the $n \times 1$ column vector $\mathbf{u}$ contains the n state variables (e.g. $a_{\mathrm{S}},\ a_{\mathrm{P}},\ N_1,\ N_2$) and the $m \times 1$ vector $\mathbf{x}$ holds the m control variables (e.g. $s_{\mathrm{P}}^{\mathrm{i}},\ s_{\mathrm{S}}^{\mathrm{i}}$). Initial conditions on the state variables are contained in $\mathbf{u}_i$, and the $p \times 1$ vector $\boldsymbol{\beta}$ with $p \leq n$ contains

information about final conditions on the state variables. The dot denotes a time-derivative and all parameters in boldface are vectors or matrices, whereas the other parameters are scalars.

The underlying idea is to determine the functions $\mathbf{x}$ such that the objective function is minimized. This is done by searching for local extrema, $dJ=0$. To verify that a minimum is obtained, it is in principle necessary to determine the second order differential of J. Since the resulting equations for $\mathbf{x}$ are nonlinear ODEs, there is no general uniqueness theorem guaranteeing that a global minimum was found. Even with these limitations, we consider the method to be useful, since it is always possible to compare the solutions with more conventional choices such as Gaussian, Square, or Lorentzian input functions. By defining the scalar functions

$$J' = G(\mathbf{u}_f, \boldsymbol{\nu}) + \int_{t_0}^{t_f} \Big(H(t, \mathbf{u}, \mathbf{x}, \boldsymbol{\lambda}) - \boldsymbol{\lambda}^T \dot{\mathbf{u}} \Big)\, dt \tag{9.2.3}$$

$$G = \boldsymbol{\nu}^T \boldsymbol{\beta}(\mathbf{u}_f) \tag{9.2.4}$$

$$H = L(t, \mathbf{u}, \mathbf{x}) + \boldsymbol{\lambda}^T \mathbf{f}(t, \mathbf{u}, \mathbf{x}), \tag{9.2.5}$$

and setting $dJ'=0$, the following equations are found [77]

$$\dot{\boldsymbol{\lambda}}^T = -H_{\mathbf{u}} \quad , \quad \boldsymbol{\lambda}_f^T = G_{\mathbf{u}_f} \tag{9.2.6}$$

$$H_{\mathbf{x}} = \mathbf{0}. \tag{9.2.7}$$

The functions $\boldsymbol{\lambda}(t)$ and constants $\boldsymbol{\nu}$ are Lagrange multipliers, and Eqs. (9.2.6) and (9.2.7) are often referred to is the adjoint problem. The partial derivatives of scalar functions with respect to a column vector variable are row vectors defined as

$$H_{\mathbf{u}} = \left[\frac{\partial H}{\partial u_1}, \ \frac{\partial H}{\partial u_2}, \ \ldots, \frac{\partial H}{\partial u_n} \right]. \tag{9.2.8}$$

Depending on the type of problem we are interested in, the objective function must be defined accordingly. In the next section we will discuss a particular problem, which has analytic solutions and illustrates the general method.

9.3 Switching the Cavity Energy

As it was seen in Chapter 7, it may be of critical importance for high speed switching applications that the pump energy enters and exits the cavity as fast as possible. In this example, we shall consider a minimization problem, where the cavity energy is changed from $U_{\mathrm{P}i}$ to $U_{\mathrm{P}f}$ in a fixed time $t_f - t_i$ by injecting as little energy as possible. The work presented in this section is contained in Ref. [78]. The objective function is

$$J = U_{\mathrm{P}}^{\mathrm{i}} = \int_{t_i}^{t_f} P_{\mathrm{P}}^{\mathrm{i}} dt. \tag{9.3.1}$$

For the sake of simplicity, we will consider a system containing only a Kerr nonlinearity, which is governed by the temporal coupled mode theory (TCMT) equation

$$\dot{a}_{\mathrm{P}} = -i\left[\delta_{\mathrm{P}} - K_{\mathrm{Kerr}}|a_{\mathrm{P}}(t)|^2\right] a_{\mathrm{P}}(t) - \gamma_{\mathrm{C}} a_{\mathrm{P}}(t) + \sqrt{\gamma_{\mathrm{C}}} s^{\mathrm{i}}_{\mathrm{P}}(t). \tag{9.3.2}$$

As in Chapter 7, it is assumed that there is no nonlinear change of the cavity decay, which is completely governed by the cavity-waveguide coupling, $\gamma_{\mathrm{C}} = \gamma_1$. The fields $a_{\mathrm{P}} = \sqrt{U_{\mathrm{P}}}\exp(i\phi_{\mathrm{P}})$ and $s^{\mathrm{i}}_{\mathrm{P}} = \sqrt{P^{\mathrm{i}}_{\mathrm{P}}}\exp(i\phi^{\mathrm{i}}_{\mathrm{P}})$ are complex, and in this case it turns out to be useful to write Eq. (9.3.2) as two real equations for the cavity energy U_{P} and phase ϕ_{P}

$$\dot{U}_{\mathrm{P}} = -2\gamma_{\mathrm{C}} U_{\mathrm{P}} + 2\sqrt{\gamma_{\mathrm{C}} P^{\mathrm{i}}_{\mathrm{P}} U_{\mathrm{P}}}\cos\left(\phi_{\mathrm{P}} - \phi^{\mathrm{i}}_{\mathrm{P}}\right) \tag{9.3.3}$$

$$\dot{\phi}_{\mathrm{P}} = -\delta_{\mathrm{P}} + K_{\mathrm{Kerr}} U_{\mathrm{P}} - \sqrt{\frac{\gamma_{\mathrm{C}} P^{\mathrm{i}}_{\mathrm{P}}}{U_{\mathrm{P}}}}\sin(\phi_{\mathrm{P}} - \phi^{\mathrm{i}}_{\mathrm{P}}). \tag{9.3.4}$$

Let us introduce the normalized variables: $u_1 = U_{\mathrm{P}}/U_{\mathrm{Kerr}}$, $u_2 = \phi_{\mathrm{P}}$, $x_1 = P^{\mathrm{i}}_{\mathrm{P}}/P_{\mathrm{Kerr}}$, $x_2 = \phi^{\mathrm{i}}_{\mathrm{P}}$, $\tau = t2\gamma_{\mathrm{C}}$, and $\Delta_{\mathrm{P}} = \delta_{\mathrm{P}}/2\gamma_{\mathrm{C}}$, where

$$U_{\mathrm{Kerr}} = \frac{\gamma_{\mathrm{C}}}{K_{\mathrm{Kerr}}} \quad \text{and} \quad P_{\mathrm{Kerr}} = \frac{\gamma_{\mathrm{C}}^2}{K_{\mathrm{Kerr}}}. \tag{9.3.5}$$

By inserting into Eqs. (9.3.3) and (9.3.4), the equations take the form

$$\dot{u}_1 = -u_1 + \sqrt{x_1 u_1}\cos\left(u_2 - x_2\right) \tag{9.3.6}$$

$$\dot{u}_2 = -\Delta_{\mathrm{P}} + \frac{1}{2}u_1 - \frac{1}{2}\sqrt{\frac{x_1}{u_1}}\sin(u_2 - x_2), \tag{9.3.7}$$

where the dot now means the derivative with respect to τ. The boundary conditions are $u_{1i} = U_{\mathrm{P}i}/U_{\mathrm{Kerr}}$ and $u_{1f} = U_{\mathrm{P}f}/U_{\mathrm{Kerr}}$. From the equations in the previous section, the optimum solution for the input field may be found. Let us first write the equations for this example

$$H = x_1 + \lambda_1\left[-u_1 + \sqrt{x_1 u_1}\cos\left(u_2 - x_2\right)\right] + \lambda_2\left[-\Delta_{\mathrm{P}} + \frac{1}{2}u_1 - \frac{1}{2}\sqrt{\frac{x_1}{u_1}}\sin(u_2 - x_2)\right], \tag{9.3.8}$$

where the first term comes from $L(t, \mathbf{u}, \mathbf{x})$. From the boundary conditions, it is seen that

$$\boldsymbol{\beta} = \begin{bmatrix} u_{1f} - U_{\mathrm{P}f}/U_{\mathrm{Kerr}} \\ 0 \end{bmatrix} \quad \Rightarrow \quad G = \nu_1\left(u_{1f} - U_{\mathrm{P}f}/U_{\mathrm{Kerr}}\right). \tag{9.3.9}$$

Inserting into Eqs. (9.2.6) and (9.2.7), the adjoint equations are obtained

$$0 = 2\sqrt{x_1} + \sqrt{u_1}\lambda_1 \cos(u_2 - x_2) - \frac{\lambda_2 \sin(u_2 - x_2)}{2\sqrt{u_1}} \tag{9.3.10}$$

$$0 = \frac{\sqrt{x_1}\lambda_2 \cos(u_2 - x_2)}{2\sqrt{u_1}} + \sqrt{u_1 x_1}\lambda_1 \sin(u_2 - x_2) \tag{9.3.11}$$

$$\dot{\lambda}_1 = \lambda_1 \left(-1 + \frac{\sqrt{x_1}\cos(u_2 - x_2)}{2\sqrt{u_1}} \right) + \lambda_2 \left(\frac{1}{2} + \frac{\sqrt{x_1}\sin(u_2 - x_2)}{4u_1^{3/2}} \right) \tag{9.3.12}$$

$$\dot{\lambda}_2 = -\frac{\sqrt{x_1}\lambda_2 \cos(u_2 - x_2)}{2\sqrt{u_1}} - \sqrt{u_1 x_1}\lambda_1 \sin(u_2 - x_2) \tag{9.3.13}$$

$$\lambda_{2f} = 0. \tag{9.3.14}$$

The right hand sides of Eqs. (9.3.11) and (9.3.13) are identical except for a sign difference, which means $\dot{\lambda}_2 = 0$. Combining this information with the boundary condition in Eq. (9.3.14), it is clear that $\lambda_2(\tau) = 0$. Since x_1 cannot be zero in the entire domain, we see from Eq. (9.3.10) that λ_1 must be non-zero as well. From Eq. (9.3.11) it is then found that $\sin(u_2 - x_2) = 0$. Solving Eq. (9.3.10) for x_1 and inserting the result into Eqs. 9.3.6, 9.3.7, and 9.3.12, while remembering that $\cos^2(u_2 - x_2) = 1$, the equation system is reduced to the following

$$\dot{u}_1 = -\frac{1}{2} u_1 (2 + \lambda_1) \tag{9.3.15}$$

$$\dot{u}_2 = \frac{1}{2} (u_1 - 2\Delta_{\mathrm{P}}) \tag{9.3.16}$$

$$\dot{\lambda}_1 = \lambda_1 \left(1 + \frac{1}{4}\lambda_1 \right). \tag{9.3.17}$$

The equation for λ_1 is readily solved with the result

$$\lambda_1(\tau) = \frac{4}{\exp(-\tau - c_1) - 1}, \tag{9.3.18}$$

where c_1 is an integration constant. Inserting this into Eq. (9.3.15) and solving for u_1, we find

$$u_1(\tau) = \exp(c_2 - \tau)\big[\exp(\tau + c_1) - 1\big]^2. \tag{9.3.19}$$

The integration constants c_1 and c_2 are found from the initial and final condition on u_1. The input phase is found by integration of Eq. (9.3.16) and x_1 follows directly from inserting into Eq. (9.3.10)

$$u_2(\tau) = -\frac{1}{2}\exp(c_2 - \tau) + \frac{1}{2}\exp(2c_1 + c_2 + \tau) - \exp(c_1 + c_2)\tau - \Delta_{\mathrm{P}}\tau + c_3 \tag{9.3.20}$$

$$x_1(\tau) = 4\exp(2c_1 + c_2 + \tau). \tag{9.3.21}$$

The integration constant c_3 must be chosen to match the initial condition on the phase of the input field $\phi_{\mathrm{P}}^{\mathrm{i}}(t_i)$. From the above solutions it is clear that the absolute value of the input phase is irrelevant since it enters as $u_2 - x_2 = (2p+1)\pi,\ p \in \mathbb{Z}_0$, so c_3 may be chosen arbitrarily. The solutions are valid for both "switch on" ($U_{\mathrm{P}i} < U_{\mathrm{P}f}$) and "switch off" ($U_{\mathrm{P}i} > U_{\mathrm{P}f}$) operations, and in Fig. 9.1 an example of both operations is shown. We note that the input power jumps discontinuously at the endpoints of the "switch on" and "switch off" intervals. Even if this behavior is not exactly possible to achieve experimentally, the analysis is very useful as it provides the ultimate limit of the power consumption for a given structure within the validity of the model. Another interesting observation is that the "on state" cavity energy may be made arbitrarily large by increasing the input power accordingly. Alternatively, the "switch on" time $t_f - t_i$ may be made arbitrarily small at the expense of increasing the input power. In a similar manner, the optical energy may be removed from the cavity arbitrarily fast. This may seem counter-intuitive since the decay of the cavity energy is determined by the coupling rate γ_{C}. However, by injecting light with the proper phase relative to the cavity field, it is possible to drive the energy out of the cavity by an interference effect. This kind of coherent control is well known in the optical manipulation of atomic and molecular systems [79–81], where it is used to enhance certain transitions between specific states while suppressing other transitions. Recently, coherent control was applied for a problem similar to the one studied here [82], and in Ref. [83] two consecutive pulses with a π phase difference were used to excite and de-excite the field inside an optical cavity at timescales much faster than the cavity lifetime. Escape of the cavity energy faster than the photon lifetime was also observed in Section 7.3.

The effect of using coherent control is illustrated in Fig. 9.1(a), where the dashed blue curve shows the time evolution of the cavity energy in the case of no input during the "switch off" interval. In this curve, the energy decays with γ_{C}, but the solid red curve shows that the energy may be reduced faster by injecting a field in the "switch off" interval. To ensure that the energy stays at zero at times larger than t_f, the input must be switched off abruptly at this time. From Eq. (9.3.6) this is seen to make $\dot{u}_1 = 0$, and hence, the cavity energy will remain at zero.

From the above results, it appears as if the optimum input energy does not depend on the detuning Δ_{P}. However, since the time derivative of x_2 equals that of u_2, the input field will in fact be at resonance. This is seen by writing the total field from Eq. (2.2.20)

$$S_{\mathrm{P}}^{\mathrm{i}}(t) = \sqrt{P_{\mathrm{P}}^{\mathrm{i}}(t)}\exp(-i\omega_{\mathrm{P}}t)\times \exp\left[i\left(\phi_{\mathrm{P}}^{\mathrm{i}}(t_0) + \frac{d\phi_{\mathrm{P}}^{\mathrm{i}}}{dt}(t-t_0) + \mathcal{O}(t^2)\right)\right], \quad (9.3.22)$$

where the input phase was written as a Taylor expansion in t. From Eq. (9.3.16) the first derivative is seen to have a contribution of $-\delta_{\mathrm{P}} = -\omega_1 + \omega_{\mathrm{P}}$, which shows

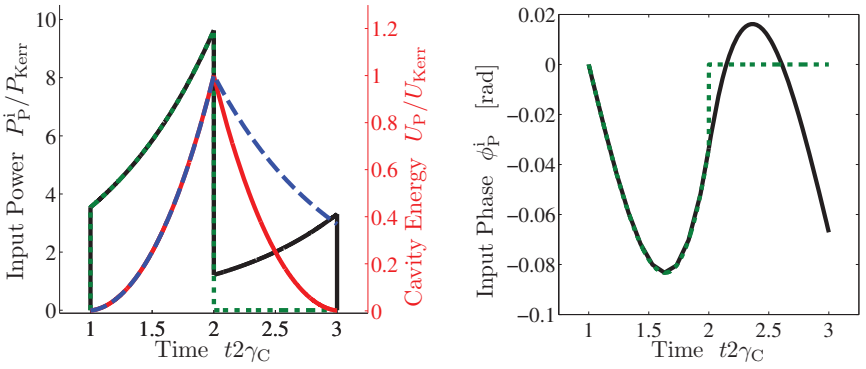

Figure 9.1: Illustration of the optimum input field for switching the cavity energy on and off. The values of the example are: $U_{{\rm P}i} = 0$, $U_{{\rm P}f} = U_{\rm Kerr}$, $\Delta_{\rm P} = 0.2$, and $\phi_{\rm P}^{\rm i}(t_i) = 0$. The "switch on" time interval is between $\tau = 1$ and $\tau = 2$, while the "switch off" interval is from $\tau = 2$ to $\tau = 3$. (a) The left axis represent values of the black and dashed green curves, while the right axis shows the values of the red and dashed blue curves. The black curve corresponds to the optimum input power, while the dashed green follows the optimum for the "switch on" and is then simply turned off during the "switch off" interval. The red curve shows the cavity energy corresponding to the optimum input, while the dashed blue shows the energy for the input that is switched off at $\tau = 2$. (b) The black curve shows the phase variation of the optimum input pulse. For the input being turned off at $\tau = 2$, we also turn off the phase variation, which is shown by the dashed green curve.

that the total field oscillates at the resonance with some additional phase variation given by Eq. (9.3.20). If one insists that the input field oscillates at $\omega_{\rm P}$ with some additional phase variation, it is necessary to expand the theory in Section 9.2 to include boundary conditions on the control variables. Then, the condition: $\phi_{\rm P}^{\rm i}(t_f) - \phi_{\rm P}^{\rm i}(t_i) = \delta_{\rm P} \times (t_f - t_i)$ could be imposed.

We may imagine many other problems that can be formulated in terms of the optimal control theory of Section 9.2. For instance, for a given signal input, the problem of maximizing the output energy of the signal while injecting a pump with a fixed pulse energy is very relevant. In such a case, the optimum pump amplitude and phase variation could be obtained. The additional constraint of a fixed pump energy may be implemented in a simple manner. The constraint reads

$$U_{\rm P}^{\rm i} = \int_{t_i}^{t_f} P_{\rm P}^{\rm i} dt, \tag{9.3.23}$$

where $U_{\rm P}^{\rm i}$ is a fixed number. The set of n state variables may be expanded with

the anti-derivative of $P_{\mathrm{P}}^{\mathrm{i}}$

$$u_{n+1}(t) = u_{n+1}(t_i) + \frac{1}{P_{\mathrm{Kerr}}} \int_{t_i}^{t} P_{\mathrm{P}}^{\mathrm{i}}(t')dt' \quad \Leftrightarrow \quad \dot{u}_{n+1} = \frac{P_{\mathrm{P}}^{\mathrm{i}}}{P_{\mathrm{Kerr}}}.$$

The physical interpretation of $u_{n+1}(t)$ is the amount of pump energy having entered the cavity at time t. An initial condition must be applied to fix $u_{n+1}(t_i)$ and the final condition on the new variable is $u_{n+1}(t_f) = U_{\mathrm{P}}^{\mathrm{i}}/U_{\mathrm{Kerr}}$.

In future work, we intend to apply the optimal control theory to such more advanced problems to investigate the ultimate limitations on switching energy. Conditions on the maximum slope of the input variables could be imposed to make the solutions more compatible with experimentally realizable pulses. It should be kept in mind that the energy reduction resulting from pulse shaping and coherent control must outweigh the energy required to produce such variations. This is a consideration, which should be addressed when implementing these schemes in an integrated optical circuit.

10

Conclusion and Outlook

The work in this thesis is the starting point of a research effort within all-optical switching in photonic crystal (PC) membrane structures in the group of Jesper Mørk at DTU Fotonik. The relatively broad range of focus areas is a reflection of this. The ambition of the project was to obtain an understanding of the underlying physics of such structures, and to use this knowledge to identify challenges and possible solutions as well as limitations of devices based on this platform.

The temporal coupled mode theory is widely used in the literature as a simple yet exhaustive model of waveguide-cavity structures. In Chapter 3 we considered a rigorous perturbation theory for calculating the first order corrections to the complex eigenfrequency of the cavity. The method takes into account the leaky nature of the cavity modes, which is an issue that seems to be ignored in most of the literature on nonlinear dynamics of such structures. Corrections to the imaginary part of the eigenfrequency result naturally from this approach, but are neglected in perturbation calculations based on a Hermitian eigenvalue problem. We also applied this general approach to carrier induced nonlinearities, where comparisons with full numerical simulations are not available presently. A first attempt at accounting for diffusion effects was implemented by considering two carrier distributions, which exchange particles at a rate proportional to the density difference between them.

Experimental techniques and results from different types of measurements were discussed in Chapter 5. We learned that studying the nonlinear dynamics of cavity structures is nontrivial due to the need for separation of the pump and signal before detection. From a comparison of experimental results with simulations based on the model derived in Chapter 3, it was seen that a qualitative agreement can be achieved, which provides confidence in the model capturing the physical mechanisms of the real structures.

A substantial part of the work in this thesis has been concerned with structural design. This effort was mainly aimed at supporting the fabrication and characterization activities undertaken by Yi Yu. The first designs of two port

structures similar to those already presented in the literature, were merely intended as a test of the design-fabrication-characterization process. The more advanced design discussed in Chapter 6 is believed to provide an integrated platform for studying the cavity dynamics without complex modulation techniques. The spatial separation of the pump and signal enabled by the design also offers important flexibility, which we believe is essential for real devices.

The flexibility of the four port design was utilized in Chapter 7 to study the limitations set by the coupling rates of the signal and pump in high speed operation. Even though we believe carrier induced nonlinearities to be more promising than the Kerr effect due to a lower energy requirement, the analysis in Chapter 7 provided a substantial improvement in our understanding of the cavity dynamics, and the limitations set by the quality factors are also important for design considerations in the case of carrier nonlinearities.

The two last chapters of the thesis are concerned with improvements of the switching energy in waveguide-cavity structures. It was shown that structures exhibiting Fano resonances are very sensitive to small changes in the signal detuning, which may greatly reduce the necessary pump energy to achieve any specified switching contrast. A general method for optimizing the properties of the input pulses resulting in an energy reduction was discussed in Chapter 9. The advantage of such a mathematical framework is that it provides estimates of the ultimate limitations of a certain structure within the range of validity of the model.

We believe that the results in this thesis represent some contributing aspects to the ongoing discussion of the viability of all-optical logic devices in future integrated communication systems. In the final section of the thesis, we will provide suggestions for future work that could assist in determining the ultimate limitations of PC waveguide-cavity switching devices.

10.1 Future Directions

First of all, we believe that more work is needed on the model of carrier dynamics. Some steps are already being taken in refining the way diffusion effects are included, which is based on solutions of the diffusion equation and comparisons with finite element modeling of the carrier dynamics of the considered structures. The temporal coupled mode theory (TCMT) equations should also be solved taking the full experimental technique of homodyne and heterodyne measurements into account. This would provide a direct means of comparison with the experimental results, as opposed to the approximate method used in Section 5.4. Further experimental efforts are also required, and in this respect, it will be very interesting to perform pump probe measurements using the four port structures considered in this thesis.

The relatively slow relaxation time of carriers observed in Chapter 5 pose a serious limitation on the switching speed. A solution to this problem has been suggested within semiconductor optical amplifier (SOA) based switches [84],

and the underlying idea of this approach may be implemented in waveguide-cavity structures by employing more advanced designs. If it is possible to make the transmission of the signal depend on the carrier density difference between to cavities, an effect similar to that proposed in Ref. [84] is expected.

Using the optimal control theory of Chapter 9 may provide a path for using cavity based switches for signals employing more advanced modulation formats utilizing the information in both the amplitude and phase of the light fields. An increase in the information density or decrease in switching energy is expected to be achievable from such an investigation. Such efforts should be combined with investigations of beam shaping mechanisms that are on-chip integrable and preferably passive to avoid additional energy consumption and complexity.

Designs for more advanced functionalities such as optically-controlled re-routing [85] should also be emphasized. The structures considered in this thesis simply reflect the signal pulse into the same port in the "off" state of the switch. In re-routing the state of the switch determines, which of two possible output ports the signal pulse will exit through. This represents a key functionality of integrated all-optical signal processing circuits. Designs utilizing a recycling of the pump pulse could also be interesting to investigate to further reduce the energy consumption per bit.

In terms of material systems, there are possibilities of incorporating quantum wells or quantum dots in the structures, which could be beneficial in terms of speed in the carrier relaxation dynamics [86]. Advances in selective growth techniques [87] offers the freedom to place the active material only at the cavity region, which has advantages in terms of energy consumption and heating issues as well as loss in the access waveguides.

Appendix A

Perturbation Theory

A.1 Perturbation of the Wave Equation

In this appendix, we solve Eq. (3.2.3) for the first order correction to the eigenfrequency using the boundary condition in Eq. (2.2.7). We state Eq. (3.2.3) again for reference

$$\nabla\times\nabla\times\mathbf{E}^{(1)} - \frac{2\tilde{\omega}^{(0)}\tilde{\omega}^{(1)}}{c^2}\epsilon_r\mathbf{E}^{(0)} - \frac{(\tilde{\omega}^{(0)})^2}{c^2}\epsilon_r\mathbf{E}^{(1)} - \frac{(\tilde{\omega}^{(0)})^2}{c^2}\Delta\epsilon_{\mathrm{r}}(\mathbf{E}^{(0)})\mathbf{E}^{(0)} = \mathbf{0}.$$

First, we take the dot product of both sides of Eq. (3.2.3) with $\mathbf{E}^{(0)}$ and integrate

$$\int_V \mathbf{E}^{(0)}\cdot\left[\nabla\times\nabla\times - \frac{(\tilde{\omega}^{(0)})^2}{c^2}\epsilon_{\mathrm{r}}\right]\mathbf{E}^{(1)}dV = \frac{2\tilde{\omega}^{(0)}\tilde{\omega}^{(1)}}{c^2}\int_V \epsilon_r\mathbf{E}^{(0)}\cdot\mathbf{E}^{(0)}dV + \frac{(\tilde{\omega}^{(0)})^2}{c^2}\int_V \Delta\epsilon_{\mathrm{r}}\mathbf{E}^{(0)}\cdot\mathbf{E}^{(0)}dV. \quad \text{(A.1.1)}$$

Now we look at the left hand side (LHS) and start with the part of the integral containing the rotation operators

$$\int_V \mathbf{E}^{(0)}\cdot\nabla\times\nabla\times\mathbf{E}^{(1)}dV.$$

We will use integration by parts to transfer the operators from $\mathbf{E}^{(1)}$ to $\mathbf{E}^{(0)}$, so we may use Eq. (3.2.2) to get rid of some terms. To do this, we need the operator identity [41]

$$\begin{aligned}\nabla\cdot[(\nabla\times\mathbf{G})\times\mathbf{F}] &= \mathbf{F}\cdot[\nabla\times(\nabla\times\mathbf{G})] - (\nabla\times\mathbf{G})\cdot(\nabla\times\mathbf{F}) \quad \Leftrightarrow\\ \mathbf{F}\cdot[\nabla\times(\nabla\times\mathbf{G})] &= \nabla\cdot[(\nabla\times\mathbf{G})\times\mathbf{F}] + (\nabla\times\mathbf{G})\cdot(\nabla\times\mathbf{F}),\end{aligned}$$

where $\mathbf{F}$ and $\mathbf{G}$ are arbitrary vector fields. We then have

$$\int_V [\mathbf{E}^{(0)} \cdot \nabla\times\nabla\times\mathbf{E}^{(1)} - \mathbf{E}^{(1)} \cdot \nabla\times\nabla\times\mathbf{E}^{(0)}]\, dV = \int_{\partial V} [(\nabla\times\mathbf{E}^{(1)})\times\mathbf{E}^{(0)} - (\nabla\times\mathbf{E}^{(0)})\times\mathbf{E}^{(1)}] \cdot d\mathbf{A}, \quad \text{(A.1.2)}$$

where Gauss' identity was used to convert the volume integral into a surface integral [41]. The vector $\hat{\mathbf{n}}$ is a unit vector perpendicular to the integration surface. Far from the perturbed region, the fields are outgoing spherical waves, which are solutions to Eq. (2.2.7). Including up to first order, the field is

$$\mathbf{E} = \mathbf{E}^{(0)} + \mathbf{E}^{(1)} = \mathbf{e}(1+\epsilon_1)\frac{e^{i[k^{(0)}+k^{(1)}]r}}{r} \quad \text{and} \quad \mathbf{E}^{(0)} = \mathbf{e}\frac{e^{ik^{(0)}r}}{r} \quad \Rightarrow$$
$$\mathbf{E}^{(1)} = \mathbf{e}(1+\epsilon_1)\frac{e^{i[k^{(0)}+k^{(1)}]r}}{r} - \mathbf{e}\frac{e^{ik^{(0)}r}}{r},$$

where $\mathbf{e}$ is perpendicular to $\hat{\mathbf{r}}$, and $\mathbf{k}^{(0)} = k^{(0)}\hat{\mathbf{r}}$. Using the identity [41]

$$\nabla\times[\psi(\mathbf{r})\mathbf{F}(\mathbf{r})] = \nabla\psi(\mathbf{r})\times\mathbf{F}(\mathbf{r}) + \psi(\mathbf{r})\nabla\times\mathbf{F}(\mathbf{r}),$$

we may write

$$\nabla\times\mathbf{E}^{(0)} = \nabla\left(\frac{e^{ik^{(0)}r}}{r}\right)\times\mathbf{e} = \frac{\partial}{\partial r}\left(\frac{e^{ik^{(0)}r}}{r}\right)\hat{\mathbf{r}}\times\mathbf{e}.$$

Insert this into the first term in the surface integral, we find

$$(\nabla\times\mathbf{E}^{(1)})\times\mathbf{E}^{(0)} = \frac{\partial}{\partial r}\left[(1+\epsilon_1)\frac{e^{i[k^{(0)}+k^{(1)}]r}}{r} - \frac{e^{ik^{(0)}r}}{r}\right](\hat{\mathbf{r}}\times\mathbf{e})\times\mathbf{e}\frac{e^{ik^{(0)}r}}{r} =$$
$$\left[(1+\epsilon_1)e^{i[k^{(0)}+k^{(1)}]r}\left(-\frac{1}{r^2} + \frac{i[k^{(0)}+k^{(1)}]}{r}\right) - e^{ik^{(0)}r}\left(-\frac{1}{r^2} + \frac{ik^{(0)}}{r}\right)\right]\left(\frac{e^{ik^{(0)}r}}{r}\right)(\hat{\mathbf{r}}\times\mathbf{e})\times\mathbf{e}.$$

The second term in the surface integral is

$$(\nabla\times\mathbf{E}^{(0)})\times\mathbf{E}^{(1)} = \frac{\partial}{\partial r}\left(\frac{e^{ik^{(0)}r}}{r}\right)(\hat{\mathbf{r}}\times\mathbf{e})\times\mathbf{e}\left(\frac{(1+\epsilon_1)e^{i[k^{(0)}+k^{(1)}]r}}{r} - \frac{e^{ik^{(0)}r}}{r}\right) =$$
$$e^{ik^{(0)}r}\left(-\frac{1}{r^2} + \frac{ik^{(0)}}{r}\right)\left(\frac{(1+\epsilon_1)e^{i[k^{(0)}+k^{(1)}]r}}{r} - \frac{e^{ik^{(0)}r}}{r}\right)(\hat{\mathbf{r}}\times\mathbf{e})\times\mathbf{e}.$$

Subtracting the second term from the first, we get

$$i(1+\epsilon_1)k^{(1)}\frac{e^{ik^{(0)}r}\left(1+e^{ik^{(1)}r}\right)}{r}\frac{e^{ik^{(0)}r}}{r}\left(\hat{\mathbf{r}}\times\mathbf{e}\right)\times\mathbf{e}\approx ik^{(1)}\frac{e^{ik^{(0)}r}}{r}\frac{e^{ik^{(0)}r}}{r}\left(\hat{\mathbf{r}}\times\mathbf{e}\right)\times\mathbf{e},$$

where second order terms proportional to $k^{(1)}e^{ik^{(1)}r}$ and $\epsilon_1 k^{(1)}$ have been neglected. Using the identity [41]

$$(\mathbf{G}\times\mathbf{H})\times\mathbf{F}=(\mathbf{F}\cdot\mathbf{G})\mathbf{H}-(\mathbf{F}\cdot\mathbf{H})\mathbf{G},$$

and $\mathbf{e}\cdot\hat{\mathbf{r}}=0$ since they are perpendicular, we get

$$\left(\hat{\mathbf{r}}\times\mathbf{e}\right)\times\mathbf{e}=-(\mathbf{e}\cdot\mathbf{e})\hat{\mathbf{r}}.$$

Using the above results, it is then seen that the integrand of the surface integral is

$$(\nabla\times\mathbf{E}^{(1)})\times\mathbf{E}^{(0)}-(\nabla\times\mathbf{E}^{(0)})\times\mathbf{E}^{(1)}=-ik^{(1)}\left(\mathbf{E}^{(0)}\cdot\mathbf{E}^{(0)}\right)\hat{\mathbf{r}}.$$

Inserting this into Eq. (A.1.2), we find

$$\int_V \mathbf{E}^{(0)}\cdot\nabla\times\nabla\times\mathbf{E}^{(1)}dV=\int_V \mathbf{E}^{(1)}\cdot\nabla\times\nabla\times\mathbf{E}^{(0)}dV-ik^{(1)}\int_{\partial V}\left(\mathbf{E}^{(0)}\cdot\mathbf{E}^{(0)}\right)\hat{\mathbf{r}}\cdot d\mathbf{A}. \quad \text{(A.1.3)}$$

Using this result in Eq. (A.1.1) and the relation $k^{(1)}=\tilde{\omega}^{(1)}\sqrt{\epsilon_{\mathrm{B}}}/c$, we get

$$\begin{aligned}
&-i\frac{\tilde{\omega}^{(1)}\sqrt{\epsilon_{\mathrm{B}}}}{c}\int_{\partial V}\left(\mathbf{E}^{(0)}\cdot\mathbf{E}^{(0)}\right)\hat{\mathbf{r}}\cdot d\mathbf{A}=\\
&\quad\frac{2\tilde{\omega}^{(0)}\tilde{\omega}^{(1)}}{c^2}\int_V\epsilon_{\mathrm{r}}\mathbf{E}^{(0)}\cdot\mathbf{E}^{(0)}dV+\frac{(\tilde{\omega}^{(0)})^2}{c^2}\int_V\Delta\epsilon_{\mathrm{r}}\mathbf{E}^{(0)}\cdot\mathbf{E}^{(0)}dV \quad\Rightarrow\\
&\quad\tilde{\omega}^{(1)}\left[\int_V\epsilon_{\mathrm{r}}\mathbf{E}^{(0)}\cdot\mathbf{E}^{(0)}dV+i\frac{c\sqrt{\epsilon_{\mathrm{B}}}}{2\tilde{\omega}^{(0)}}\int_{\partial V}\left(\mathbf{E}^{(0)}\cdot\mathbf{E}^{(0)}\right)\hat{\mathbf{r}}\cdot d\mathbf{A}\right]=\\
&\qquad-\frac{1}{2}\tilde{\omega}^{(0)}\int_V\Delta\epsilon_{\mathrm{r}}\mathbf{E}^{(0)}\cdot\mathbf{E}^{(0)}dV.
\end{aligned}$$

Finally, the first order perturbation of the eigenfrequency is given by

$$\tilde{\omega}^{(1)}=-\frac{1}{2}\tilde{\omega}^{(0)}\frac{\int_V\Delta\epsilon_{\mathrm{r}}\mathbf{E}^{(0)}\cdot\mathbf{E}^{(0)}dV}{\int_V\epsilon_{\mathrm{r}}\mathbf{E}^{(0)}\cdot\mathbf{E}^{(0)}dV+i\frac{c\sqrt{\epsilon_{\mathrm{B}}}}{2\tilde{\omega}^{(0)}}\int_{\partial V}\left(\mathbf{E}^{(0)}\cdot\mathbf{E}^{(0)}\right)\hat{\mathbf{r}}\cdot d\mathbf{A}}. \quad \text{(A.1.4)}$$

A.2 One Electric Field

Let us first assume a 2 dimensional space spanned by the Cartesian unit vectors $\hat{\mathbf{x}}$ and $\hat{\mathbf{y}}$, since this will simplify the notation without loss of generality. We make a further simplification by assuming that the materials we consider are isotropic. The only nonzero elements of the third order susceptibility are then [88]

$$\chi^{(3)}_{xxxx} = \chi^{(3)}_{yyyy} = \frac{1}{3}\chi^{(3)}_{xxyy} = \frac{1}{3}\chi^{(3)}_{xyxy} = \frac{1}{3}\chi^{(3)}_{xyyx} \tag{A.2.1}$$

The general expression for the i'th component of the nonlinear polarization at the frequency $\omega_n = \omega_a + \omega_b + \omega_c$ is [34, 88]

$$\frac{1}{2}P^{(3)}_i(\omega_a+\omega_b+\omega_c) = \sum_{jkl}\sum_{(abc)} \chi^{(3)}_{ijkl}(\omega_a+\omega_b+\omega_c)\frac{1}{2}E_j(\omega_a)\frac{1}{2}E_k(\omega_b)\frac{1}{2}E_l(\omega_c), \quad jkl = x, y\ . \tag{A.2.2}$$

The sum over a, b, c is understood to run only over all distinguishable combinations of a, b, c, where $\omega_a + \omega_b + \omega_c$ is constant. In Eq. (A.2.2) we have dropped the n subscripts from Eq. (3.3.2) because the arguments indicate the frequency components. Instead, the subscript here indicates the spatial component of the field amplitude.

Let us consider the simplest example of a single cavity field at the frequency ω. Then, Eq. (A.2.2) is given by

$$\begin{aligned}
&P^{(3)}_x(\omega) = \\
&\frac{1}{4}\chi^{(3)}_{xxxx}\left[E_x(\omega)E_x(\omega)E_x(-\omega)+E_x(\omega)E_x(-\omega)E_x(\omega)+E_x(-\omega)E_x(\omega)E_x(\omega)\right]+\\
&\frac{1}{4}\chi^{(3)}_{xxyy}\left[E_x(\omega)E_y(\omega)E_y(-\omega)+E_x(\omega)E_y(-\omega)E_y(\omega)+E_x(-\omega)E_y(\omega)E_y(\omega)\right]+\\
&\frac{1}{4}\chi^{(3)}_{xyxy}\left[E_y(\omega)E_x(\omega)E_y(-\omega)+E_y(\omega)E_x(-\omega)E_y(\omega)+E_y(-\omega)E_x(\omega)E_y(\omega)\right]+\\
&\frac{1}{4}\chi^{(3)}_{xyyx}\left[E_y(\omega)E_y(\omega)E_x(-\omega)+E_y(\omega)E_y(-\omega)E_x(\omega)+E_y(-\omega)E_y(\omega)E_x(\omega)\right]=\\
&\frac{1}{4}\chi^{(3)}_{xxxx}\left[3E_x(\omega)E_x(-\omega)E_x(\omega)+\frac{6}{3}E_y(\omega)E_y(-\omega)E_x(\omega)+E_y(\omega)E_y(\omega)E_x(-\omega)\right].
\end{aligned}$$

Eq. (A.2.1) was used in the last line, and below we drop the subscript on $\chi^{(3)}_{xxxx}$ and write $\chi^{(3)}$ instead. The y-component is found in the same way or by interchanging x and y in the above expression

$$\begin{aligned}
P^{(3)}_y(\omega) = \frac{1}{4}\chi^{(3)}\big[&3E_y(\omega)E_y(-\omega)E_y(\omega) + 2E_x(\omega)E_x(-\omega)E_y(\omega)+\\
&E_x(\omega)E_x(\omega)E_y(-\omega)\big].
\end{aligned}$$

To further simply notation, we write $E_x = E_x(\omega)$, $E_x^* = E_x(-\omega)$. To write the result on vector form, the terms are rearranged as

$$\begin{aligned} P_x^{(3)} &= \frac{1}{4}\chi^{(3)}\left[2(E_xE_x^* + E_yE_y^*)E_x + (E_xE_x + E_yE_y)E_x^*\right] \\ P_y^{(3)} &= \frac{1}{4}\chi^{(3)}\left[2(E_yE_y^* + E_xE_x^*)E_y + (E_yE_y + E_xE_x)E_y^*\right] \quad \Rightarrow \\ \mathbf{P}^{(3)} &= \frac{1}{4}\chi^{(3)}\left[2(\mathbf{E}\cdot\mathbf{E}^*)\mathbf{E} + (\mathbf{E}\cdot\mathbf{E})\mathbf{E}^*\right]. \end{aligned}$$

This result is inserted in Eq. (3.3.2)

$$\nabla\times\nabla\times\mathbf{E} - \frac{\omega^2}{c^2}\epsilon_r(\mathbf{r})\mathbf{E} = \frac{\omega^2}{c^2}\frac{1}{4}\chi^{(3)}\left[2\left(\mathbf{E}\cdot\mathbf{E}^*\right)\mathbf{E} + \left(\mathbf{E}\cdot\mathbf{E}\right)\mathbf{E}^*\right].$$

The nonlinear polarization term is now considered a perturbation and the field and eigenfrequency are expanded according to Eq. (3.2.1). Again, writing out all terms proportional to ζ, we have

$$\begin{aligned} \nabla\times\nabla\times\mathbf{E}^{(1)} - \frac{2\tilde{\omega}^{(0)}\tilde{\omega}^{(1)}}{c^2}\epsilon_r(\mathbf{r})\mathbf{E}^{(0)} - \frac{(\tilde{\omega}^{(0)})^2}{c^2}\epsilon_r(\mathbf{r})\mathbf{E}^{(1)} = \\ \frac{(\tilde{\omega}^{(0)})^2}{c^2}\frac{1}{4}\chi^{(3)}\left[2\left(\mathbf{E}^{(0)}\cdot\mathbf{E}^{(0)^*}\right)\mathbf{E}^{(0)} + \left(\mathbf{E}^{(0)}\cdot\mathbf{E}^{(0)}\right)\mathbf{E}^{(0)^*}\right]. \end{aligned}$$

Taking the dot product of both sides with $\mathbf{E}^{(0)}$ and integrating, we get

$$\begin{aligned} \int_V \mathbf{E}^{(0)}\cdot\left[\nabla\times\nabla\times - \frac{(\tilde{\omega}^{(0)})^2}{c^2}\epsilon_r(\mathbf{r})\right]\mathbf{E}^{(1)}dV = \frac{2\tilde{\omega}^{(0)}\tilde{\omega}^{(1)}}{c^2}\int_V \epsilon_r\mathbf{E}^{(0)}\cdot\mathbf{E}^{(0)}dV \\ + \frac{(\tilde{\omega}^{(0)})^2}{c^2}\int_V \frac{1}{4}\chi^{(3)}\left[2\left(\mathbf{E}^{(0)}\cdot\mathbf{E}^{(0)^*}\right)\mathbf{E}^{(0)}\cdot\mathbf{E}^{(0)} + \left(\mathbf{E}^{(0)}\cdot\mathbf{E}^{(0)}\right)\mathbf{E}^{(0)^*}\cdot\mathbf{E}^{(0)}\right]dV, \end{aligned}$$

which may be compared with Eq. (A.1.1) to identify the perturbation as

$$\Delta\epsilon_{\mathrm{r}} = \frac{3}{4}\chi^{(3)}|\mathbf{E}^{(0)}|^2\mathbf{E}^{(0)}\cdot\mathbf{E}^{(0)}. \tag{A.2.3}$$

Using Eq. (A.1.4), we may then write the result directly as

$$\tilde{\omega}^{(1)} = -\frac{3}{8}\tilde{\omega}^{(0)}\frac{\int_V \chi^{(3)}|\mathbf{E}^{(0)}|^2\mathbf{E}^{(0)}\cdot\mathbf{E}^{(0)}dV}{\int_V \epsilon_{\mathrm{r}}(\mathbf{r})\mathbf{E}^{(0)}\cdot\mathbf{E}^{(0)}dV + i\frac{c\sqrt{\epsilon_{\mathrm{B}}}}{2\tilde{\omega}^{(0)}}\int_{\partial V}\left(\mathbf{E}^{(0)}\cdot\mathbf{E}^{(0)}\right)\hat{\mathbf{r}}\cdot d\mathbf{A}}. \tag{A.2.4}$$

A.3 Two Electric Fields

For mulit-mode cavities, it is necessary to consider the case, where there are two terms in Eq. (2.2.3), one oscillating at ω_1 and the other oscillating at ω_2. As in the previous section, we will use a shorthand notation such that $E_{1i} = E_i(\omega_1)$ and $E_{1i}^* = E_i(-\omega_1)$ and likewise for ω_2. We focus on the part

of the polarization, which oscillates at ω_1 and proceed as before. The terms oscillating at ω_1 are

$$\begin{aligned}
P_x^{(3)}(\omega_1) = \; & \frac{1}{4}\chi^{(3)}_{xxxx}\left[E_{1x}E_{1x}E^*_{1x} + E_{1x}E^*_{1x}E_{1x} + E^*_{1x}E_{1x}E_{1x} + E_{2x}E^*_{2x}E_{1x} + \right. \\
& E^*_{2x}E_{2x}E_{1x} + E_{2x}E_{1x}E^*_{2x} + E^*_{2x}E_{1x}E_{2x} + E_{1x}E_{2x}E^*_{2x} + E_{1x}E^*_{2x}E_{2x}\left.\right] + \\
& \frac{1}{4}\chi^{(3)}_{xxyy}\left[E_{1x}E_{1y}E^*_{1y} + E_{1x}E^*_{1y}E_{1y} + E^*_{1x}E_{1y}E_{1y} + E_{2x}E^*_{2y}E_{1y} + \right. \\
& E^*_{2x}E_{2y}E_{1y} + E_{2x}E_{1y}E^*_{2y} + E^*_{2x}E_{1y}E_{2y} + E_{1x}E_{2y}E^*_{2y} + E_{1x}E^*_{2y}E_{2y}\left.\right] + \\
& \frac{1}{4}\chi^{(3)}_{xyxy}\left[E_{1y}E_{1x}E^*_{1y} + E_{1y}E^*_{1x}E_{1y} + E^*_{1y}E_{1x}E_{1y} + E_{2y}E^*_{2x}E_{1y} + \right. \\
& E^*_{2y}E_{2x}E_{1y} + E_{2y}E_{1x}E^*_{2y} + E^*_{2y}E_{1x}E_{2y} + E_{1y}E_{2x}E^*_{2y} + E_{1y}E^*_{2x}E_{2y}\left.\right] + \\
& \frac{1}{4}\chi^{(3)}_{xyyx}\left[E_{1y}E_{1y}E^*_{1x} + E_{1y}E^*_{1y}E_{1x} + E^*_{1y}E_{1y}E_{1x} + E_{2y}E^*_{2y}E_{1x} + \right. \\
& \left. E^*_{2y}E_{2y}E_{1x} + E_{2y}E_{1y}E^*_{2x} + E^*_{2y}E_{1y}E_{2x} + E_{1y}E_{2y}E^*_{2x} + E_{1y}E^*_{2y}E_{2x}\right].
\end{aligned}$$

To keep an overview, some terms are collected

$$\begin{aligned}
P_x^{(3)}(\omega_1) = \; & \frac{1}{4}\chi^{(3)}_{xxxx}\left[3E_{1x}E_{1x}E^*_{1x} + 6E_{2x}E^*_{2x}E_{1x} + \right. \\
& \left. 2E_{1y}E^*_{1y}E_{1x} + E_{1y}E_{1y}E^*_{1x}\right] + \\
& \frac{1}{4}\chi^{(3)}_{xxyy}\left[E_{2x}E^*_{2y}E_{1y} + E^*_{2x}E_{2y}E_{1y} + E_{2x}E_{1y}E^*_{2y} + \right. \\
& E^*_{2x}E_{1y}E_{2y} + E_{1x}E_{2y}E^*_{2y} + E_{1x}E^*_{2y}E_{2y}\left.\right] + \\
& \frac{1}{4}\chi^{(3)}_{xyxy}\left[E_{2y}E^*_{2x}E_{1y} + E^*_{2y}E_{2x}E_{1y} + E_{2y}E_{1x}E^*_{2y} + \right. \\
& E^*_{2y}E_{1x}E_{2y} + E_{1y}E_{2x}E^*_{2y} + E_{1y}E^*_{2x}E_{2y}\left.\right] + \\
& \frac{1}{4}\chi^{(3)}_{xyyx}\left[E_{2y}E^*_{2y}E_{1x} + E^*_{2y}E_{2y}E_{1x} + E_{2y}E_{1y}E^*_{2x} + \right. \\
& \left. E^*_{2y}E_{1y}E_{2x} + E_{1y}E_{2y}E^*_{2x} + E_{1y}E^*_{2y}E_{2x}\right].
\end{aligned}$$

Collecting the remaining terms, the result simplifies to

$$\begin{aligned}
P_x^{(3)}(\omega_1) = \; & \frac{1}{4}\chi^{(3)}\left[3E_{1x}E_{1x}E^*_{1x} + 2E_{1y}E^*_{1y}E_{1x} + E_{1y}E_{1y}E^*_{1x} + \right. \\
& \left. 6E_{2x}E^*_{2x}E_{1x} + 2E_{2y}E^*_{2y}E_{1x} + 2E_{2x}E^*_{2y}E_{1y} + 2E^*_{2x}E_{2y}E_{1y}\right].
\end{aligned}$$

Let us only concern ourselves with those terms that include both ω_1 and ω_2, and rearrange terms to make it easier to identify how to write the result in

vector form

$$\underbrace{P_x^{(3)}(\omega_1)}_{\text{mixed terms}} = \frac{1}{4}\chi^{(3)}\left[6E_{2x}E_{2x}^*E_{1x} + 2E_{2y}E_{2y}^*E_{1x} + 2E_{2x}E_{2y}^*E_{1y} + 2E_{2x}^*E_{2y}E_{1y}\right] =$$
$$\frac{1}{4}\chi^{(3)}\left[2(E_{2x}E_{2x}^* + E_{2y}E_{2y}^*)E_{1x} + 2(E_{2x}E_{1x} + E_{2y}E_{1y})E_{2x}^* + 2(E_{2x}^*E_{1x} + E_{2y}^*E_{1y})E_{2x}\right].$$

Utilizing that $P_y^{(3)}(\omega_1)$ is found from the above result by interchanging x and y in the subscripts, we have

$$\underbrace{P_y^{(3)}(\omega_1)}_{\text{mixed terms}} = \frac{1}{4}\chi^{(3)}\left[2(E_{2y}E_{2y}^* + E_{2x}E_{2x}^*)E_{1y} + 2(E_{2y}E_{1y} + E_{2x}E_{1x})E_{2y}^* + 2(E_{2y}^*E_{1y} + E_{2x}^*E_{1x})E_{2y}\right].$$

The result can thus be written as

$$\underbrace{\mathbf{P}^{(3)}(\omega_1)}_{\text{all terms}} = \frac{1}{4}\chi^{(3)}\left[2(\mathbf{E}_1\cdot\mathbf{E}_1^*)\mathbf{E}_1 + (\mathbf{E}_1\cdot\mathbf{E}_1)\mathbf{E}_1^* + 2(\mathbf{E}_2\cdot\mathbf{E}_2^*)\mathbf{E}_1 + 2(\mathbf{E}_1\cdot\mathbf{E}_2)\mathbf{E}_2^* + 2(\mathbf{E}_2^*\cdot\mathbf{E}_1)\mathbf{E}_2\right]. \quad \text{(A.3.1)}$$

Following the procedure from the previous section, we take the dot product of $\mathbf{P}^{(3)}$ with $\mathbf{E}^{(0)}$ and integrate. From Eqs. (A.2.3) and (A.2.4) it is seen that the results may be written directly as the sum of two terms

$$\frac{\tilde{\omega}_1^{(1)}}{\tilde{\omega}_1^{(0)}} = -\frac{3}{8}\frac{\int_V \chi^{(3)}|\mathbf{E}_1^{(0)}|^2(\mathbf{E}_1^{(0)}\cdot\mathbf{E}_1^{(0)})dV}{\int_V \epsilon_{\mathrm{r}}(\mathbf{r})\mathbf{E}_1^{(0)}\cdot\mathbf{E}_1^{(0)}dV + i\frac{c\sqrt{\epsilon_{\mathrm{B}}}}{2\tilde{\omega}_1^{(0)}}\int_{\partial V}\mathbf{E}_1^{(0)}\cdot\mathbf{E}_1^{(0)}dA} -$$
$$\frac{2}{8}\frac{\int \chi^{(3)}\left[|\mathbf{E}_2^{(0)}|^2(\mathbf{E}_1^{(0)}\cdot\mathbf{E}_1^{(0)}) + 2(\mathbf{E}_1^{(0)}\cdot\mathbf{E}_2^{(0)*})(\mathbf{E}_2^{(0)}\cdot\mathbf{E}_1^{(0)})\right]dV}{\int_V \epsilon_{\mathrm{r}}(\mathbf{r})\mathbf{E}_1^{(0)}\cdot\mathbf{E}_1^{(0)}dV + i\frac{c\sqrt{\epsilon_{\mathrm{B}}}}{2\tilde{\omega}_1^{(0)}}\int_{\partial V}\mathbf{E}_1^{(0)}\cdot\mathbf{E}_1^{(0)}dA}.$$

By inserting Eq. (2.2.8), the terms are written as

$$\tilde{\omega}_1^{(1)} = -\frac{3}{8}\tilde{\omega}_1^{(0)}|A_1(t)|^2\frac{\int_V \chi^{(3)}|\tilde{\mathbf{f}}_1|^2(\tilde{\mathbf{f}}_1\cdot\tilde{\mathbf{f}}_1)dV}{\int_V \epsilon_{\mathrm{r}}(\mathbf{r})\tilde{\mathbf{f}}_1\cdot\tilde{\mathbf{f}}_1dV + i\frac{c\sqrt{\epsilon_{\mathrm{B}}}}{2\tilde{\omega}_1^{(0)}}\int_{\partial V}\tilde{\mathbf{f}}_1\cdot\tilde{\mathbf{f}}_1dA} -$$
$$\frac{2}{8}\tilde{\omega}_1^{(0)}|A_2(t)|^2\frac{\int \chi^{(3)}\left[|\tilde{\mathbf{f}}_2|^2(\tilde{\mathbf{f}}_1\cdot\tilde{\mathbf{f}}_1) + 2(\tilde{\mathbf{f}}_1\cdot\tilde{\mathbf{f}}_2^*)(\tilde{\mathbf{f}}_2\cdot\tilde{\mathbf{f}}_1)\right]dV}{\int_V \epsilon_{\mathrm{r}}(\mathbf{r})\tilde{\mathbf{f}}_1\cdot\tilde{\mathbf{f}}_1dV + i\frac{c\sqrt{\epsilon_{\mathrm{B}}}}{2\tilde{\omega}_1^{(0)}}\int_{\partial V}\tilde{\mathbf{f}}_1\cdot\tilde{\mathbf{f}}_1dA},$$

and the first order correction to the eigenfrequency of mode 1 may be written as

$$\tilde{\omega}_1^{(1)} = (-K_{\text{Kerr}}^{11} - iK_{\text{TP}}^{11})|A_1(t)|^2 + (-K_{\text{Kerr}}^{12} - iK_{\text{TP}}^{12})|A_2(t)|^2.$$

In all the above calculations, the subscripts "1" and "2" could be replaced to calculate the corrections to $\tilde{\omega}_2$ from $\mathbf{E}_1$ and $\mathbf{E}_2$. We may thus write the general relations

$$K_{\text{Kerr}}^{jk} = \text{Re}\left\{\frac{\tilde{\omega}_j^{(0)}\chi^{(3)}}{\epsilon_0 V_{jk}}\right\},\ K_{\text{TP}}^{jk} = \text{Im}\left\{\frac{\tilde{\omega}_j^{(0)}\chi^{(3)}}{\epsilon_0 V_{jk}}\right\},\ (j,k) = (1,2). \qquad \text{(A.3.2)}$$

The complex characteristic volumes are defined by

$$\frac{1}{V_{jj}} = \frac{3}{8}\frac{\epsilon_0 \int_V f_\epsilon |\tilde{\mathbf{f}}_j|^2 (\tilde{\mathbf{f}}_j \cdot \tilde{\mathbf{f}}_j) dV}{\langle\langle \tilde{\mathbf{f}}_j | \tilde{\mathbf{f}}_j \rangle\rangle},$$

and

$$\frac{1}{V_{jk}} = \frac{2}{8}\frac{\epsilon_0 \int_V f_\epsilon \left[|\tilde{\mathbf{f}}_k|^2 (\tilde{\mathbf{f}}_j \cdot \tilde{\mathbf{f}}_j) + 2(\tilde{\mathbf{f}}_j \cdot \tilde{\mathbf{f}}_k^*)(\tilde{\mathbf{f}}_k \cdot \tilde{\mathbf{f}}_j)\right] dV}{\langle\langle \tilde{\mathbf{f}}_j | \tilde{\mathbf{f}}_j \rangle\rangle}.$$

Appendix B

FDTD Simulations

This appendix is devoted to a discussion of extracting linear parameters of the temporal coupled mode theory (TCMT) from finite difference time domain (FDTD) simulations. Two different implementations have been used in this thesis: A freely available code, which allows for Kerr nonlinearities [48] (referred to as MEEP), and a code developed by Yuriy Elesin at the Department of Mechanical Engineering at DTU [89] (referred to as PHAZOR). We have performed a comparison of using the two methods and the agreement for the considered structure was good. It is, however, not known to us whether the implementation of perfectly matched layers (PML) and index-averaging is identical for the two methods, so differences between the methods are expected in general. To solve Eq. (2.2.6), which is a frequency-domain equation, with a time-domain method, a transient source is used to excite the eigenmode. After the source is turned off, the excited cavity mode leaks energy into the surroundings while oscillating at the eigenfrequency. The electric field is then given by

$$\vec{\mathcal{E}}(\mathbf{r},t) = \frac{1}{2}\mathbf{E}_n e^{-i\tilde{\omega}_n t} + \frac{1}{2}\mathbf{E}_n^* e^{i\tilde{\omega}_n t}, \tag{B.0.1}$$

where the complex eigenfrequency is defined as $\tilde{\omega} = \omega_{\mathrm{C}} - i\gamma_{\mathrm{C}}$. If $\tilde{\omega}_n$ was real, it is easy to see that the eigenmode could be obtained by taking the Fourier transform of the real field in Eq. (B.0.1).

B.1 Eigenmodes

Let us show that this is also the case for a complex frequency. The discrete Fourier transform is evaluated in a time window $t \in [t_0; t_0 + Ndt]$ after the source has died out. In PHAZOR the discrete Fourier transform is defined as

$$\tilde{f}(\nu) = \sum_{n=0}^{N} f(t) \exp\left[-i2\pi\nu t_n\right], \quad t = t_0, t_0 + dt, \ldots, t_0 + Ndt. \tag{B.1.1}$$

The definition of the Fourier transform used in this thesis is

$$\mathcal{F}\{f(t)\} = f(\omega) = \int_{-\infty}^{+\infty} f(t)e^{i\omega t}dt \tag{B.1.2}$$

$$\mathcal{F}^{-1}\{f(\omega)\} = f(t) = \frac{1}{2\pi}\int_{-\infty}^{+\infty} f(\omega)e^{-i\omega t}d\omega\,, \tag{B.1.3}$$

which uses a different sign convention than Eq. (B.1.1). If it is assumed that the summation in Eq. (B.1.1) can be written as an integral and the integrand $f(t)$ equals the electric field from Eq. (2.2.3), but with a complex frequency $\tilde{\omega}_n$, the output from PHAZOR is given by

$$\begin{aligned}\vec{\mathcal{E}}(\mathbf{r},\omega) &= \int_{t_0}^{t_1}\frac{1}{2}\left(\mathbf{E}_n e^{-i\tilde{\omega}_n t} + \mathbf{E}_n^* e^{i\tilde{\omega}_n t}\right)e^{-i\omega t}dt \\ \vec{\mathcal{E}}(\mathbf{r},\omega) &= \frac{1}{2}\frac{\mathbf{E}_n\left[e^{-[\gamma_C + i(\omega+\tilde{\omega}_n)]t_1} - e^{-[\gamma_C + i(\omega+\tilde{\omega}_n)]t_0}\right]}{-\gamma_C - i(\omega+\tilde{\omega}_n)} + \\ &\qquad \frac{1}{2}\frac{\mathbf{E}_n^*\left[e^{-[\gamma_C + i(\omega-\tilde{\omega}_n)]t_1} - e^{-[\gamma_C + i(\omega-\tilde{\omega}_n)]t_0}\right]}{-\gamma_C - i(\omega-\tilde{\omega}_n)}.\end{aligned}$$

In Eq. (B.1.1) the summation must be carried out for each frequency of interest. Using the resonance frequency $\tilde{\nu}_n$, we get

$$\begin{aligned}\vec{\mathcal{E}}(\mathbf{r},\tilde{\omega}_n) = \frac{1}{2}\frac{\mathbf{E}_n\left[e^{-[\gamma_C + i2\tilde{\omega}_n]t_1} - e^{-[\gamma_C + i2\tilde{\omega}_n]t_0}\right]}{-\gamma_C - i2\tilde{\omega}_n} + \frac{1}{2}\frac{\mathbf{E}_n^*\left[e^{-\gamma_C t_1} - e^{-\gamma_C t_0}\right]}{-\gamma_C} \approx \\ \frac{1}{2}\frac{\mathbf{E}_n^*\left[e^{-\gamma_C t_1} - e^{-\gamma_C t_0}\right]}{-\gamma_C}.\end{aligned}$$

It is thus seen that

$$\vec{\mathcal{E}}(\mathbf{r},\tilde{\omega}_n) \propto \mathbf{E}_n^* \quad \text{and} \quad \vec{\mathcal{E}}^*(\mathbf{r},\tilde{\omega}_n) \propto \mathbf{E}_n.$$

Since the normalization in Eq. (2.2.10) is used to find the mode function $\tilde{\mathbf{f}}_n$ that is used in the perturbation theory in Chapter 3, the output from PHAZOR only needs to be proportional to $\mathbf{E}_n$.

B.2 Complex Eigenfrequency

To extract the complex eigenfrequency, the electric or magnetic field is monitored in a single point as a function of time in an interval $t \in [t_1, t_2]$ after the source is gone. The output from the FDTD simulation has the form

$$f(t) = e^{[-\Gamma t - i\omega_0 t]}\left[\theta(t-t_1) - \theta(t-t_2)\right], \tag{B.2.1}$$

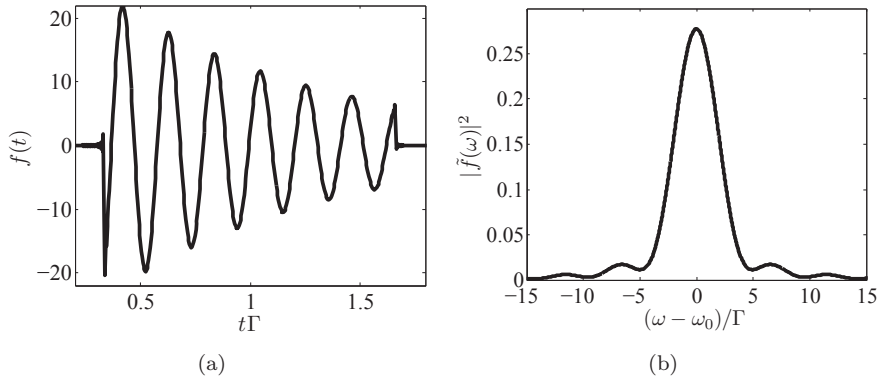

Figure B.1: (a) A plot of the function $f(t)$ in Eq. (B.2.1). (b) A plot of the function $|\tilde{f}(\omega)|^2$ in Eq. (B.2.3).

where $\theta(t)$ is the step function. It is illustrated in Fig. B.1(a). If only a single resonance is excited, one may simply fit the output from FDTD with the decaying exponential in Eq. (B.2.1). If the data is a superposition of decaying fields from different resonances, the Fourier transform of Eq. (B.2.1) may be used to distinguish between the resonances in the frequency-domain. Including only one step function, the Fourier transform is known [76]

$$f_L(t) = e^{[-\Gamma t - i\omega_0 t]}\theta(t) \qquad \tilde{f}_L(\omega) = \frac{1}{\Gamma - i(\omega - \omega_0)}.$$

Looking at just one of the terms in $f(t)$

$$f_1(t) = e^{[-\Gamma t - i\omega_0 t]}\theta(t - t_1)$$

and defining the function

$$g(t) = f_1(t + t_1) = e^{[-\Gamma t_1 - i\omega_0 t_1]}e^{[-\Gamma t - i\omega_0 t]}\theta(t),$$

it is seen that the Fourier transform of $g(t)$ is

$$\tilde{g}(\omega) = e^{[-\Gamma t_1 - i\omega_0 t_1]}\frac{1}{\Gamma - i(\omega - \omega_0)}.$$

Using the identity [76]

$$\mathcal{F}\{f(t)e^{i\omega_0 t}\} = f(\omega + \omega_0), \qquad \mathcal{F}^{-1}\{f(\omega)e^{it_0\omega}\} = f(t - t_0)\,, \tag{B.2.2}$$

the transform of $f_1(t)$ is

$$f_1(t) = g(t - t_1) \quad \Rightarrow \quad \tilde{f}_1(\omega) = \mathcal{F}\{g(t - t_1)\} = \mathcal{F}\{\mathcal{F}^{-1}\{\tilde{g}(\omega)e^{[i\omega t_1]}\}\} \quad \Rightarrow$$
$$\tilde{f}_1(\omega) = e^{[-\Gamma t_1 + i(\omega - \omega_0)t_1]}\frac{1}{\Gamma - i(\omega - \omega_0)}.$$

By adding the second term of $f(t)$, its Fourier transform is

$$\tilde{f}(\omega) = \frac{1}{\Gamma - i(\omega - \omega_0)} \left[e^{[-\Gamma t_1 + i(\omega-\omega_0)t_1]} - e^{[-\Gamma t_2 + i(\omega-\omega_0)t_2]} \right]$$

$$|\tilde{f}(\omega)|^2 = \frac{\exp[-2\Gamma t_1] + \exp[-2\Gamma t_2]}{\Gamma^2 + (\omega - \omega_0)^2} - \frac{2\exp[-\Gamma(t_2 + t_1)]\cos[(\omega - \omega_0)(t_2 - t_1)]}{\Gamma^2 + (\omega - \omega_0)^2}. \quad \text{(B.2.3)}$$

A plot of Eq. (B.2.3) is shown in Fig. B.1(b) corresponding to the function $f(t)$ shown in Fig. B.1(a). By Fourier transforming the output from FDTD and fitting to Eq. (B.2.3) locally around each peak in the spectrum, it is possible to determine multiple resonance frequencies and decay rates from a single FDTD time trace.

B.3 Transmission Spectrum

In Appendix B.2 it was shown how to extract the complex eigenfrequency by monitoring the field in a single point. In this section, we discuss how the transmission spectrum of the structures may be obtained. One approach is illustrated in Fig. B.2. The details of this structure are treated in Section 8.2. A broadband source is placed at the red circles and the power spectrum passing through the surfaces indicated by solid red or blue lines is monitored. To get the input spectrum, the power passing through the input plane, indicated by the solid red line in Fig. B.2(b), is monitored and the transmission spectrum is obtained by taking the ratio of the output- and input spectrum. The auxiliary structure in Fig. B.2(b) is needed, because the input spectrum cannot by measured in Fig. B.2(a) directly, due to back reflections originating from the structure. The size of the planes used to monitor the power must be chosen according to the discussion in Section 3.3.1.

In general, an auxiliary structure must be constructed, such that the input spectrum may be monitored with the smallest possible amount of back reflection. There may not be a unique way of choosing such a structure, and Fig. B.3 shows an alternative auxiliary structure, which may be used in combination with Fig. B.2(a). We shall refer to the use of Fig. B.2(a) with the structure in Fig. B.2(b) as the reference as method 1, and the use of Fig. B.3 as the reference structure as method 2. Alternatively, one could let the photonic crystal (PC) waveguide extend throughout the calculation domain to remove these reflections. However, reflections from the PML boundary condition used in FDTD are difficult to suppress for a non-homogeneous medium in the PML region. It is thus not a trivial task to obtain the transmission spectrum of the cavity alone.

It is important to place the source sufficiently far away from the input plane, because the power passing through this surface must equal the power passing

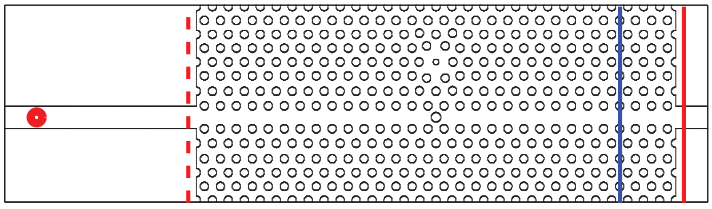

(a)

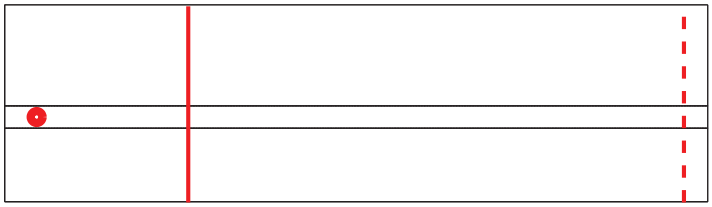

(b)

Figure B.2: Illustration of procedure for calculating transmission spectra. (a) The actual structure, from which the output spectra are calculated. (b) Auxiliary structure used to obtain the input power spectra. A transmission calculation using this structure with that in (a) is referred to as method 1. Power spectra are calculated through surfaces indicated by the solid red lines and sources are placed at the red circles. The blue line in (a) corresponds to the auxiliary structure in Fig. B.3.

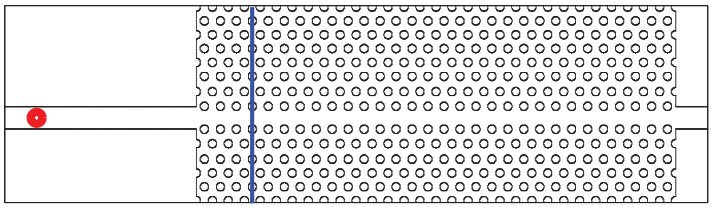

Figure B.3: Illustration of an alternative auxiliary structure to that in Fig. B.2(b) consisting of only a PC waveguide. A transmission calculation using this structure with that in Fig. B.2(a) is referred to as method 2.

through the surface indicated by the dashed red line. Or, put another way, the source must be sufficiently far away, such that the transmission becomes independent of its distance to the input plane.

We expect future generation structures to be embedded in some low index material (other than air) due to the possible improvements in temperature insensitivity of such devices. These structures also enable the access waveguides

to be formed as strip waveguides as in the figures of this section. Such waveguides exhibit lower propagation loss, which is another advantage of embedded structures. In such a case, the reflections from the interfaces are no longer a computational issue, but a property of the real device and tapers at the facets may be needed [49].

B.4 Convergence

The focus of this thesis is not on numerical techniques, and they are used primarily as tools for device design. For such purposes, it is not of particular importance to have good estimates of the numerical precision. The key issue is whether the fabricated structures based on these designs have properties similar to the designed structures. Exact matching of e.g. resonance frequency and quality factor cannot be expected due to fabrication uncertainties, and deviations in resonant wavelengths on the order of 10nm are acceptable.

When using the numerical techniques to investigate the validity of simpler models such as the TCMT, the accuracy becomes more critical. A comparison

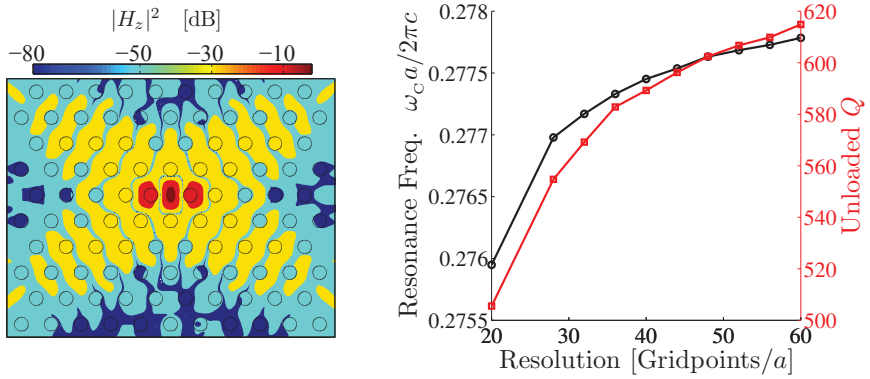

Figure B.4: Convergence test. (a) The structure considered consisting of an H0 cavity in a finite sized PC membrane. The parameters are: $d = 0.8a$, $r = 0.23a$, and $\delta x = 0.16a$. (b) Resonance frequency and quality factor as a function of resolution measured in grid points per lattice constant.

of transmission spectra in Fig. 8.10(b) is, in principle, difficult to make sense of, unless some error estimate on the FDTD results are known. This requires a convergence test, which should be performed for every structure being considered. For 3D FDTD simulations, this is basically an insurmountable task due to the simulation time it would require. To have at least some idea of the convergence properties of the method for the type of structure, we are considering, we have calculated the eigenfrequency of the structure shown in Fig. B.4(a)

for different resolutions using PHAZOR. The result is shown in Fig. B.4(b). A clear tendency is observed for both the real part of the frequency and the Q factor, but their values have not converged within the resolution interval shown in Fig. B.4. The calculation time for the highest resolution is about 24 hours on 144 cores connected with infiniband. The mode profile shows no qualitative changes when increasing the resolution and the decay of the cavity field is well approximated by and exponential. Thus, we assume that the transmission spectra considered in e.g. Fig. 8.10(b) would exhibit the same qualitative behavior if they were calculated using a higher resolution. The TCMT is therefore still expected to show a good agreement with the FDTD result, if the parameters in the model are modified slightly. We note that all FDTD simulations in this thesis have been performed with a resolution of 20 grid points per lattice constant.

Appendix C

MPB Simulations

This appendix contains a brief investigation of the convergence properties of simulations using the freely available software called MBP [15]. We shall not go into details with the plane wave expansion method, but simply show a calculation of the dispersion of the even mode of a line-defect waveguide as in Fig. 1.3(a) for different resolutions of the discretization of the computation domain.

C.1 Convergence

In Fig. C.1 we show the dependence of the dispersion curve of a line-defect waveguide mode on the resolution of the discretization used in the computation. It is observed that the absolute value of the frequency depends on the

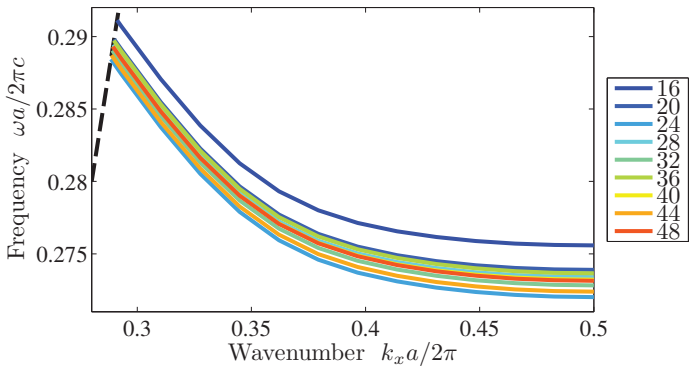

Figure C.1: Band diagram of a line-defect waveguide for different resolutions of the discretization used in the calculation. The parameters of the structure are: $d = 0.8a$, $r_0 = 0.26a$, $l_{1p} = 0.15a$, $l_{2p} = 0.1a$, and $l_{1l} = 0$. The resolution is measured in grid points per lattice constant as in Fig. B.4(b).

resolution as in the case of finite difference time domain (FDTD) simulations. The qualitative features of the dispersion are the same regardless of the resolution, which provides confidence that we may use a resolution of e.g. 20 grid points per lattice for calculations intended structure design. This is the resolution used in all MPB simulations throughout this thesis.

Appendix D

Experiment and Model Comparison

This appendix contains some additional figures to support the discussions in Section 5.4.

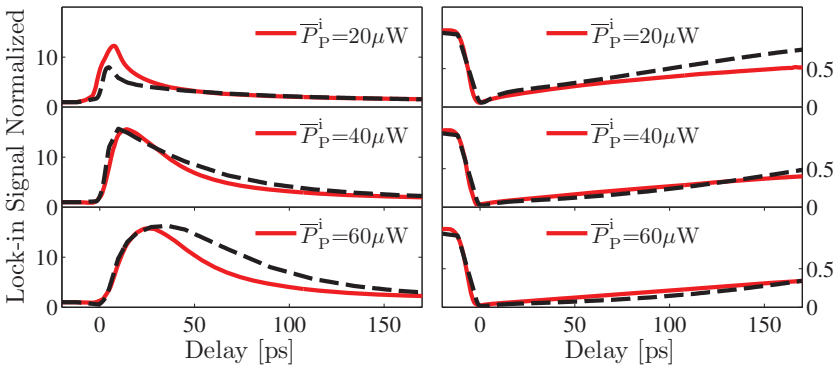

Figure D.1: Comparison of data from Fig. 5.9 with simulations using Eq. (5.4.7) by fitting to the time-domain data only. The data is the same as in Fig. 5.12.

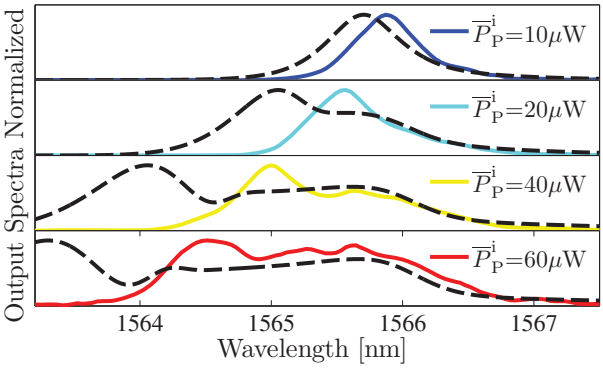

Figure D.2: Comparison of data from Fig. 5.9 with simulations using Eq. (5.4.7) by fitting to the time-domain data only. The data is the same as in Fig. 5.13.

Model Parameters

$\partial\epsilon_{\mathrm{FCD}}/\partial N_1$	=	-6.16×10^{-26} m^3	V_1/V_2	=	0.89
$\partial\epsilon_{\mathrm{FCA}}/\partial N_1$	=	5.26×10^{-27} m^3	$1/\gamma_{\mathrm{diff}}$	=	8ps
Im $\{\chi^{(3)}\}$	=	5.46×10^{-18} m^2/V^2	$1/\gamma_{\mathrm{nr}}$	=	150ps
Re $\{\chi^{(3)}\}$	=	2.80×10^{-18} m^2/V^2	$\gamma_1/\gamma_{\mathrm{C}}$	=	0.98
V_1	=	0.92 $(\lambda_{\mathrm{C}}/n_{\mathrm{R}})^3$	T_{coup}	=	0.06
V_χ	=	(280-i38)×$(\lambda_{\mathrm{C}}/n_{\mathrm{R}})^3$	$\zeta_{\mathrm{N_1}}$	=	0.0213 + i0.0017
α_{TPA}	=	123cm/GW	σ_{FCA}	=	0.23×10^{-17}cm^2

Table D.1: Model parameter values found by fitting to the time-domain measurements only.

Model Parameters

$\partial\epsilon_{\mathrm{FCD}}/\partial N_1$	=	-3.30×10^{-26} m^3	V_1/V_2	=	1.38
$\partial\epsilon_{\mathrm{FCA}}/\partial N_1$	=	1.05×10^{-26} m^3	$1/\gamma_{\mathrm{diff}}$	=	6ps
Im $\{\chi^{(3)}\}$	=	5.46×10^{-18} m^2/V^2	$1/\gamma_{\mathrm{nr}}$	=	175ps
Re $\{\chi^{(3)}\}$	=	2.80×10^{-18} m^2/V^2	$\gamma_1/\gamma_{\mathrm{C}}$	=	0.98
V_1	=	0.92 $(\lambda_{\mathrm{C}}/n_{\mathrm{R}})^3$	T_{coup}	=	0.06
V_χ	=	(280-i38)×$(\lambda_{\mathrm{C}}/n_{\mathrm{R}})^3$	$\zeta_{\mathrm{N_1}}$	=	0.0213 + i0.0017
α_{TPA}	=	123cm/GW	σ_{FCA}	=	0.47×10^{-17}cm^2

Table D.2: Model parameter values found by fitting to the spectral measurements only.

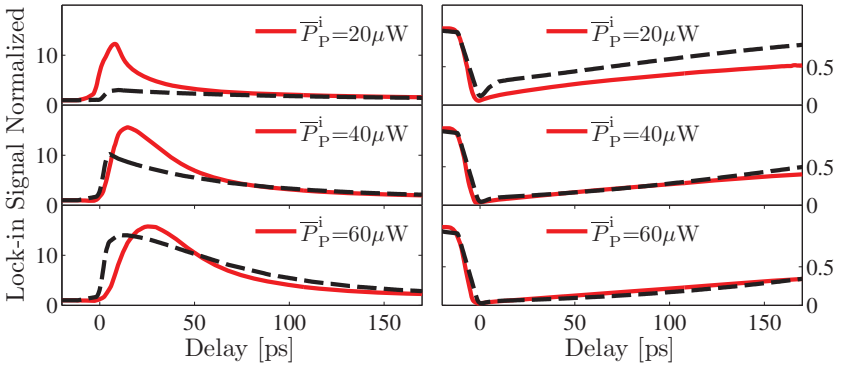

Figure D.3: Comparison of data from Fig. 5.9 with simulations using Eq. (5.4.7) by fitting to the spectral data only. The data is the same as in Fig. 5.12.

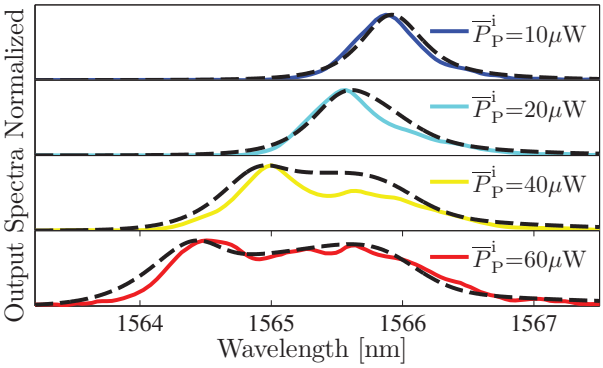

Figure D.4: Comparison of data from Fig. 5.9 with simulations using Eq. (5.4.7) by fitting to the spectral data only. The data is the same as in Fig. 5.13.

Appendix E

List of Acronyms

TCMT temporal coupled mode theory

FDTD finite difference time domain

PDE partial differential equation

ODE ordinary differential equation

RHS right hand side

LHS left hand side

BPF bandpass filter

PC photonic crystal

SOA semiconductor optical amplifier

WDM wavelength division multiplexing

OTDM optical time division multiplexing

FWHM full width at half maximum

TPA two photon absorption

FCD free carrier dispersion

FCA free carrier absorption

PRBS pseudo random binary signal

CW continuous wave

AOM acousto optic modulator

PML perfectly matched layers

Appendix F

Bibliography

[1] D. A. B. Miller, "Device Requirements for Optical Interconnects to Silicon Chips," *Proceedings of the IEEE*, vol. 97, pp. 1166–1185, July 2009.

[2] D. A. B. Miller, "The Roles of Optics in Information Processing," in *Advanced Photonics Congress, OSA*, no. i, pp. 1–3, 2012.

[3] M. Hilbert and P. López, "The World's Technological Capacity to Store, Communicate, and Compute Information," *Science*, vol. 332, pp. 60–65, 2011.

[4] D. A. B. Miller, "Are optical transistors the logical next step?," *Nature Photonics*, vol. 4, pp. 3–5, Jan. 2010.

[5] H. J. Caulfield and S. Dolev, "Why future supercomputing requires optics," *Nature Photonics*, vol. 4, pp. 261–263, May 2010.

[6] D. A. B. Miller, "The role of optics in computing," *Nature Photonics*, vol. 4, p. 2010, 2010.

[7] J. Caulfield and S. Dolev, "The role of optics in computing," *Nature Photonics*, vol. 4, pp. 406–407, July 2010.

[8] P. J. Winzer and R.-J. Essiambre, "Advanced Modulation Formats for High-Capacity Optical Transport Networks," *Journal of Applied Physics*, vol. 24, no. 12, pp. 4711–4728, 2006.

[9] R. C. Jaeger, *Microelectronic Circuit Design*. McGraw-Hill, first ed., 1996.

[10] E. Yablonovitch, "Inhibited Spontaneous Emission in Solid-State Physics and Electronics," *Physical Review Letters*, vol. 58, no. 20, pp. 2059–2062, 1987.

[11] S. John, "Strong localization of photons in certain disordered dielectric superlattices," *Physical Review Letters*, vol. 58, no. 23, pp. 2486–2489, 1987.

[12] S. Elliott, *The Physics and Chemistry of Solids*. John Wiley & Sons, Inc., third ed., 2005.

[13] J. D. Joannopoulos, S. G. Johnson, J. N. Winn, and R. D. Meade, *Photonic Crystals, Molding the Flow of Light*. Princeton University Press, second ed., 2008.

[14] S. McNab, N. Moll, and Y. Vlasov, "Ultra-low loss photonic integrated circuit with membrane-type photonic crystal waveguides.," *Optics Express*, vol. 11, pp. 2927–39, Nov. 2003.

[15] S. Johnson and J. Joannopoulos, "Block-iterative frequency-domain methods for Maxwell's equations in a planewave basis," *Optics Express*, vol. 8, p. 173, Jan. 2001.

[16] S. Johnson, P. Villeneuve, S. Fan, and J. Joannopoulos, "Linear waveguides in photonic-crystal slabs," *Physical Review B*, vol. 62, pp. 8212–8222, Sept. 2000.

[17] Z. Zhang and M. Qiu, "Small-volume waveguide-section high Q microcavities in 2D photonic crystal slabs.," *Optics Express*, vol. 12, pp. 3988–95, Aug. 2004.

[18] Y. Akahane, T. Asano, B. Song, and S. Noda, "High-Q photonic nanocavity in a two-dimensional photonic crystal," *Nature*, vol. 425, no. October, pp. 4–7, 2003.

[19] M. Soljacić and J. D. Joannopoulos, "Enhancement of nonlinear effects using photonic crystals.," *Nature Materials*, vol. 3, pp. 211–9, Apr. 2004.

[20] P. T. Kristensen, C. Van Vlack, and S. Hughes, "Generalized effective mode volume for leaky optical cavities.," *Optics Letters*, vol. 37, pp. 1649–51, May 2012.

[21] J. Y. Lee, L. Yin, G. P. Agrawal, and P. M. Fauchet, "Ultrafast optical switching based on nonlinear polarization rotation in silicon waveguides.," *Optics Express*, vol. 18, pp. 11514–23, May 2010.

[22] M. Waldow, T. Plötzing, M. Gottheil, M. Först, J. Bolten, T. Wahlbrink, and H. Kurz, "25ps all-optical switching in oxygen implanted silicon-on-insulator microring resonator," *Optics Express*, vol. 16, no. 11, pp. 2254–2256, 2008.

[23] C. Husko, A. De Rossi, S. Combrié, Q. V. Tran, F. Raineri, and C. W. Wong, "Ultrafast all-optical modulation in GaAs photonic crystal cavities," *Applied Physics Letters*, vol. 94, no. 2, p. 021111, 2009.

[24] K. Nozaki, T. Tanabe, A. Shinya, S. Matsuo, T. Sato, H. Taniyama, and M. Notomi, "Sub-femtojoule all-optical switching using a photonic-crystal nanocavity," *Nature Photonics*, vol. 4, no. May, pp. 477–483, 2010.

[25] L. O'Faolain, D. M. Beggs, T. P. White, T. Kampfrath, K. Kuipers, and T. F. Krauss, "Compact Optical Switches and Modulators Based on Dispersion Engineered Photonic Crystals," *IEEE Photonics Journal*, vol. 2, pp. 404–414, June 2010.

[26] R. J. Manning, a. D. Ellis, a. J. Poustie, and K. J. Blow, "Semiconductor laser amplifiers for ultrafast all-optical signal processing," *Journal of the Optical Society of America B*, vol. 14, p. 3204, Nov. 1997.

[27] S. Nakamura, Y. Ueno, and K. Tajima, "Femtosecond switching with semiconductor-optical-amplifier-based Symmetric Mach-Zehnder-type All-optical Switch," *Applied Physics Letters*, vol. 78, no. 25, p. 3929, 2001.

[28] O. Wada, "Recent Progress in Semiconductor-Based Photonic Signal-processing Devices," *IEEE Journal of Selected Topics in Quantum Electronics*, vol. 17, no. 2, pp. 309–319, 2011.

[29] A. I. Siahlo, L. K. Oxenløwe, K. S. Berg, A. T. Clausen, P. A. Andersen, C. Peucheret, A. Tersigni, P. Jeppesen, K. P. Hansen, and J. R. Folkenberg, "A High-Speed Demultiplexer Based on a Nonlinear Optical Loop Mirror With a Photonic Crystal Fiber," *IEEE Photonics Technology Letters*, vol. 15, no. 8, pp. 1147–1149, 2003.

[30] P. A. Andrekson, H. Sunnerud, S. Oda, T. Nishitani, and J. Yang, "Ultrafast, atto-Joule switch using fiber-optic parametric amplifier operated in saturation.," *Optics Express*, vol. 16, pp. 10956–61, July 2008.

[31] D. M. Beggs, T. P. White, L. O'Faolain, and T. F. Krauss, "Ultracompact and low-power optical switch based on silicon photonic crystals," *Optics Letters*, vol. 33, pp. 147–9, Jan. 2008.

[32] L. H. Frandsen, A. V. Lavrinenko, J. Fage-Pedersen, and P. I. Borel, "Photonic crystal waveguides with semi-slow light and tailored dispersion properties," *Optics Express*, vol. 14, pp. 9444–50, Oct. 2006.

[33] M. Santagiustina, C. G. Someda, G. Vadala, S. Combrié, and A. D. Rossi, "Theory of slow light enhanced four-wave mixing in photonic crystal waveguides," *Optics Express*, vol. 18, no. 20, pp. 21024–21029, 2010.

[34] R. W. Boyd, *Nonlinear Optics*. Academic Press, third ed., 2008.

[35] B. R. Bennett, R. A. Soref, and J. A. Del Alamo, "Carrier-Induced Change in Refractive Index of InP , GaAs , and InGaAsP," *IEEE Journal of Quantum Electronics*, vol. 26, no. 1, 1990.

[36] D. Englund, A. Faraon, I. Fushman, N. Stoltz, P. Petroff, and J. Vuković, "Controlling cavity reflectivity with a single quantum dot," *Nature*, vol. 450, pp. 857–61, Dec. 2007.

[37] H. M. Lai, P. T. Leung, K. Young, P. W. Barber, and S. C. Hill, "Time-independent Perturbation for Leaking Electromagnetic Modes in Open Systems with Apllication to Resonances in Microdroplets," *Physical Review A*, vol. 41, no. 9, pp. 5187–5198, 1990.

[38] K. M. Lee, P. T. Leung, and K. M. Pang, "Dyadic Formulation of Morphology-dependent Resonances . I . Completeness Relation," *Journal of the Optical Society of America B*, vol. 16, no. 9, pp. 1409–1417, 1999.

[39] K. M. Lee, P. T. Leung, and K. M. Pang, "Dyadic Formulation of Morphology-dependent Resonances . II . Perturbation Theory," *Journal of the Optical Society of America B*, vol. 16, no. 9, pp. 1418–1430, 1999.

[40] S. Fan, "Sharp asymmetric line shapes in side-coupled waveguide-cavity systems," *Applied Physics Letters*, vol. 80, no. 6, p. 908, 2002.

[41] J. D. Jackson, *Classical Electrodynamics*. John Wiley & Sons, Inc., third ed., 1999.

[42] P. A. Martin, *Multiple Scattering - Interaction of Time-Harmonic Waves with N Obstacles*. Cambridge University Press, first ed., 2006.

[43] D. J. Griffiths, *Introduction to Electrodynamics*. Prentice Hall International, Inc., third ed., 1999.

[44] W. Suh, S. Member, Z. Wang, and S. Fan, "Temporal Coupled-Mode Theory and the Presence of Non-Orthogonal Modes in Lossless Multimode Cavities," *IEEE Journal of Quantum Electronics*, vol. 40, no. 10, pp. 1511–1518, 2004.

[45] H. A. Haus, *Waves and Fields in Optoelectronics*. Prentice Hall International, Inc., 1984.

[46] J. Bravo-Abad, S. Fan, S. G. Johnson, J. D. Joannopoulos, and M. Soljacic, "Modeling Nonlinear Optical Phenomena in Nanophotonics," *Journal of Lightwave Technology*, vol. 25, no. 9, pp. 2539–2546, 2007.

[47] E. Waks and J. Vuckovic, "Coupled mode theory for photonic crystal cavity-waveguide interaction," *Optics Express*, vol. 13, pp. 5064–5073, June 2005.

[48] A. F. Oskooi, D. Roundy, M. Ibanescu, P. Bermel, J. Joannopoulos, and S. G. Johnson, "Meep: A flexible free-software package for electromagnetic simulations by the FDTD method," *Computer Physics Communications*, vol. 181, pp. 687–702, Mar. 2010.

[49] Q. V. Tran, S. Combrié, P. Colman, and A. De Rossi, "Photonic crystal membrane waveguides with low insertion losses," *Applied Physics Letters*, vol. 95, no. 6, p. 061105, 2009.

[50] T. Tanabe, H. Taniyama, and M. Notomi, "Carrier Diffusion and Recombination in Photonic Crystal Nanocavity Optical Switches," *Journal of Lightwave Technology*, vol. 26, no. 11, pp. 1396–1403, 2008.

[51] A. Mecozzi and J. Mørk, "Theory of heterodyne pump-probe experiments with femtosecond pulses," *Journal of the Optical Society of America B*, vol. 13, p. 2437, Nov. 1996.

[52] T. Katayama and H. Kawaguchi, "Measurement of self- and cross-gain saturation dynamics using two-color heterodyne pump-probe technique," *IEEE Photonics Technology Letters*, vol. 17, pp. 1244–1246, June 2005.

[53] J. H. Scofield, "Frequency-domain description of a lock-in amplifier," *American Journal of Physics*, vol. 62, no. 2, p. 129, 1994.

[54] R. Soref and B. Bennett, "Electrooptical effects in silicon," *IEEE Journal of Quantum Electronics*, vol. 23, pp. 123–129, Jan. 1987.

[55] Http://www.ioffe.rssi.ru/SVA/NSM/Semicond/InP/index.html, "Ioffe Institute of Physics and Technology."

[56] L. P. Gonzalez, J. M. Murray, S. Krishnamurthy, and S. Guha, "Wavelength dependence of two photon and free carrier absorptions in InP," *Optics Express*, vol. 17, pp. 8741–8, May 2009.

[57] T. Matsusue, H. Bando, S. Fujita, and Y. Takayama, "Polarization dependence of two-photon absorption coefficient and nonlinear susceptibility tensor in InP," *Physica Status Solidi (C)*, vol. 8, pp. 387–389, Feb. 2011.

[58] D. H. P. Maat, *InP-based Integrated MZI Switches for Optical Communication*. Ph.d. thesis, Delft University of Technology, 2001.

[59] M. F. Yanik, S. Fan, M. Soljacić, and J. D. Joannopoulos, "All-optical transistor action with bistable switching in a photonic crystal cross-waveguide geometry," *Optics Letters*, vol. 28, pp. 2506–8, Dec. 2003.

[60] S.-H. Kwon, M. Kamp, A. Forchel, M.-K. Seo, and Y.-H. Lee, "Elimination of cross-talk in waveguide intersections of triangular lattice photonic crystals.," *Optics Express*, vol. 16, pp. 11399–404, July 2008.

[61] S.-h. Kim and Y.-h. Lee, "Symmetry relations of two-dimensional photonic crystal cavity modes," *IEEE Journal of Quantum Electronics*, vol. 39, pp. 1081–1085, Sept. 2003.

[62] P. Colman, S. Combrié, G. Lehoucq, and A. De Rossi, "Control of dispersion in photonic crystal waveguides using group symmetry theory.," *Optics Express*, vol. 20, pp. 13108–14, June 2012.

[63] Y. Yu, M. Heuck, S. Ek, N. Kuznetsova, K. Yvind, and J. Mørk, "Experimental demonstration of a four-port photonic crystal cross-waveguide structure," *Applied Physics Letters*, vol. 101, no. 25, p. 251113, 2012.

[64] L. Frandsen, A. Harpøth, P. Borel, M. Kristensen, J. Jensen, and O. Sigmund, "Broadband photonic crystal waveguide 60 degrees bend obtained utilizing topology optimization," *Optics Express*, vol. 12, pp. 5916–21, Nov. 2004.

[65] M. Heuck, P. T. Kristensen, and J. Mørk, "Energy-bandwidth trade-off in all-optical photonic crystal microcavity switches.," *Optics Express*, vol. 19, pp. 18410–18422, Sept. 2011.

[66] J. Xu, X. Zhang, and J. Mørk, "Investigation of Patterning Effects in Ultrafast SOA-Based Optical Switches," *IEEE Journal of Quantum Electronics*, vol. 46, no. 1, pp. 87–94, 2010.

[67] J. B. Khurgin, "Performance of nonlinear photonic crystal devices at high bit rates," *Optics Letters*, vol. 30, pp. 643–5, Mar. 2005.

[68] J. Mørk, F. Öhman, and S. Bischoff, "Analytical Expression for the Bit Error Rate of Cascaded All-Optical Regenerators," *Photonics Technology Letters*, vol. 15, no. 10, pp. 1479–1481, 2003.

[69] U. Fano, "Effects of Configuration Interaction on Intensities and Phase Shifts," *Physical Review*, vol. 124, pp. 1866–1878, Dec. 1961.

[70] M. Heuck, P. Trøst Kristensen, Y. Elesin, and J. Mørk, "Improved Switching using Fano Resonances in Photonic Crystal Structures," *Submitted*.

[71] S. F. Mingaleev, A. E. Miroshnichenko, and Y. S. Kivshar, "Coupled-resonator-induced reflection in photonic-crystal waveguide structures," *Optics Express*, vol. 16, no. 15, pp. 11647–11659, 2008.

[72] A. Cowan and J. Young, "Optical bistability involving photonic crystal microcavities and Fano line shapes," *Physical Review E*, vol. 68, p. 046606, Oct. 2003.

[73] K. Nozaki, T. Tanabe, A. Shinya, S. Matsuo, T. Sato, H. Taniyama, and M. Notomi, "All-optical Switch Involving Fano Resonance in Ultrasmall Photonic Crystal Nanocavities," in *Lasers and ElectroOptics CLEO and Quantum Electronics and Laser Science Conference QELS*, vol. 1, pp. 10–11, 2010.

[74] X. Yang, C. Husko, C. W. Wong, M. Yu, and D.-L. Kwong, "Observation of femtojoule optical bistability involving Fano resonances in high-Q/V silicon photonic crystal nanocavities," *Applied Physics Letters*, vol. 91, no. 5, p. 051113, 2007.

[75] A. Miroshnichenko and Y. Kivshar, "Engineering Fano resonances in discrete arrays," *Physical Review E*, vol. 72, p. 056611, Nov. 2005.

[76] S. M. Lea, *Mathematics for Physicists*. Thomson, Brooks/Cole, first ed., 2004.

[77] D. G. Hull, *Optimal Control Theory for Applications*. Springer-Verlag New York, Inc., 2003.

[78] P. Trøst Kristensen, M. Heuck, and J. Mørk, "Optimal switching using coherent control," *Applied Physics Letters*, vol. 102, no. 4, p. 041107, 2013.

[79] S. W. Warren, H. Rabitz, and M. Dahleh, "Coherent Control of Quantum Dynamics: The Dream is Alive," *Science*, vol. 259, pp. 1581–1589, 1993.

[80] N. Dudovich, D. Oron, and Y. Silberberg, "Coherent Transient Enhancement of Optically Induced Resonant Transitions," *Physical Review Letters*, vol. 88, p. 123004, Mar. 2002.

[81] H. Rabitz, "Focus on Quantum Control," *New Journal of Physics*, vol. 11, p. 105030, Oct. 2009.

[82] S. Sandhu, M. L. Povinelli, and S. Fan, "Enhancing optical switching with coherent control," *Applied Physics Letters*, vol. 96, no. 23, p. 231108, 2010.

[83] M. Ferrera, Y. Park, L. Razzari, B. E. Little, S. T. Chu, R. Morandotti, D. J. Moss, and J. Azaña, "On-chip CMOS-compatible all-optical integrator.," *Nature Communications*, vol. 1, p. 29, Jan. 2010.

[84] M. L. Nielsen and J. Mørk, "Increasing the modulation bandwidth of semiconductor-optical-amplifier-based switches by using optical filtering," *Journal of the Optical Society of America B*, vol. 21, no. 9, pp. 1606–1619, 2004.

[85] S. Combrié, M. Heuck, S. Xavier, G. Lehoucq, S. Malaguti, G. Bellanca, S. Trillo, P. T. Kristensen, J. Mørk, and A. D. Rossi, "Demonstration of Optically Controlled re-Routing in a Photonic Crystal Three-Port Switch," in *Integrated Photonics Research, Silicon and Nanophotonics*, pp. 5–7, 2012.

[86] J. Park, N. J. Kim, Y. D. Jang, E. G. Lee, J. M. Lee, J. S. Baek, J. H. Kim, H. S. Lee, K. J. Yee, D. Lee, S. H. Pyun, W. G. Jeong, and J. Kim, "Gain dynamics of an InAs/InGaAsP quantum dot semiconductor optical amplifier operating at 1.5 micrometer," *Applied Physics Letters*, vol. 98, no. 1, p. 011107, 2011.

[87] S. Matsuo, K. Takeda, T. Sato, M. Notomi, A. Shinya, K. Nozaki, H. Taniyama, K. Hasebe, and T. Kakitsuka, "Room-temperature continuous-wave operation of lateral current injection wavelength-scale embedded active-region photonic-crystal laser.," *Optics Express*, vol. 20, pp. 3773–80, Mar. 2012.

[88] P. N. Butcher and D. Cotter, *The Elements of Nonlinear Optics*. Cambridge University Press, first ed., 1990.

[89] Y. Elesin, B. S. Lazarov, J. S. Jensen, and O. Sigmund, "Time domain topology optimization of 3D nanophotonic devices," *Submitted*.

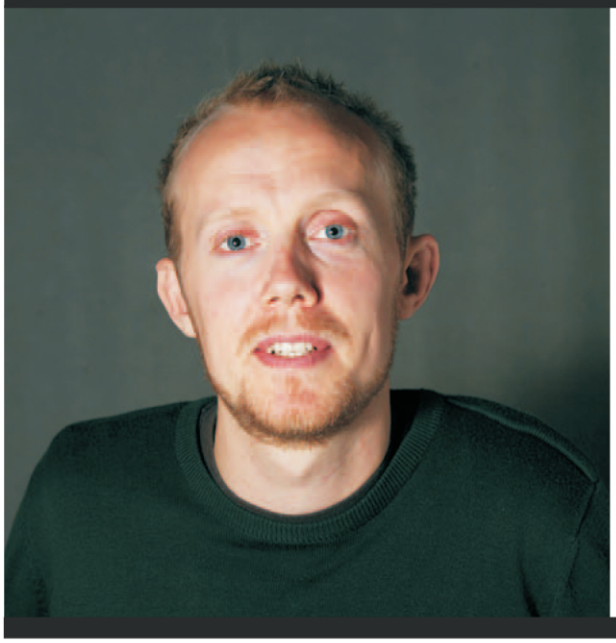

ISBN: 978-87-93089-10-5

Published by:
DTU Fotonik
Department of Photonics Engineering
Technical University of Denmark
Ørsteds Plads, building 343
DK-2800 Kgs. Lyngby

Mikkel Heuck was born May 27th, 1982, in Haderslev, Denmark. He received his M.Sc. degree in applied physics engineering from DTU Fotonik at the Technical University of Denmark in 2009. His thesis was concerned with theoretical aspects of photonic crystal mode locked lasers.
In his Ph.D. studies, Mikkel has moved the focus of his work to all-optical signal processing, while maintaining semiconductor photonic crystals as the material system of choice. During his Ph.D. Mikkel spent two months with Dr. Alfredo de Rossi at Thales Research and Technology in Palaiseau, France, as well as three months in the group of Yurii Vlasov at IBM T. J. Watson Research Center in Yorktown Heights, USA. This thesis was successfully defended on June 17, 2013.